Fatigue Life Prediction via Strain Energy Density and Digital Image Correlation

by

Ying Kei Samuel Cheung

A thesis submitted in conformity with the requirements
for the degree of Master of Applied Science
Graduate Department of Aerospace Science and Engineering
University of Toronto

Abstract

Fatigue Life Prediction via Strain Energy Density and Digital Image Correlation

Ying Kei Samuel Cheung
Master of Applied Science
Graduate Department of Aerospace Science and Engineering
University of Toronto
2020

The energy-based fatigue life prediction method estimates the fatigue life of a specimen, based on the theory that the total strain energy density dissipation required to cause monotonic quasi-static rupture is equivalent to the total energy dissipated in fatigue. The existing method is expanded to include predict the fatigue life of specimens with nanocrystalline coatings stressed at varying stress ratios. Digital image correlation is also used to demonstrate there is a region surrounding the fatigue crack initiation point where the strain energy density dissipation value deviates by a critical value from the median strain energy density dissipation value immediately prior to fatigue. This study represents one of the first instances in literature that the fatigue life of nanocrystalline-coated specimens has been quantified. As well, it provides a basis for estimating the fatigue life of coated specimens and an alternative indicator for predicting impending fatigue failure based on non-contact methods.

Acknowledgements

This thesis could not have been possible without the help of many others. It is not possible to fully acknowledge and show my utmost gratitude to each of them here, but I will humbly attempt to do so.

I'm extremely grateful to Dr. Craig Steeves for giving me the opportunity to undertake this project. The time I've spent at UTIAS undertaking this thesis has been one of the most challenging and rewarding times of my life. I'm thankful for his constant support throughout this project and for patiently answering the myriad questions I had. As well, thanks to Enzo Macchia at Pratt & Whitney Canada for bringing this project to life, Jeff Cook and Peter Miras for always lending us a hand in the lab, and Sal Boccia for his technical expertise in getting all our SEM images.

It was a privilege to have been a part of the Advanced Aerospace Structures group. Special thanks to Bharat Bhaga for helping me navigate Gentoo, Dan Pepler for making math more sensible, Isobel Lees and Cole Mero for the extra hands over the summers, and Katie Daley for your lab partnership throughout the long days (and nights!) during this project. To the rest of UTIAS, thank you for making the last few years incredibly enjoyable and I'm thankful to have met all of you.

I couldn't have made it this far without a strong community to keep me grounded. To the BSF fam, and especially Kris, Jon, Will, Charis and Angela, I was so blessed by your encouragement to always put my identity in Christ before all else. To Allie, Todd, Reb, Laura and James, thank you for the late night deep talks and laughs that pushed me through. To the numerous others that I had the opportunity to walk with these last few years, I have been so blessed by your presence in my life. And Viv, thank you for always praying for me and the reminders to always persevere. I am so glad we are able to walk together in life.

媽媽和爸爸 , thank you for always supporting me in all my endeavors. The man I am now is a testament to your constant prayers and love throughout my life. Words can't express how grateful I am to have you both as my parents.

Finally, all glory goes to God the Father, Son and Spirit. This thesis is a testimony to His glories and works. Truly, salvation belongs to our God alone and it is by faith in the resurrected Christ that we find salvation and the strength to live out the rest of our days.

Contents

1 Introduction **1**

1.1 Overview and Motivation 1

1.2 Incorporating Energy Methods to Predict Coated Specimen Fatigue and Obtain Fatigue Indicator Parameters 3

2 Theory and Background **5**

2.1 Overview of Metal Fatigue 5

2.2 Energy-Based Fatigue Model 8

2.2.1 Air Force Research Laboratory Energy-Based Fatigue Life Prediction Framework 8

2.3 Effects of Changes in Grain Size on Fatigue Life 15

2.4 Digital Image Correlation 18

2.4.1 Applications of DIC for Fatigue 19

3 Experimental Procedures **25**

3.1 Static and Fatigue Testing 25

3.2 Digital Image Correlation Measurements 28

4 Energy-Based Prediction for Coated Specimens **30**

4.1 Coated Specimen Fatigue Prediction Theory 30

4.1.1 Predicting Fatigue Life at Varying Stress Ratios 30

4.1.2 Fatigue Prediction for Coated Specimens 36

4.2 Material Properties 42

4.2.1 Al 6061-T6 properties 42

4.2.2 nNiCo properties 44

4.3 Fatigue Results 47

4.3.1 Fatigue Life of Uncoated Al 6061-T6 Specimens 47

4.3.2 Fatigue Life of nNiCo-coated Al 6061-T6 Specimens 49

4.4 Comparison of Fatigue Life Predictions Against Test Data 50
4.4.1 Fatigue Life Predictions for Al 6061-T6 51
4.4.2 Fatigue Life Predictions for nNiCo-coated Al 6061-T6 59
4.4.3 Analysis of Energy-Based Fatigue Life Prediction Framework 64

5 Evaluating Energy Dissipation Via Digital Image Correlation 67
5.1 Comparison Between Strain Gauge and DIC Strain Measurements 67
5.2 Measuring Strain Energy Density Dissipation Via DIC 71
5.2.1 Methodology 72
5.2.2 Results 73

6 Conclusions 80
6.1 Extension of the Energy-Based Fatigue Prediction Method 80
6.2 Strain Energy Dissipation Via Digital Image Correlation 81
6.3 Future Work 82

References 84

Chapter 1

Introduction

1.1 Overview and Motivation

The prediction of the number of cycles to failure in aerospace components is a critical safety step in the prevention of catastrophic fatigue failures. The two most common methods to predict fatigue failure are the safe-life and fail-safe approaches [1]. The safe-life approach considers the typical loading conditions and defines a conservative number of cycles after which the part should be removed from service. Since this approach is theoretical in nature, it may not always account for in-service conditions such as unexpected changes in loading conditions, batch variations, corrosion and test data scatter. Another approach is to use the fail-safe method, where parts are designed to withstand cracks of a certain size, and the prediction of the cycles to failure is based on a detectable crack size. Since the method is crack size dependent, periodic inspections must be conducted to ensure the crack size remains sufficiently small to not cause failure. These inspections result in part unavailability and high operator proficiency is required to detect the cracks.

The limits of these approaches were seen in 2018, when a fatigue failure on an engine blade caused a Southwest Airlines accident. Fragments from the broken engine blade damaged the engine inlet and cowling and broke a cabin window. A woman was sucked out of the broken window and sustained fatal injuries as a result. The subsequent National Transportation Safety Board (NTSB) investigation found features consistent with low-cycle metal fatigue, shown in Figure 1.1, which were not detected during the last inspection. The inspection was conducted using visual and fluorescent penetrant methods, which detect surface cracks. In this instance, the crack occurred on the interior section of the blade, making detection difficult. Two of the NTSB recommendations to prevent future failures were to decrease the inspection interval and to use ultrasonic techniques to examine for fatigue cracks [2]. Ultrasonic inspection techniques, along with eddy current inspection techniques, are

advantageous due to their ability to detect subsurface cracks. However, the techniques are only able to detect fatigue cracks after initiation and interpretation of the data is subject to operator judgment. The inspection interval required for crack propagation methods is problematic for nanocrystalline (NC) metals, since their fatigue crack growth rates are higher than conventional metals due to their smaller grain size [3] and hence the intervals must be shorter. Thus, it is desirable to find other fatigue indicators to monitor the remaining cycles to failure.

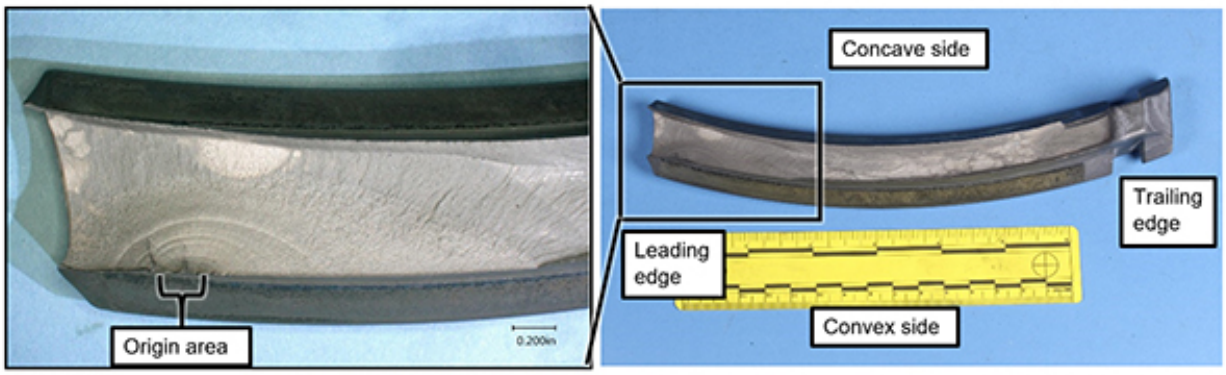

Figure 1.1 Fractured blade showing the initial crack initiation and propagation regions consistent with low cycle fatigue [2].

One method of monitoring the remaining cycles to failure is by monitoring the strain energy density dissipation (SEDD) of the specimen during fatigue. For every fatigue cycle, mechanical energy dissipation occurs when either 1) the specimen undergoes inelastic deformation, or 2) crack surfaces are formed in the specimen [1]. The sum of the energy dissipated during each fatigue cycle from these two modes is the total energy dissipation during fatigue. Literature suggests that the total energy dissipated during fatigue is equivalent to the energy required to cause monotonic quasi-static tensile rupture [4, 5, 6]. This energy level is known as the fatigue toughness value. Several studies have been conducted into using the cyclic energy dissipation value to determine critical points prior to fracture [7] and predicting the fatigue life for a given stress based on the measured energy dissipation [8, 9]. Monitoring energy dissipation rather than crack size may allow for simpler and more consistent fatigue monitoring, since inspections are no longer concerned with detecting very small cracks in the specimen, but rather are based on measuring the energy dissipation via the cyclic stress-strain behaviour.

Typically, strain gauges or extensometers are used to measure the strain in the specimen. The strain is used in the calculation of the cyclic SEDD, which is based on the load and strain in the specimen. Digital image correlation (DIC) is a new technique that is gaining

widespread acceptance as an alternative technique for measuring displacement and strain. DIC is a non-contact measurement method, where a random speckle pattern is applied to a specimen. The specimen is imaged in its undeformed and subsequent deformed states, and correlation algorithms are used to determine the changes in the speckle pattern and consequently the full-field displacements and strains [10]. In addition to full-field measurements, DIC has also been used to track fatigue microcracks [11], fatigue crack propagation [12] and as a measurement tool for plastic energy dissipation [13]. Figure 1.2 shows an example of DIC, where a speckle pattern is painted on a specimen that subsequently undergoes fatigue cycling. Figure 1.3 shows the strain field measurements obtained from the specimen in Figure 1.2 during fatigue cycling.

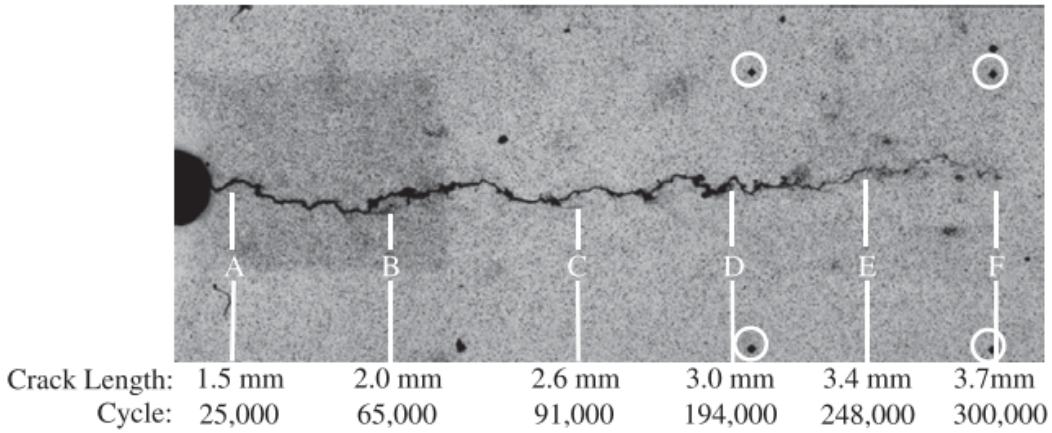

Figure 1.2 Specimen with speckle pattern painted, with indicators of the crack length during fatigue cycling [14].

1.2 Incorporating Energy Methods to Predict Coated Specimen Fatigue and Obtain Fatigue Indicator Parameters

The recent developments of nanocrystalline specimens and DIC present an opportunity to incorporate both of these into an energy-based fatigue prediction methodology. This thesis will quantify the effect of the nanocrystalline coatings on fatigue life and extend the energy-based prediction method to include methods to predict fatigue of coated metal specimens. As well, a new fatigue parameter that uses DIC to indicate impending fatigue fracture will be developed. This parameter incorporates the existing theories on energy dissipation during

fatigue. Chapter 2 describes the theoretical basis and current research for the SEDD theory, effect of nanometal coatings on fatigue, and the existing uses of DIC to measure fatigue parameters. Chapter 3 describes the experimental setup and procedure used to perform the tests. Chapter 4 describes the method used to expand the current energy dissipation theory to include coated metal specimen fatigue life predictions at different stress ratios. The predictions made by the model are compared to experimental test data to validate the theory. Chapter 5 describes the development of a new fatigue indicator parameter using the full-field calculated strain energy to predict impending fatigue failure. It also calculates the feasibility of using DIC as an alternate strain measurement system. Chapter 6 concludes the thesis by providing a summary of key findings and suggests future directions to extend the research.

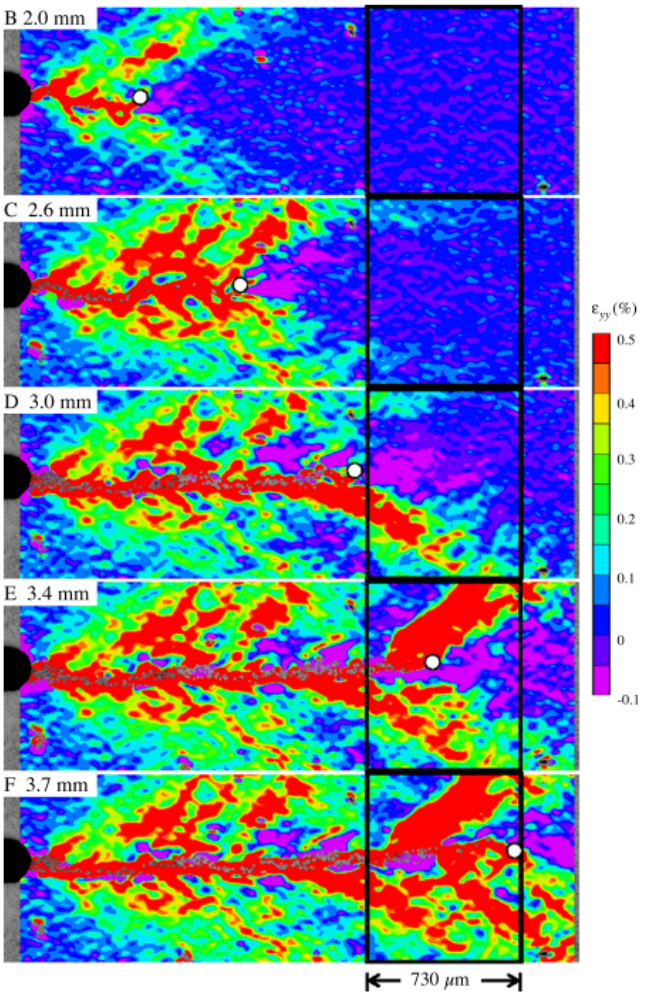

Figure 1.3 Example of the accumulated plastic strain fields at the points indicated from Figure 1.2 [14].

Chapter 2

Theory and Background

2.1 Overview of Metal Fatigue

Metal fatigue, defined by the International Organization for Standardization as "changes in properties which can occur in a metallic material due to the repeated application of stress or strains", has been studied since the early 1800s [1]. Fatigue studies are primarily concerned with overall life prediction, examining the factors that lead to crack initiation, the rate of crack growth, or the stress intensity of a crack.

The number of loading cycles a structure can sustain prior to failure is primarily a function of the applied load. Efforts to predict the relationship between the applied load and the life of a specimen can be traced back to Wöhler [15], who characterized fatigue behaviour in terms of stress-life, or S-N, curves. The stress-life model assumes a straight line log-log relation, represented by

$$\sigma_a = \sigma_f (2N_f)^b. \tag{2.1}$$

Here, σ_a is the applied stress amplitude, N_f is the number of cycles to failure, σ_f is the fatigue strength coefficient and b is the fatigue strength exponent. This is one of the most common methods used for the high cycle fatigue design of structures, and can be found throughout the literature. One of the major drawbacks of using this relationship is that many data points are required to generate statistically significant fits, creating an enormous strain on laboratory resources. As well, this relation does not take into account the effects of geometrical stress concentrations on the fatigue life and is only applicable for one loading configuration. Numerous corrections have been proposed to account for these issues, for example, including the Goodman relation to account for mean stresses, or using the elastic stress concentration factor to correct for notches in the specimen [15].

For low-cycle fatigue, plastic deformation occurs for each cycle. It is more appropri-

ate in these cases to consider the strain-life approach instead of the stress-life approach, since the strain-life approach incorporates the effects of metal plasticity during fatigue [15]. The Coffin-Manson relationship shows the relationship between plastic strain amplitude and cycles to failure,

$$\frac{\Delta\epsilon_p}{2} = \epsilon'_f \left(2N_f\right)^c , \tag{2.2}$$

where ϵ_p is the plastic strain amplitude, ϵ'_f is the fatigue ductility coefficient and c is the fatigue ductility exponent [1]. The plastic strain amplitude is typically more difficult to measure than the total strain amplitude. If the Young's modulus, E, is known, the elastic strain components can be estimated. Equation 2.2 can then be rewritten to require the total strain amplitude $\Delta\epsilon$, rather than the plastic strain amplitude, as

$$\frac{\Delta\epsilon}{2} = \frac{\sigma'_f}{E} \left(2N_f\right)^b + \epsilon'_f \left(2N_f\right)^c . \tag{2.3}$$

Although the stress-life and strain-life methods measure the total life until unstable crack propagation, sometimes it is desirable to predict cycles to crack initiation or the cycles required to extend a given crack. In this thesis, crack initiation is defined as the nucleation of a fatigue crack that can be detectable by typical non-destructive methods. Most crack initiation models are based at least in part on the specimen microstructure. These are often challenging to model, since they are heavily dependent on factors such as the geometry of the grain boundaries, dislocation substructures and the development of lattice curvature [16]. One method to reduce the sensitivity of the model to the details of the microstructure is to focus analysis at the meso-scale rather than the micro-scale. The most prominent models use the concept of slip plastic flow, where cracks are assumed to initiate from inclusions or slip bands, which occur when dislocations accumulate [1]. Other models calculate the likelihood of crack initiation based on the probability of inclusions [17]. The crack initiation models listed above do not examine specimens as a whole, since intergranular stresses, strain field interactions and realistic dislocation structures are not considered [16]. One solution was proposed by Kohn [18], who studied an *in-situ* acoustic emission method to monitor crack initiation throughout a specimen. In the study, three distinct fatigue stages generated acoustic emissions: crack initiation, slow crack propagation and rapid crack propagation. By monitoring changes in the acoustic events, these events could be correlated to changes in crack initiation by detecting incipient fatigue crack extensions as low as 10 µm. This *in-situ* approach offers the opportunity to examine crack initiation from an overall view, rather than only at the grain level.

Crack propagation life methods are frequently used within the aerospace industry to determine whether parts should be taken out of service after non-destructive inspection.

Parts are designed so that they will not fail until after cracks are detectable by the chosen inspection method. The parts are inspected from time to time, where it is assumed that the fatigue between inspection intervals will not propagate cracks to the point of unstable crack propagation. One common method to calculate the propagation rate is the Paris law [19],

$$\frac{\mathrm{d}a}{\mathrm{d}N} = C_0 \Delta K^m, \tag{2.4}$$

where $\frac{\mathrm{d}a}{\mathrm{d}N}$ is the change in the crack length per load cycle the fatigue life, C_0 and m are fit constants and ΔK is the stress intensity factor (SIF) range. The SIF range describes the changes in the stress-field around the crack tip based on the geometry and loading conditions at the minimum and maximum loads. The Paris law is useful to estimate the number of loading cycles to failure once a crack is detected and its length measured.

Another method to estimate the number of cycles to failure uses the strain energy density dissipation (SEDD). During fatigue, small amounts of energy are dissipated during plastic deformation and when cracks are formed and extended [1]. The energy dissipated during a fatigue cycle is equal to the area within the stress-strain hysteresis loop. An example of an exaggerated hysteresis loop where the coordinate axes are shifted to the origin is shown in Figure 2.1. Enomoto [4] showed there is a critical SEDD value corresponding to fatigue which can be used to estimate the cycles to failure in a specimen. Strain energy-based methods have several advantages, primarily that they do not require monitoring of crack formation and can provide *in-situ* data. Fatigue models based on strain energy are discussed in the next section.

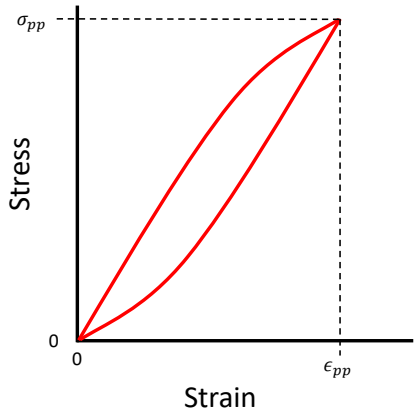

Figure 2.1 Exaggerated hysteresis loop with coordinate axes shifted to the origin, based on the figure by Scott-Emuakpor [20].

2.2 Energy-Based Fatigue Model

Extensive research has been done into the energy relationship between monotonic fracture and fatigue fracture. The earliest research into this relationship was done by Enomoto [4], who proposed that the total energy loss per unit volume which can be attributed to fatigue failure is constant. The theory was advanced by Stowell [6], who found that in the cases of fatigue failures with strain cycling about zero mean strain, failure occurs when the total amount of strain energy dissipated in the fatigue test is equal to the energy required for monotonic fracture.

There is debate in the literature over whether the estimation should be restricted to the mechanical energy dissipation, as there may be thermodynamic contributions [21] or acoustic contributions [17] to the energy dissipation. One school of thought is that at lower cyclic frequencies, these contributions are minimal. Since the analyses limited to mechanical dissipation show fairly robust results [8], the discussion will assume the primary cause of energy dissipation leading to fatigue fracture is mechanical.

2.2.1 Air Force Research Laboratory Energy-Based Fatigue Life Prediction Framework

Research into the relationship between energy dissipation and fatigue life continued at the Air Force Research Laboratory (AFRL) at the Wright-Patterson Air Force Base. The trends of strain energy density per cycle were analyzed in order to develop a fatigue life prediction method [22]. Using the fundamental assumptions that 1) the SEDD per cycle at a given stress amplitude is constant and 2) the total SEDD to cause fatigue fracture is constant and equal to the energy dissipated in monotonic fracture [23], they proposed that the total life could be found by dividing the total SEDD in monotonic fracture by the measured SEDD for a representative fatigue cycle [22]. These experiments were originally done for fully reversed cycling (stress ratio R = -1.0) at different stress amplitudes.

To find the monotonic strain energy density, the Ramberg-Osgood constitutive equation was used to describe the monotonic stress-strain curve up to the point of necking. The equation was expressed as

$$\epsilon = \frac{\sigma}{E} + \epsilon_0 \sinh\left(\frac{\sigma}{\sigma_o}\right), \tag{2.5}$$

where the σ represents the specimen stress, ϵ is strain, E is the elastic modulus and ϵ_0 and σ_0 are material constants. A linear relationship was used to represent the curve beyond the necking point,

$$\sigma = \beta_1 \epsilon + \beta_0, \tag{2.6}$$

where β_0 and β_1 are material constants, found by curve-fitting a line between the necking point and the fracture point.

The cyclic SEDD is found by calculating the area of the hysteresis loop represented by the loading and unloading stress-strain curve for a given fatigue cycle. To simplify the analysis, the compressive stress-strain behaviour is assumed to be the same as the tensile stress-strain behaviour, ignoring the Bauschinger effect [7]. The data are then shifted to a generalized coordinate system, where the minimum fully reversed point of the hysteresis loop is set at the origin, as shown in Figure 2.1.

The cyclic Ramberg-Osgood relation is used to represent the stress-strain behaviour in fatigue. Similar terms to the monotonic relation from Equation 2.5 are used, however the stress parameter is σ_{pp}, representing the peak-to-peak stress or twice the stress amplitude, and the parameter σ_0 is changed to σ_c, which is a curve fit parameter similar to σ_0 but renamed to avoid confusion with the monotonic parameter, and the curve fit parameter ϵ_0 is changed to $\frac{1}{C}$. The new equation becomes

$$\epsilon = \frac{\sigma_{pp}}{E} + \frac{1}{C}\sinh\left(\frac{\sigma_{pp}}{\sigma_c}\right). \tag{2.7}$$

Since the total energy dissipation from monotonic fracture is equal to the average cyclic energy dissipation times the number of cycles, the relation is expressed as,

$$W_f = NW_c, \tag{2.8}$$

where the monotonic fracture energy is W_f, the average cyclic energy dissipation is W_c, and the number of cycles to fracture is N. To find the average cyclic energy dissipation, the cyclic Ramberg-Osgood relation is integrated between the loading and unloading stress-strain curves,

$$W_c = \sigma_{pp}\epsilon_{pp} - 2\int_0^{\sigma_{pp}} \epsilon_{pp}\mathrm{d}\sigma_{pp}. \tag{2.9}$$

The fatigue life is then predicted by inserting Equation 2.9 into Equation 2.8 and rearranging the terms,

$$N = C\frac{\sigma_n\left(\epsilon_n - \frac{\sigma_n}{2E}\right) + \epsilon_o\sigma_o\left(\cosh\left(\frac{\sigma_n}{\sigma_o}\right) - 1\right) + \frac{\beta_1}{2}\left(\epsilon_f^2 - \epsilon_n^2\right) + \beta_0\left(\epsilon_f - \epsilon_n\right)}{2\sigma_c\left(\frac{\sigma}{\sigma_c}\sinh\left(\frac{2\sigma}{\sigma_c}\right) - \left(\cosh\left(\frac{2\sigma}{\sigma_c} - 1\right)\right)\right)}, \tag{2.10}$$

where the expression for W_f is the integration of Equations 2.5 and 2.6 and the expression for W_c is from Equation 2.9. Figure 2.2 compares the experimental fatigue life results against the fatigue life that was predicted using Equation 2.10. In the figure, the fatigue life was

shown to be underpredicted at high stress levels and overpredicted at low stress levels.

In order to improve the fatigue life prediction, several model parameter corrections were considered by different authors. These corrections included modifying the region from which the average strain energy was obtained [20], using different frequencies [24], and using the strain range rather than the hysteresis loops [23]. The above equations are also limited to fully reversed cycling. Further methods were developed by Scott-Emuakpor et al. [22] to correct for non-zero mean stresses during cycling.

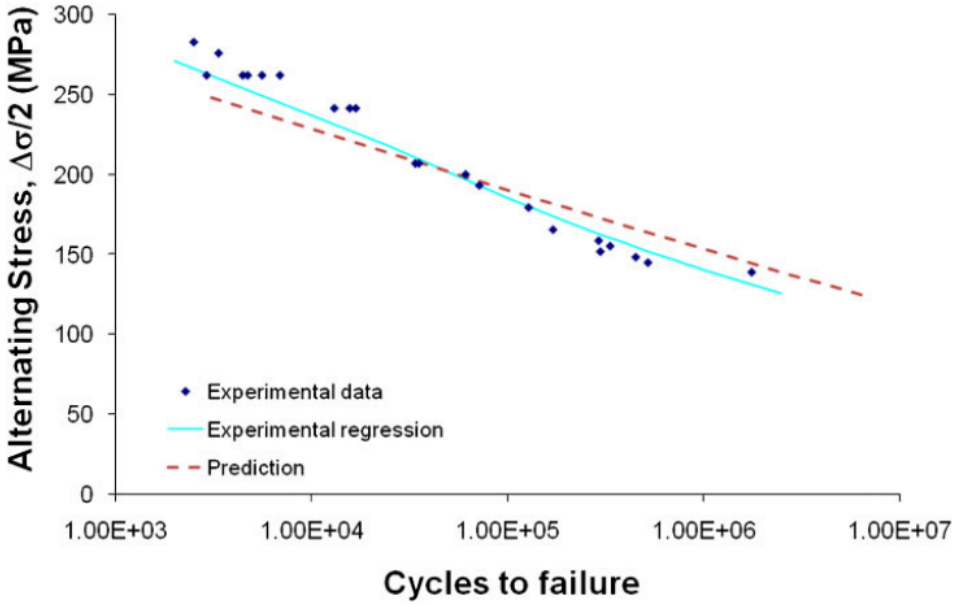

Figure 2.2 Experimental results versus the corresponding fatigue life predictions for fully reversed testing. The fatigue life was underpredicted at high stress amplitudes and overpredicted at low stress amplitudes [20].

Distribution of the Strain Energy Density Dissipation

The original Scott-Emuakpor model [22], described by Equation 2.10, used an average SEDD to predict the fatigue life. However, the plastic SEDD for each cycle does not remain constant throughout fatigue. For materials that exhibit cyclic hardening, there are three distinct phases of the SEDD for each cycle [20]. These three regions are shown in Figure 2.3, where section A shows the cyclic strain energy dissipation decreasing early in the process, section B shows the cyclic strain energy dissipation stabilizing at constant value, and section C shows the strain energy dissipation increasing rapidly as the loading cycles approach failure. A cyclic softening material would show the SEDD increasing initially rather than decreasing [5]. The changes in strain energy dissipation can be explained from a microstructural point

of view. The initial increase or decrease in SEDD can be attributed to the changes of the dislocation structures within the specimen during initial loading, after which the material experiences "stress saturation". At this point, the specimen has reached an equilibrium dislocation structure which can accommodate the imposed stresses with minimal increases in strain [5]. When large fatigue cracks begin to form on the surface, the energy required to form them increases significantly, thus resulting in the large increase in SEDD. Since the crack initiation stage, rather than the crack growth stage, takes up the majority of the fatigue life, the large increase in energy is only seen near fatigue failure.

One observation made about the variation in strain energy was that there was a critical variance in the SEDD prior to failure. Letcher [7] suggests that the cycle corresponding to a 5% deviation from the steady-state strain energy density values can be defined as the critical lifetime, as the accumulated SEDD up to this value were the same for different stress levels. This value was selected to avoid electrical noise in the strain signal and slight variations in load during fatigue testing. This approach offers an alternative way to monitor fatigue, since the specimen can be removed from service once deviations in the cyclic SEDD are observed. However, one disadvantage of this method is the requirement to record hysteresis data frequently during fatigue.

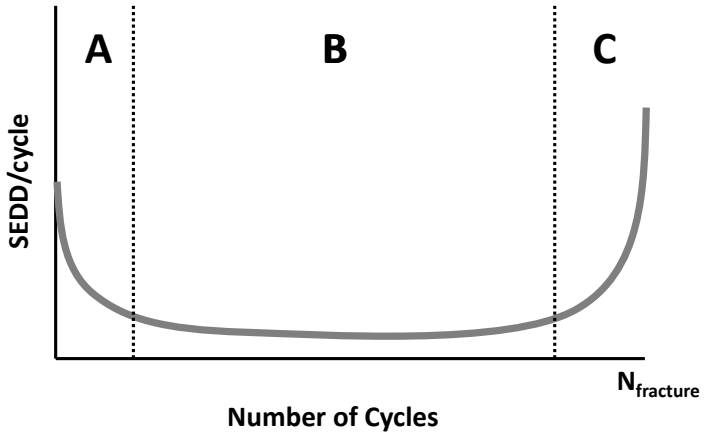

Figure 2.3 Representative strain energy variation over the lifetime of a specimen, modified from [20].

Using the Strain Range as an Alternate Measurement for Strain Energy Density Dissipation

Experimental data in Figure 2.4a shows that there is an additional energy contribution during the fatigue caused by anelastic effects such as friction and damping. These effects are dissipated as heat energy and do not contribute to mechanical damage of the specimen. However, the hysteresis loops generated by the specimen loading and unloading curves do not differentiate between the two energy types, making it difficult to obtain an estimate of the mechanical energy dissipation for the fatigue cycle. Ozaltun [25] performed a series of experiments to determine whether there was a critical frequency below which the hysteresis loops became free from anelastic effects. Figure 2.4b shows that below 0.05 Hz, the hysteresis loop sizes and the corresponding SEDD become frequency independent.

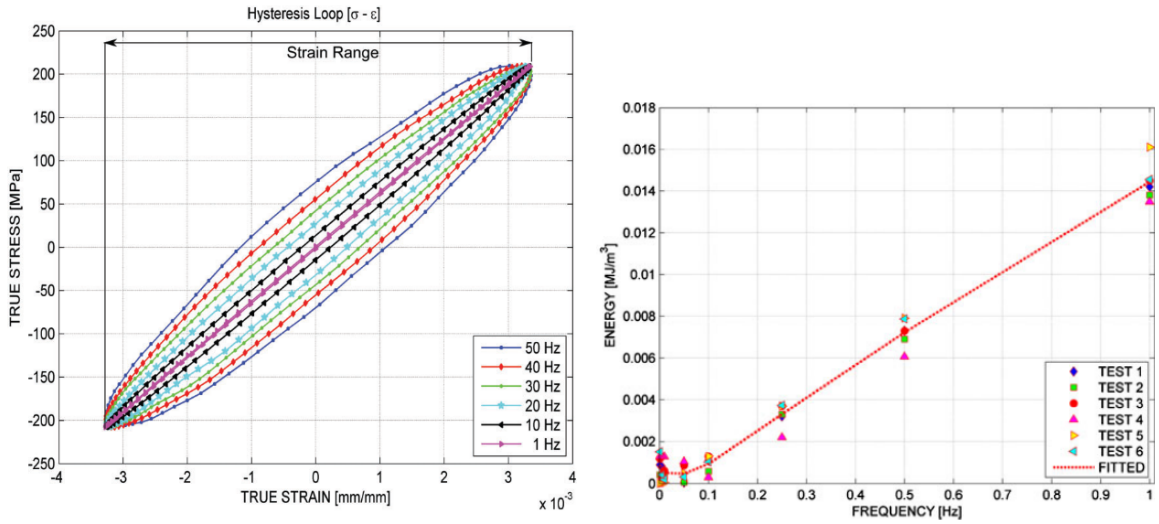

(a) **(b)**

Figure 2.4 Changes in the overall energy dissipation with frequency, shown by the hysteresis loop sizes changing in Figure 2.4a [25] and the changes in the measured energy dissipation in Figure 2.4b [24].

It is unclear whether this critical frequency is applicable across all material and load conditions or whether it is only applicable for the loading conditions in the aluminum used in this test. Since the model is very sensitive to deviations in the hysteresis loop measurement, an alternate model was developed by Shen and Akanda [23] to eliminate this measurement by using the strain range. Figure 2.4a shows that the strain range remains the same at different frequencies despite the hysteresis loop sizes changing. Thus, by developing the relation between the strain range to the SEDD, tests can be run much more quickly and the frequency no longer becomes a factor. The model is derived from the cyclic Ramberg

Osgood constitutive equation,

$$\epsilon = \frac{\sigma}{E} + \left(\frac{\sigma}{K'_H}\right)^{\frac{1}{n'}}, \tag{2.11}$$

where n' represents the cyclic strain hardening exponent and K'_H is a coefficient related to the cyclic strength coefficient K' of a cyclic stress-strain curve for a material which exhibits Masing-type behaviour, by the relation $K'_H = K'2^{n'} - 1$. Masing-type behaviour is exhibited when the stable hysteresis loops at different strain amplitudes have a common loading curve geometry if the compressive hysteresis loop tips are transferred to a common origin. This behaviour is typically associated with metals where the deformation behaviour is structurally controlled and independent of matrix properties [5].

The elastic component and plastic component of the average strain range can be separated into

$$\Delta\epsilon_e = \frac{\Delta\sigma}{E} \tag{2.12}$$

and

$$\bar{\Delta\epsilon_p} = \left(\frac{\Delta\sigma}{K'_H}\right)^{\frac{1}{n'}}. \tag{2.13}$$

The assumption that the total energy dissipation from monotonic fracture is the same as the average cyclic energy dissipation times the number of cycles, shown by Equation 2.9, still applies. After integrating, the average strain energy dissipation per cycle can be found as

$$\bar{w}_d = \frac{W_f}{N_f} = (\Delta\sigma)^{\left(1+\frac{1}{n'}\right)} \left(\frac{1}{K'_H}\right)^{\frac{1}{n'}} \left(\frac{1-n'}{1+n'}\right). \tag{2.14}$$

If the fatigue lives and stress ranges for two tests are known, the variable n' can be calculated by

$$n' = \frac{\ln\left(\frac{\Delta\sigma_1}{\Delta\sigma_2}\right)}{\ln\left(\frac{N_{f2}}{N_{f1}}\right) - \ln\left(\frac{\Delta\sigma_1}{\Delta\sigma_2}\right)}. \tag{2.15}$$

Rearranging the cyclic Ramberg Osgood Equation, the variable $\frac{1}{K'_H}$ can be found from

$$\frac{1}{K'_H} = \frac{1}{\Delta\sigma} \exp\left[n' \ln\left(\bar{\Delta\epsilon} - \frac{\Delta\sigma}{E}\right)\right]. \tag{2.16}$$

The predictions generated by the Shen and Akanda method are compared to those from the original Ozaltun method. Figure 2.5 shows the Shen and Akanda method is slightly more accurate for predicting cycles to failure. Not only is the prediction improved, but the fatigue life can be found much more quickly by using higher testing frequencies. As well, only two

points are needed to generate the curve, although increasing the number of points would improve the reliability of the prediction by reducing the effect of outliers in the data.

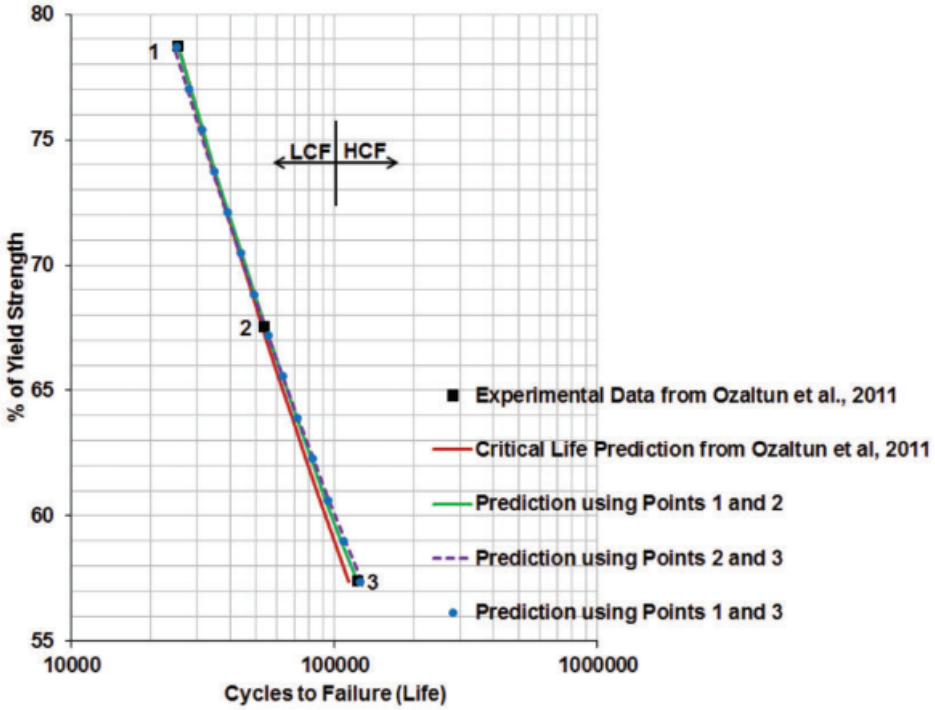

Figure 2.5 Comparison of the hysteresis loop prediction model (shown in red) and the strain range prediction model (shown in green and purple) [23].

Fatigue Tests at Varying Stress Ratios

The above discussions indicated the total SEDD in fatigue is equal to that of monotonic dissipation, where the SEDD per fatigue cycle is equal to the area bounded by the tensile and compressive stress-strain curves and the SEDD in monotonic dissipation is equivalent to the area below the monotonic stress-strain curve. These relations are valid for a fully-reversed fatigue test with a stress ratio of -1.0. However, for the non-zero mean stress cases, the amount of energy dissipation changes [26]. The application of a mean stress during fatigue implies strain energy is dissipated by a constant static applied load throughout cycling, thus causing a reduction in the strain energy. As well, the shape and size of the hysteresis loop changes when mean stress is applied. Rather than an enclosed loop, the hysteresis loop has an open end, as shown in Figure 2.6. In addition, the plastic deformation in the hysteresis loop caused by the mean stress is greater than deformation without mean stress. The equations used to define the changes in SEDD due to the mean stress are described in detail in [26].

It is sufficient to note here that if fatigue cycling with a non-zero mean stress occurs, the total SEDD required for fatigue failure will decrease and the cyclic SEDD will increase, thus requiring changes to the presented equations.

Strain Energy Density Measurement Methods

The hysteresis loops were measured in these experiments using both strain gauges and extensometers. These are generally used to measure experimental strains due to their ease of use. However, the need for the equipment to be attached to the specimen and the lack of ability to obtain full-field strains presents a significant drawback. As well, another drawback in using strain gauges and extensometers is data crossover. Although certain frequencies and data sampling rates can reduce the effect of crossover on the resulting data [27], an alternative method is to use digital image correlation (DIC) to capture these hysteresis loops. DIC was used by Celli [28], who found the total strain energy density dissipated measured by an extensometer and DIC varied by less than 1.2%. Details of DIC are discussed later in this chapter in Section 2.4.

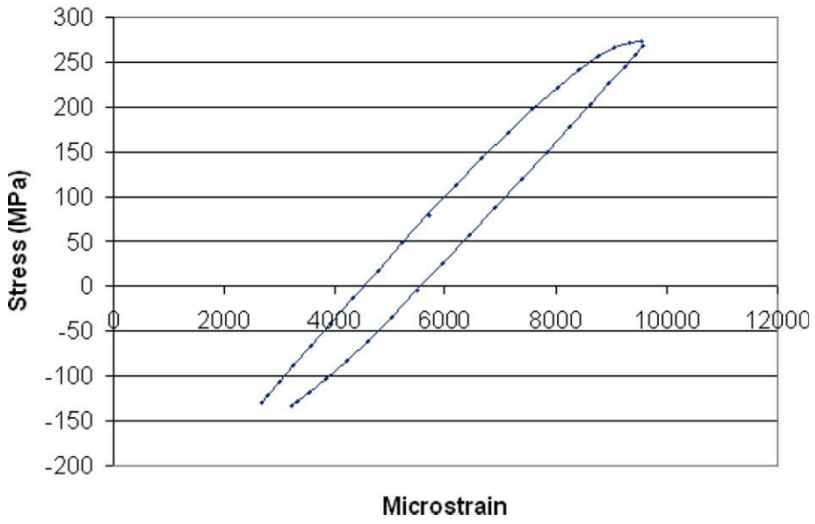

Figure 2.6 Example of a hysteresis loop when 70 MPa mean stress is applied showing the open-ended loop [26].

2.3 Effects of Changes in Grain Size on Fatigue Life

Most fatigue studies, like the AFRL studies mentioned above, have primarily focused on the effect of fatigue on conventional materials. Literature does not currently exist to relate the SEDD to nanocrystalline (NC) materials. NC metals, defined as metals with grain

sizes below 100 nm [29], compose a material category that is gaining popularity due to their unique mechanical behaviour, particularly their increased yield strength and possible increase in fatigue life [3]. A landmark paper by Gleiter [30] established some of the key mechanical properties of NC materials, but only in recent years has the fatigue behaviour begun to be extensively studied, due to the challenges in producing NC metals that comply with American Society for Testing and Materials (ASTM) standards for fatigue testing [31]. As well, the data between researchers sometimes conflicts even though the material may be obtained from the same supplier, due to variations in sample chemistry, microstructure and even test methods such as whether bulk materials or thin film samples are used for testing [29].

In general, fatigue lifetimes of NC metals have been shown to be greater than their conventional counterparts. The vast majority of a specimen's fatigue lifetime is dominated by crack initiation. If fatigue cracks take longer to initiate in a metal, then the fatigue life should correspondingly increase. Experimental results show NC metals resist crack initiation better than their conventional counterparts [31]. One possibility is that the benefit arises from the inhibition of crack nucleation due to the surface smoothness caused by the smaller grain size [31], although the NC specimens used in this thesis were observed to have a rougher surface. It should be noted that this increased resistance to crack initiation assumes internal processing defects do not exist, as the smaller critical crack length in NC materials results in increased sensitivity to internal defects and inclusions [29, 32].

Although the decrease in grain size results in improved resistance to crack nucleation, the opposite is true with resistance to crack propagation. Due to the grain refinement, there is reduced crack path tortuosity, as shown in the changes in crack path in Figure 2.7 [31]. As well, it is believed that the effective driving force for crack propagation of NC materials is less than those of its conventional counterparts [31], and there is a diminishing contribution of roughness-induced and plasticity-induced crack closure [29]. An exception to the increased crack propagation rates as grain size decreases is when twin grain boundaries are found in NC metals. Since twin boundaries are the principal sites for accumulation and pile-up of partial dislocations, the enhanced plastic strain accommodation at these areas reduces the crack growth propagation rate [33].

One factor that complicates the analysis of NC materials is the presence of residual stresses. Both residual compressive and tensile stresses have been reported for electrodeposited NC materials, while some forms of NC processing, such as equal channel angular processing, inevitably introduce residual stresses. For conventional metals, fatigue life generally improves if residual compressive stresses are present. However, the results found for NC metals show ambiguity regarding the effects of residual stresses. Although the above

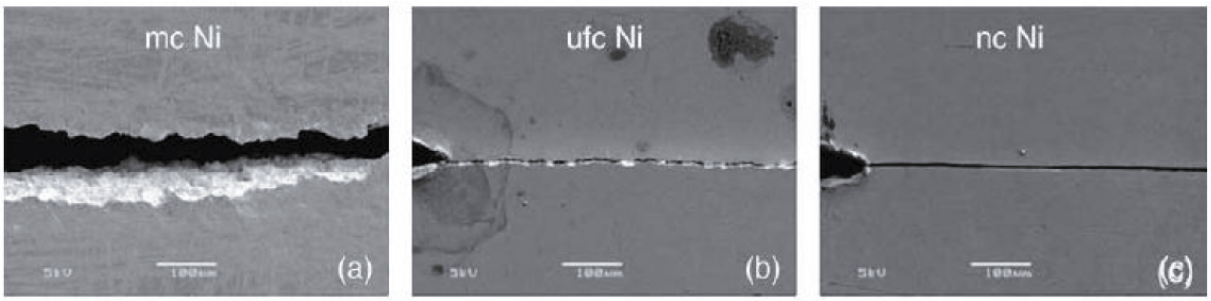

Figure 2.7 SEM of (a) conventional, (b) ultra-fine crystalline, and (c) nanocrystalline nickel subjected to fatigue loading of R=0.3, demonstrating crack path tortuosity decreasing with grain refinement [34].

mentioned crack initiation and crack growth mechanisms hold typically true, it is difficult to definitively conclude NC materials have improved fatigue life.

An area of study of NC materials that is of particular interest for this thesis is the fatigue performance of NC-coated materials. However, the only major piece of literature is by Sriraman et. al [35], where for fatigue tests of coated steel samples with Ni-W alloys of varying crystal sizes, the coated samples exhibited inferior fatigue lives compared to uncoated samples. It is important to note that within this coated sample group, the fatigue life increased as the coating grain size decreased. It appears that the presence of tensile residual stresses and inherent micro-cracks in the coating caused a fatigue crack to initiate at the surface of the deposit, which then extended to the substrate with the assistance of the metallic bonding established at the interface, thus reducing the crack nucleation stage at the steel interface. The other study available to the author was conducted in-house at the University of Toronto Institute for Aerospace Studies [36], where certain coating combinations were found to provide an improvement in fatigue life for coated Al 7255 specimens. The results showed NC nickel coatings caused a reduction in the fatigue life, whereas coatings using NC cobalt phosphorus improved the fatigue life if the quality of the coating was sufficient. As the specimens which had improved fatigue life did not fracture within the gauge section, but rather within the tensile grips of the test machine, it was difficult to estimate the exact improvement attributable to the coating.

The current literature examining NC fatigue shows that there are still significant questions outstanding before NC materials can be fully utilized in engineering applications, particularly with respect to the fatigue behaviour in NC-coated specimens. This thesis will attempt to further increase the understanding of fatigue in NC-coated aluminum specimens.

2.4 Digital Image Correlation

Section 2.2.1 briefly discussed the benefits and drawbacks of using strain gauges and extensometers. As mentioned above, the major drawbacks of these two methods is the need for equipment to be attached to the specimen and the lack of ability to obtain full-field strains. To obtain full-field non-contact strains, interferometric techniques and DIC techniques were developed [10]. DIC is a non-contact technique that uses imaging devices, often digital cameras, to measure the strains after deformation. Depending on the number of cameras used in the recording process, both two-dimensional and three-dimensional full-field surface displacements and strains can be obtained.

DIC is based on the recognition of geometric changes in the distribution of speckle patterns after sample deformation [37]. The general principle of DIC is to track the square region surrounding a point in a reference image and find the corresponding location in an image of a deformed image [38]. The process is then repeated for every point until the deformation of the entire specimen is known. A differentiation of the deformation fields is performed to find the corresponding strain fields. Smoothing functions are then applied to reduce the noise caused by the differentiation. An example of a deformed specimen with a speckle pattern, and the corresponding strain field overlaid, is shown in Figure 2.8.

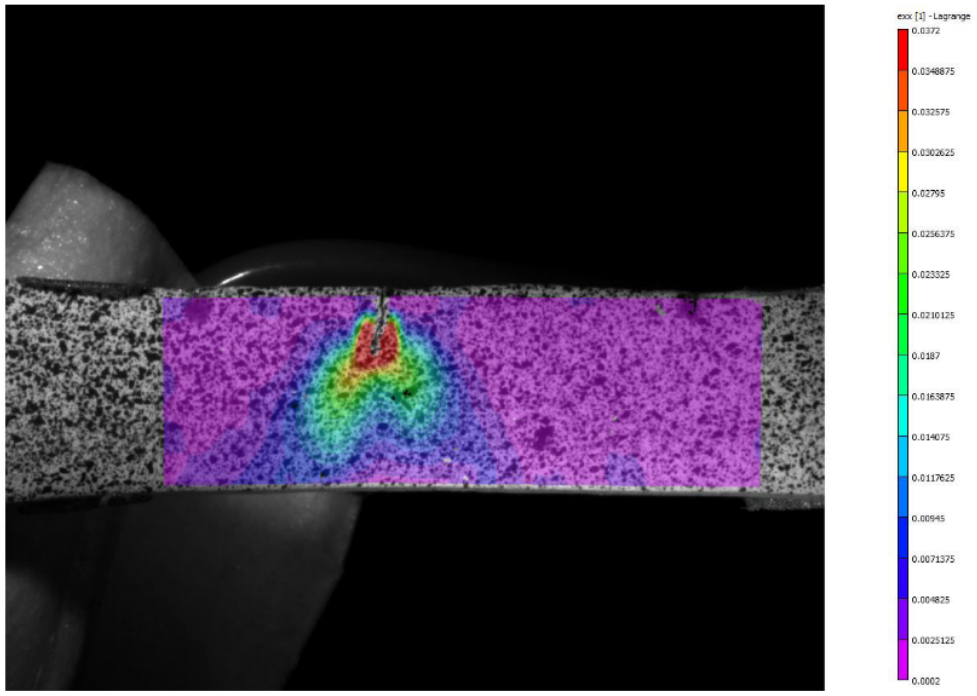

Figure 2.8 Example of a speckle pattern after deformation with the corresponding strain field overlaid.

Since its development at the University of South Carolina in the 1980s [10], the method has been improved to reduce the computational requirements, increase the accuracy of sub-pixel deformation measurements, and expand its uses from biology [37] to aerospace applications [39]. Detailed descriptions of the developments and the applications of DIC methods can be found in review papers by Pan [10] and Hild and Roux [40].

Several factors contribute to the quality of the results of DIC. First is the quality of the speckle pattern. Different parameters, including mean speckle size, subset entropy and sum of square of subset intensity gradients have been proposed to evaluate the quality of the speckle pattern [10]. However, a consensus has not yet emerged on the optimal speckle pattern as it is heavily dependent on other factors such as the subset size used in the analysis and the size of the tested specimen. Another factor is the quality of the image obtained, particularly image distortion and environmental noise [10]. Although this can be partially mitigated by using high resolution imaging equipment, the trade-off is the significantly increased cost. Further, the subset size used in analysis plays a large role in the resolution of the measurements. Resolution is increased when smaller subset sizes are used, but noise is also increased for these smaller sizes [10].

2.4.1 Applications of DIC for Fatigue

DIC has been extensively used in the last two decades to evaluate properties in fatigue, particularly to evaluate the fracture properties associated with crack growth. Figure 2.9 shows how fatigue cracks can be characterized by a leading cyclic plastic zone in the shape of two lobes, followed by the crack itself surrounded by a plastic wake [41]. Crack closure events may exist, depending on the stress levels and loading conditions. DIC has been used to characterize these plastic zones, the plastic wake and evaluate the SIFs at the tip [42, 43, 44].

Measurement of the SIF at the crack tip was one of the earliest uses of DIC [41]. At the crack tip, the stresses are significantly higher than the far-field stresses. The SIF is used to describe the increased stresses at the crack tips via linear and nonlinear fracture mechanics. Several mathematical descriptions are available to describe the crack tip stresses depending on the geometry and can be found in literature [1]. The classical two-dimensional axial stress, σ_y, at the crack tip when under tension is,

$$\sigma_y(x,0) = \frac{K_I}{\sqrt{2\pi x}}. \tag{2.17}$$

This expression is for the axial stresses on a line perpendicular to the loading direction which runs through the crack tip. K_I represents the Mode I SIF and x represents the distance on

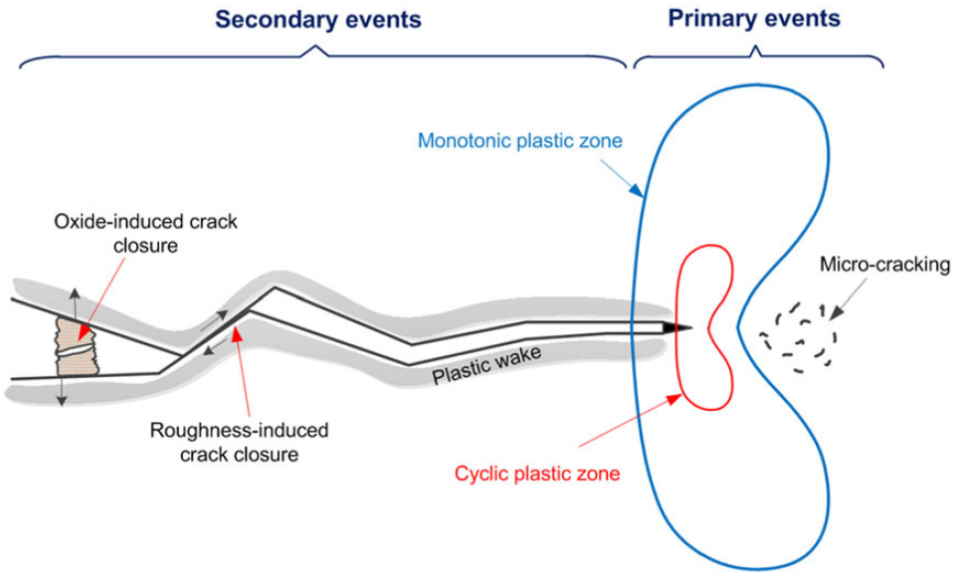

Figure 2.9 Schematic of the primary events ahead of the crack tip and secondary events behind the crack tip under cyclic loading [41].

the perpendicular line away from the crack tip, as shown in Figure 2.10a. The Mode I stress intensity description is used for a tensile fracture stress normal to the crack plane [1]. The value of K_I depends on the crack geometry and load type. This thesis focuses on fatigue loads, where cracks are usually observed to initiate from the edge of a specimen. The Mode I stress intensity for edge-cracked specimens with a crack length of $2a$ is

$$K_I = 1.122 \left(\sigma_y\right)_\infty \sqrt{\pi a}, \tag{2.18}$$

where $\left(\sigma_y\right)_\infty$ represents the far field tensile stress applied [5].

Crack length information is required to solve Equation 2.18 but may be difficult to obtain. The Williams series expansion relates the displacement fields to the stresses near a crack tip. Since the output of DIC is the full-field displacement fields, the SIF can be found without finding the crack length information. Alternatively, the J-integral approach can also be used for SIF estimation. The J-integral was originally proposed by Rice [45] to calculate the strain energy release rate. Figure 2.10a illustrates the original concept of the J-integral, where for a cracked body the line integral around the crack tip is given as

$$J = \int_\Gamma \left(w \mathrm{d}y - T_i \frac{\partial u_i}{\partial x} \mathrm{d}s \right). \tag{2.19}$$

The coordinate system is the same as used in Equation 2.17, where the x axis is parallel

to the crack and the y axis is perpendicular to the crack. The integral path is represented by γ, which is an arbitrary contour around the crack tip. The total strain energy density is w and the traction vector is T. The displacement vector is u_i and a small increment of the arc length is represented by ds [46, 47, 48]. The strain energy density is related to the stress tensor by $\sigma_{ij} = \frac{\partial w}{\partial \epsilon_{ij}}$. The J-integral is path-independent for linear or nonlinear elastic behaviour [1].

The conversion from a J-integral value to a Mode I SIF for a linear elastic fracture mechanics problem can be found by

$$K_I = \sqrt{JE'}, \tag{2.20}$$

where

$$E' = \begin{cases} E & \text{for plane stress, and} \\ \frac{E}{1-\nu^2} & \text{for plane strain.} \end{cases}$$

E is the elastic modulus of the specimen and ν is the Poisson ratio. One of the methods to calculate the J-integral is to evaluate the line integral in the equation using the displacement fields from DIC, however calculation of the line integral may be inaccurate and mathematically complex [47]. A domain integral, such as that in Figure 2.10b, is easier for DIC methods as it reduces the noise sensitivity of the measurements.

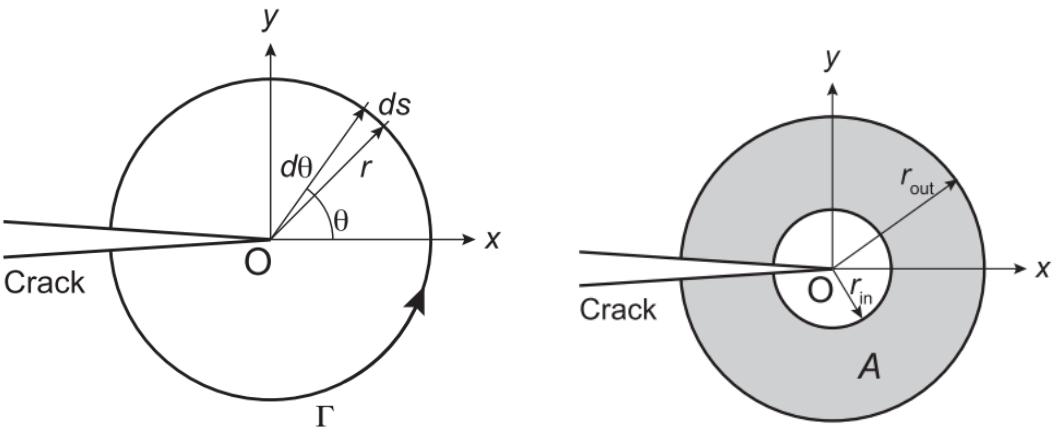

(a) Line J-integral marked by Γ [46]

(b) Domain J-integral marked by grey zone [46]

Figure 2.10 Representative crack tip in two-dimensions, where the x and y directions are marked. The stresses described by Equation 2.17 are along the x-axis. The J-integral is shown for the line and domain method.

For a crack lying on the x-axis, the domain integral is:

$$J = \int_A \left(W \frac{\partial q}{\partial x_i} - \sigma_{ij} \frac{\partial u_i}{\partial x} \frac{\partial q}{\partial x_j} \right) \mathrm{d}A \, (i, j = x, y) \,, \tag{2.21}$$

where A is an area surrounded by the two arbitrary contours around the crack tip, q is the arbitrary variable that satisfies $q = 0$ on the outer boundary and $q = 1$ on the inner boundary of the domain, defined as

$$q = \frac{r_o^2 - \left((x - x_0)^2 + (y - y_0)^2 \right)}{r_o^2 - r^2 i}, \tag{2.22}$$

where r_o and r_i are the radii of the outer and inner boundaries of the domain, respectively and x_0 and y_0 are the coordinates of the crack tip position [46]. Using DIC, the displacements are known and the strains can be calculated from the displacement. Then, the Ramberg-Osgood equation provides a relationship between the strains and their corresponding stresses. The components are written as

$$\epsilon_{ij} = \frac{1 + \nu}{E} s_{ij} + \frac{1 - 2\nu}{3E} \sigma_{kk} \delta_{ij} + \frac{3}{2} \alpha \epsilon_0 \left(\frac{\sigma_e}{\sigma_0} \right)^{n-1} \frac{s_{ij}}{\sigma_0} \, (i, j = x, y) \,, \tag{2.23}$$

where δ_{ij} is the Kronecker delta function, s_{ij} are the components of the stress deviator, σ_e is the von Mises equivalent stress, σ_0 and ϵ_0 are the yield stress and strain, α is the Ramberg-Osgood fitting constant and n is the hardening constant [46]. Then, the strain energy density is calculated as

$$W = \frac{1}{2E} \left[\sigma_e^2 + (1 - 2\nu) \left(\sigma_x \sigma_y - \tau_{xy}^2 \right) + 2 \frac{\alpha n}{n + 1} \sigma_e^2 \left(\frac{\sigma_e}{\sigma_0} \right)^{n-1} \right]. \tag{2.24}$$

The strain energy density can be inserted into Equation 2.21 to find the J-integral value. As noted above, the SIF can be found by inserting the J-integral value into Equation 2.20.

One advantage of using the J-integral rather than the theoretical and Williams methods is that it does not require precise knowledge of the crack tip location, a typically difficult task without microscopic imaging. However the method is susceptible to scatter, since the stresses and strains are calculated from the displacement data [41]. Another issue is that the J-integral was originally designed for monotonic loading, requiring a modification for cyclic loading to account for the unloading and crack closure effects caused by the reduction in load, which may create a residual compressive stress in the plastic zone [1]. The cyclic J-integral is primarily studied with regards to crack growth, where the integral value is obtained from the hysteresis loops recorded for two different crack lengths [1]. Currently, methods do not

exist for estimating the cyclic J-integral using DIC methods.

Other applications of DIC include monitoring crack growth, estimating the plastic zone size and crack opening displacements and obtaining the SEDD of notch roots. Mapping the plastic strain accumulation is a significant area of interest as it indicates crack propagation direction and crack growth. Using a microscope and stitching images together, Carroll tracked the strain localization and subsequent fatigue crack growth of a specimen through DIC as shown in Figure 2.11 [43].

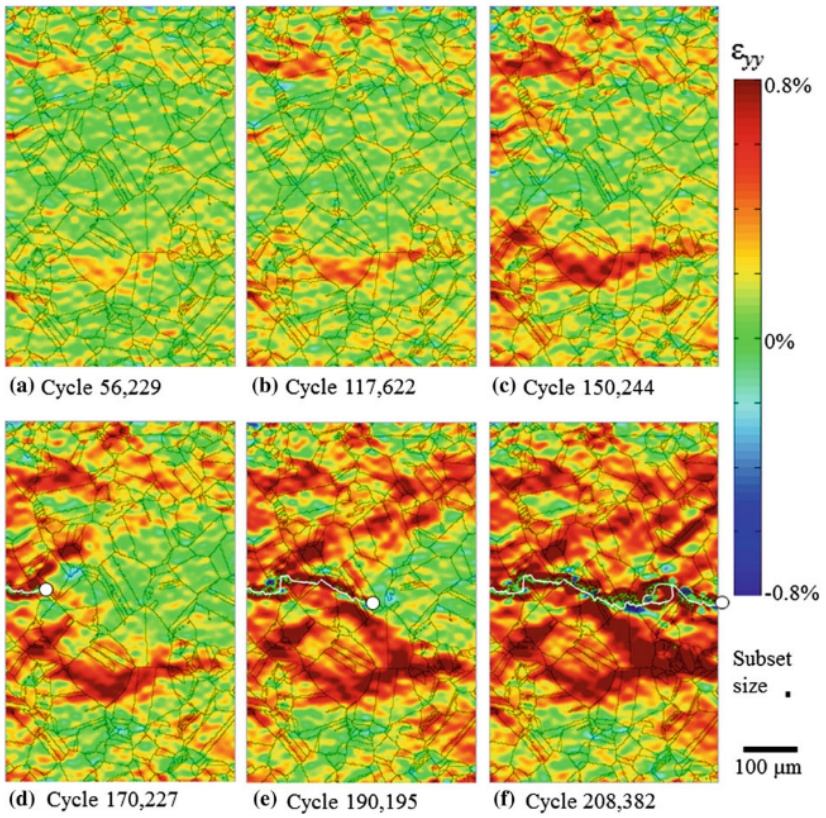

Figure 2.11 Strain field plots in the ϵ_{yy} direction at different cycle values, showing the strain lobes accumulated ahead of the crack (marked by white) [43].

In the figure, as the fatigue crack extends through the specimen, DIC shows there are two strain lobes leading the crack growth, which is in line with theoretical models. The appearance of shear strain localization zones ahead of the crack tip also is an indicator that has been used to predict fatigue crack growth [49]. Several studies examine the usage of DIC for estimating crack growth. One study extracted the crack tip location and displacements to find the corresponding SIF amplitude [12]. Another found the crack growth rate was approximately proportional to an integrated strain, or an area integral with a power law relationship with the SIF amplitude [50].

One study used notch roots to correlate the usage of strain energy density dissipated at notch roots to the energy based model in Section 2.2 [51]. In this study, the SEDD was found within a control volume around the tip of the notch, as shown in Figure 2.12.

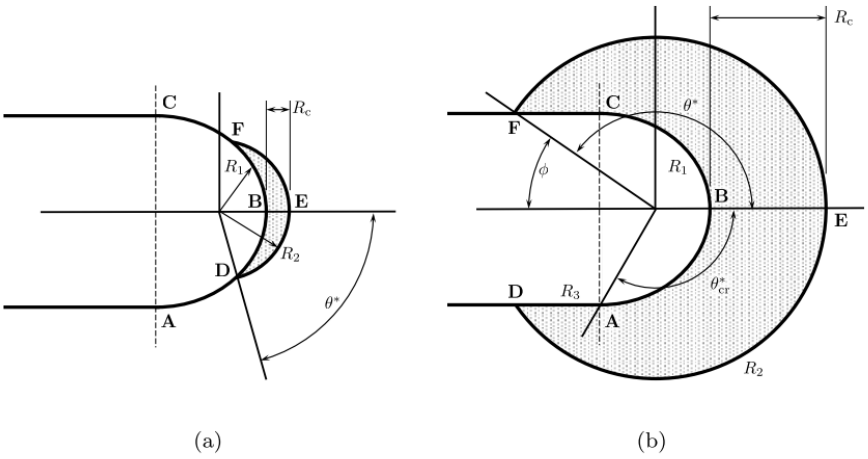

Figure 2.12 Control volumes for (a) high strength, brittle materials and (b) marginal, ductile materials used to study SEDD [51].

Then, the averaged strain energy in the control volume was calculated from the element strains found by DIC, and the results compared to theoretical calculations for the same specimen computed using finite element methods. The results showed good agreement, thus showing promise in using DIC to evaluate the SEDD during fatigue.

As demonstrated in this chapter, techniques to evaluate fatigue properties using SEDD and DIC have undergone significant advances. However, there are significant gaps remaining in our understanding and prediction of fatigue. This study will synthesize existing literature and develop a method to predict the fatigue life of nanocoated specimens at different stress levels, as well as obtain a new fatigue prediction parameter using DIC to predict impending failure.

Chapter 3

Experimental Procedures

Monotonic and fatigue tests were performed for this thesis to validate the fatigue prediction framework and to analyze the relation of full-field strain energy density measurements to the progression of fatigue damage.

3.1 Static and Fatigue Testing

Tests were run on a MTS 880 load frame with a 100 kN capacity. The load frame was controlled using MTS Series 793 Control Software and MTS Model 793.10 Multipurpose Testware Software. Multipurpose Testware allows for fatigue tests to be run easily, as there is a programming function to vary the number of cycles, frequency, cycle shape, load levels and load compensators during the test, minimizing manual control over the test program. For monotonic tests, MTS Basic Testware was used to provide better control over the loading when the material properties were not well known.

Cylindrical threaded specimens and flat dogbone specimens were used. The load frame held the specimens using threaded inserts for the cylindrical threaded specimens and MTS 647.30 hydraulic wedge grips for the flat dogbone specimens. The threaded inserts were manufactured by Lilex Industries, a nearby machine shop. As the planned fatigue program did not include compressive testing, there was not a need to guard against backlash in the grips. The cylindrical specimens were used for validating the fatigue prediction framework, while the flat specimens were used to provide observations about the strain energy density dissipation during fatigue via digital image correlation. Drawings of these samples are shown in Figure 3.1 for the cylindrical specimen and Figure 3.2 for the flat dogbone sample.

The force data was obtained from a voltage output on the MTS Controller, while the strain data was obtained from Tokyo Measuring Instruments Lab F-series strain gauges mounted on the specimen. For the cylindrical specimens, four strain gauges were mounted

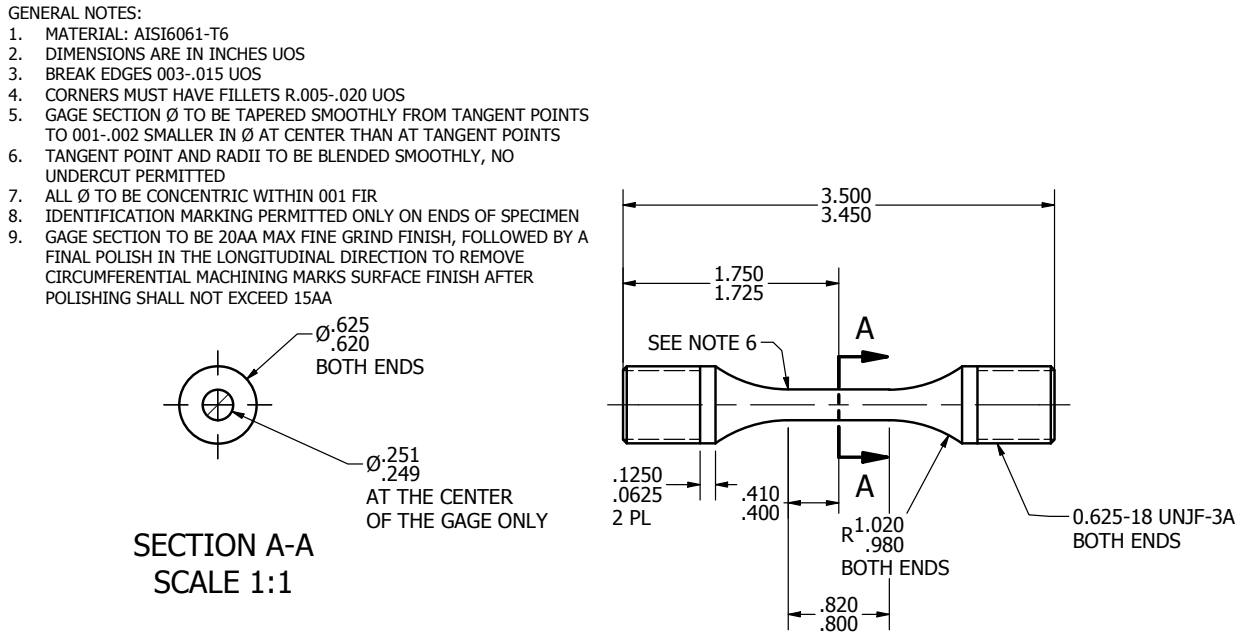

Figure 3.1 Cylindrical specimen drawing.

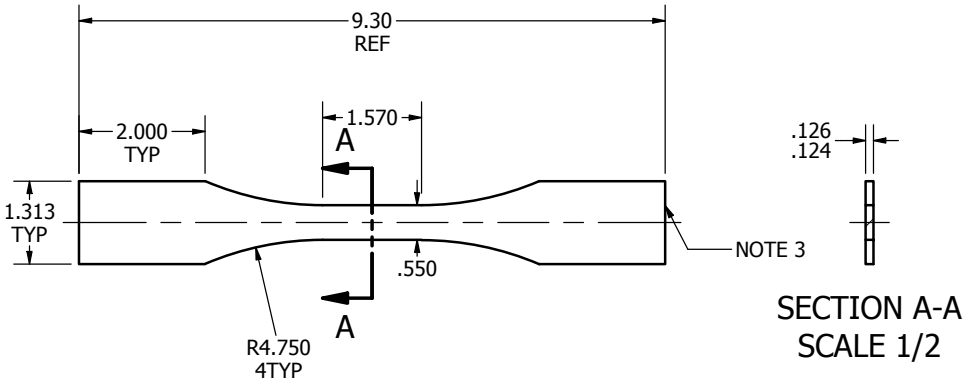

Figure 3.2 Flat dogbone specimen drawing.

90 degrees apart from each other in the longitudinal direction, to measure the axial strain and the effects of any bending strain. A laser extensometer also measured the specimen strain. At low strains the extensometer was severely affected by noise, thus limiting its use to measuring strains when the strain gauge limits were exceeded. A contact extensometer was also used for measurements but did not provide better measurements than the non-contact laser extensometer. In this thesis, the laser extensometer was used to measure the monotonic strain, while the strain gauges was used to measure the strain values during fatigue. The force and strain gauge data were then synthesized using a National Instruments Labview script.

The setup of the experiment for the cylindrical specimens is shown in Figure 3.3. The strain gauges, laser extensometer, threaded inserts and cylindrical specimen are indicated in the figure.

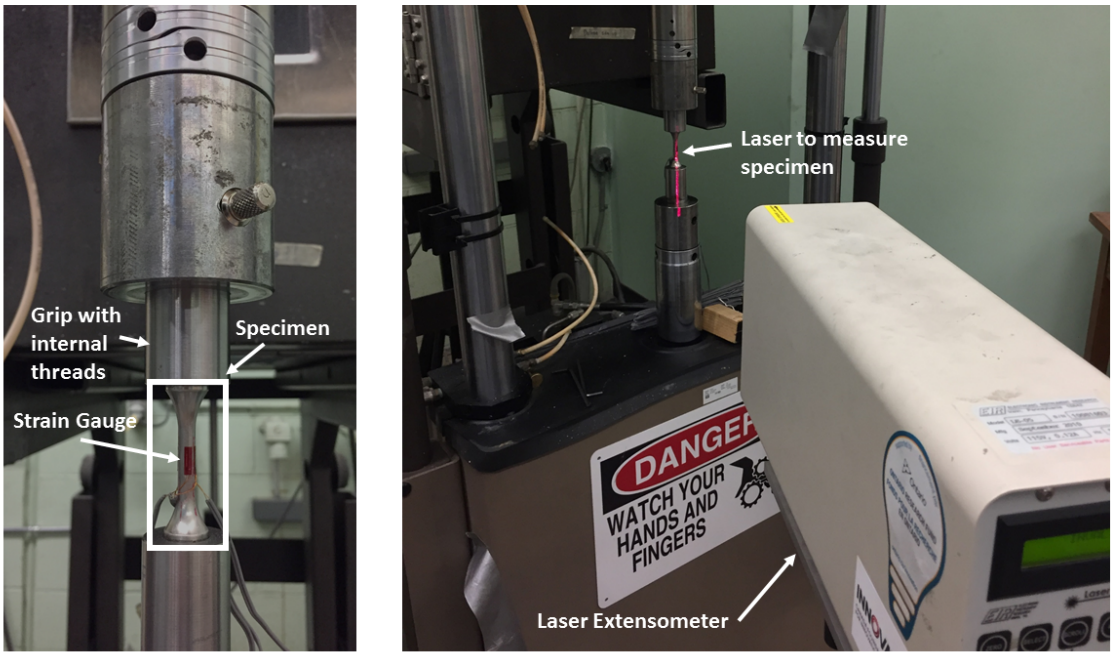

Figure 3.3 Experiment setup for cylindrical specimen.

Prior to loading the specimens, the load and strain source were zeroed. The specimen was then loaded to a point well below the known elastic limit to obtain the elastic modulus of the specimen. Then, the specimen was unloaded to zero load and the strain source rezeroed to ensure the test data would start at the origin.

For the monotonic tests, the elastic modulus properties were obtained by displacing the specimen up to 0.3% strain at strain rates below 0.015 mm/mm/min, then unloading the specimen. This process was repeated three times, as suggested by ASTM Standard E111-17

[52]. The tensile properties were obtained by straining the specimen at a rate below 0.015 mm/mm/min until the material was evidently yielded, then the strain rate was increased to a rate no higher than 0.5 mm/mm/min until fracture.

For the fatigue tests, an initial set of tests was run at 1.5 Hz, where the measurements were taken at 0.05 Hz. A later set of tests was run at 10 Hz to reduce testing times, while measurements were still taken at 0.05 Hz. Increasing the loading frequency did not cause any observable differences in the fatigue results. The measurements were taken at arbitrarily determined intervals, where measurement frequency increased at the initial stages of fatigue and at the end of fatigue, in order to optimize test time while obtaining sufficient fatigue information for analysis.

3.2 Digital Image Correlation Measurements

The DIC measurements were obtained using a separate system, where a Point Grey GRAS-50S5M-C camera was used in conjunction with a Tamron 90 mm F/2.8 Macro lens to obtain images. A two-source fibre optic light was used to ensure uniform lighting. This camera was controlled using Correlated Solutions Vic-Snap software. A speckle pattern was applied to the specimen to allow the DIC software to correlate the specimen displacement. The speckle pattern base was painted using Rust-Oleum Flexidip Matte White spray paint and the speckle pattern dots were spray-painted using Rust-Oleum Specialty High Heat black paint. Prior to testing, a ruler was placed on the specimen to calibrate the image scale. The displacement and strain maps were calculated using Correlated Solutions Vic-2D software and exported as text files for further data processing. The experimental setup for digital image correlation is shown in Figure 3.4.

In DIC, several parameters affect the quality of the measurements, including geometrical distortions, speckle size and density and correlation size and density. The camera was aligned 90 degrees to the specimen and ground reference using a combination of levels and rulers in order to prevent distorted measurements. Widely accepted standards on the speckle size and density painted on the specimen do not exist, therefore the speckle pattern was painted to approximately 50% density of black dots. Literature indicates that the subset and step size used for correlation is also critical to resolution, but as with the speckle pattern, standards for obtaining optimal measurements do not exist. The correlation values were based on a similar experiment by Celli [28], where the optimal correlation had a subset size of 29 and step size of 7.

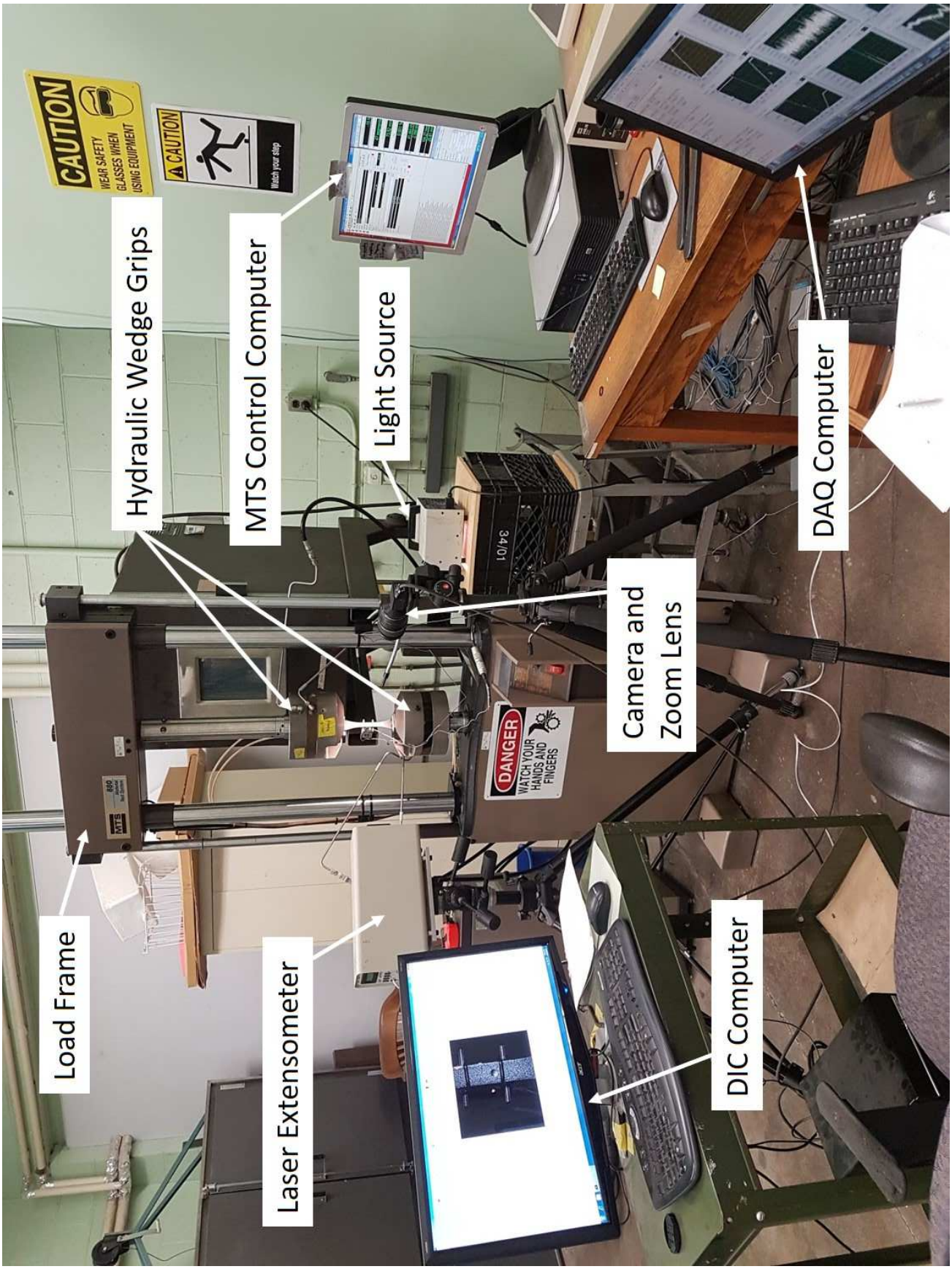

Figure 3.4 Experimental setup for digital image correlation, obtained with permission from K. Daley

Chapter 4

Energy-Based Prediction for Coated Specimens

As described in Chapter 1, one of the goals of this thesis was to expand the current energy-based fatigue prediction theory to include fatigue life predictions for coated specimens when loaded at different stress ratios. This chapter first describes the modifications to the theory necessary to make such predictions. Next, the material properties obtained by static tests are presented. Then, the fatigue results are presented. The predictions made using the fatigue prediction framework are compared to the measured fatigue lives.

4.1 Coated Specimen Fatigue Prediction Theory

The fatigue prediction framework is based on the energy-based method developed by Shen and Akanda [23]. This method assumes the total cyclic strain energy density dissipation (SEDD) is equivalent to the SEDD to induce monotonic rupture. The method uses the average strain range to calculate the cyclic SEDD via a power-law relation, making it independent of the test frequency.

4.1.1 Predicting Fatigue Life at Varying Stress Ratios

The Shen-Akanda method can only be used to predict fatigue life for stress ratios of R = -1.0. At higher stress ratios, the framework needs to account for the difference in SEDD caused by the mean stress. This chapter proposes a variation of the Scott-Emuakpor correction [26] to accommodate these differences. The correction is required to account for the decrease in total energy dissipated in fatigue when a mean stress is present and the increase in cyclic energy dissipation caused by the greater plastic strain. The decrease in total energy required

for fatigue when a mean stress is present is shown in Figure 4.1.

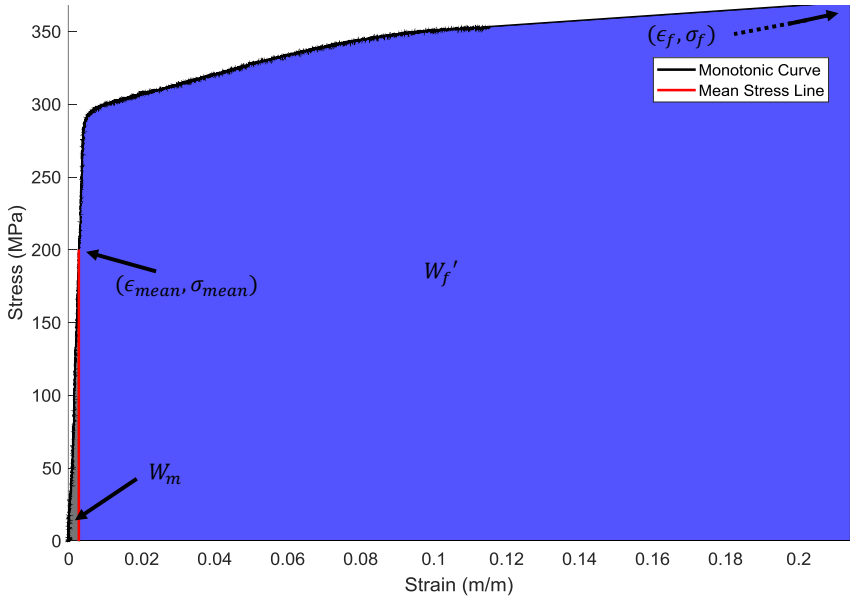

Figure 4.1 Example monotonic stress-strain curve with the mean stress reduction marked. The recorded data for one of the test specimens is shown, where the smooth line indicates the straight-line approximation to the fracture point. The figure magnifies the first part of the curve so the fracture point is not shown. Adapted from [26].

For specimens with a stress ratio of R = -1.0, the total SEDD dissipated at fatigue fracture, W_f, is equivalent to the total energy dissipation for monotonic fracture. This monotonic SEDD is defined by Scott-Emuakpor as the area under the true stress-logarithmic strain curve [26], which is the sum of the areas W_m and W_f' shown in Figure 4.1. If the experimental data for the stress-strain curve is known, the SEDD can be integrated directly from the data. Otherwise, if the experimental curve is not known but the Ramberg-Osgood parameters for the stress-strain curve are known, the SEDD prior to the point of specimen necking can be calculated by an integration of the Ramberg-Osgood equation. The Ramberg-Osgood equation is

$$\epsilon = \frac{\sigma}{E} + \left(\frac{\sigma}{K}\right)^{\frac{1}{n}}, \tag{4.1}$$

where σ and ϵ represent the stress and strain, respectively, E represents the elastic modulus, and n and K are curve-fit parameters.

The onset of specimen necking is commonly defined as the maximum point on the nominal stress-nominal strain curve. The stress level is also referred to as the necking stress. From this point until specimen rupture, which is defined by complete specimen separation, material instability causes a disproportionate localized cross-sectional area reduction and the stresses in the specimen are not easily measured. A straight line approximation is used to define the

stress-strain relationship between the two points. Then the total SEDD dissipated at fatigue fracture is calculated by integrating the area under the Ramberg-Osgood stress-strain curve and adding the area under the straight line approximation, such that

$$W_f = \sigma_n \epsilon_n - \frac{\sigma_n^2}{2E} - \frac{\sigma_n^{\left(1+\frac{1}{n}\right)}}{\left(1+\frac{1}{n}\right) K^{\frac{1}{n}}} + \frac{\sigma_n + \sigma_f}{2} \left(\epsilon_f - \epsilon_n\right), \tag{4.2}$$

where σ_n, σ_f, ϵ_n and ϵ_f indicate the necking and fracture stresses and strains, respectively.

When a mean stress is applied, W_f is reduced, since there is a constant static load applied to the specimen. The reduction is shown by the small grey region on the left in Figure 4.1, where the red line denotes the mean strain line for a given mean stress. The reduction is termed the mean stress reduction and is denoted by W_m. This point can be directly obtained from the area under the experimental curve or from Ramberg-Osgood parameters if the experimental curve is not available.

If the mean stress is less than the necking stress, W_m is calculated as

$$W_m = \sigma_m \left(\epsilon_m - \frac{\sigma_m}{2E}\right) - \frac{\sigma_m^{1+\frac{1}{n}}}{\left(1+\frac{1}{n}\right) K^{\frac{1}{n}}}, \tag{4.3}$$

where the mean stress is indicated by σ_m. If the mean stress is greater than the necking stress, Equation 4.3 needs to be modified to include the curve described by the straight-line approximation. Since the mean stresses in this thesis were less than the necking stress, these modifications are not discussed. The revised W_f value is marked by the blue region in Figure 4.1 and is calculated by

$$W_f' = W_f - W_m, \tag{4.4}$$

where the prime indicator is for the total SEDD after correcting for mean stresses.

The graphical description for the Shen-Akanda cyclic SEDD expression with a zero mean stress and a positive mean stress is shown in Figure 4.2. The relation for fully-reversed cycling is represented by the red line, where the point of minimum stress and strain is located at the origin. The tensile stress-strain relationship is assumed to follow the Ramberg-Osgood stress-strain description. The maximum point is at $(\epsilon_{pp}, \sigma_{pp})$, where σ_{pp} indicates the peak-to-peak stress, or double the stress amplitude, and ϵ_{pp} is for the peak-to-peak strain. For the purposes of simplicity, the compressive stress-strain relation is assumed to be a mirror image of the tensile stress-strain relation, assuming negligible Bauschinger effect.

Assuming the stress amplitude is constant and keeping the generalized coordinate system, if a tensile mean stress is applied to the specimen, the maximum stress will increase by the mean stress value. Then the maximum point of the curve with the mean stress will become

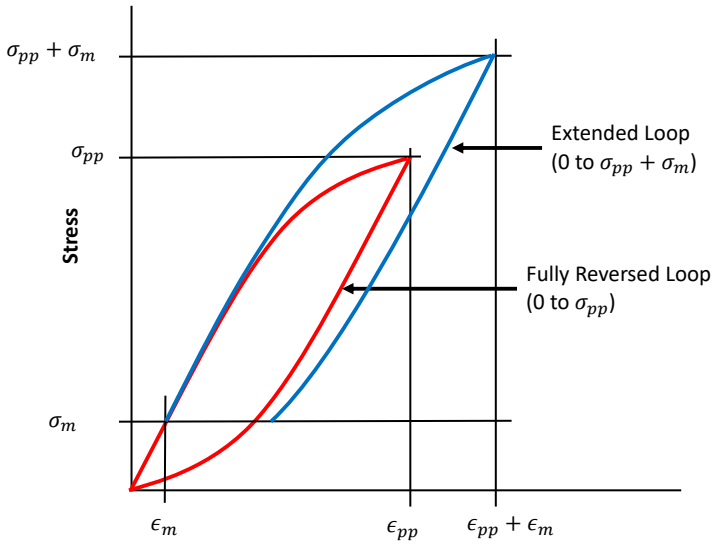

Figure 4.2 Cyclic stress-strain curve with the fully-reversed loop marked in red and the hysteresis loop for cycling with mean stresses marked in blue. Adapted from [26].

$(\epsilon_{pp} + \epsilon_m, \sigma_{pp} + \sigma_m)$, where the mean stress and strain terms are added to the maximum point. This increase in the maximum point is equivalent to extending the original hysteresis loop shape due to the increased plastic deformation. In order to keep the stress amplitude the same, the new loop needs to have the same minimum. The bottom section of the loop is "cut-off" at the minimum stress level, creating an open loop shown by the blue line in Figure 4.2. The minimum stress value is equal to the increase in the maximum stress. The increase in the maximum stress is equivalent to the mean stress, thus the mean stress value is marked on the stress axis. This open-ended behaviour was confirmed by experimental data and by Scott-Emuakpor [26] (see Figure 2.6).

As an example, if a specimen is tested with a stress amplitude of 300 MPa for a mean stress of zero, the hysteresis loop would be translated to the generalized coordinate system so the minimum point is at the origin, (0,0), and the maximum point is at the peak-to-peak stress, (0.6% strain, 300 MPa). The strain value is arbitrarily selected for the purposes of this example. Then, if the mean stress was increased to 150 MPa, the new maximum point would be at (1.0% strain, 450 MPa), but the new minimum must compensate to keep the stress amplitude the same. By setting the new minimum point at 150 MPa, the conditions are satisfied.

To calculate the cyclic SEDD, the hysteresis loop is integrated. The cyclic SEDD for fully-reversed cycling, W_c, is:

$$W_c = \sigma_{pp}\epsilon_{pp} - 2\int_0^{\sigma_{pp}} \epsilon \mathrm{d}\sigma. \tag{4.5}$$

For cycling with mean stresses, the integration limits change, such that the cyclic SEDD for non-zero mean stresses, W_c', becomes

$$W_c' = \sigma_{pp}\left(\epsilon_{pp} + \epsilon_m\right) - \int_{\sigma_m}^{\sigma_{pp}+\sigma_m} \epsilon \mathrm{d}\sigma - \int_0^{\sigma_{pp}} \epsilon \mathrm{d}\sigma. \tag{4.6}$$

By incorporating the Ramberg-Osgood stress-strain relationship into Equation 4.6 and integrating, the relation for SEDD during fatigue cycling with mean stresses becomes

$$W_c' = \sigma_{pp}\left(\frac{\sigma_{pp}+\sigma_m}{E} + \left(\frac{\sigma_{pp}+\sigma_m}{K}\right)^{\frac{1}{n}}\right) - \frac{\left(\sigma_{pp}+\sigma_m\right)^2}{2E} - \frac{\left(\sigma_{pp}+\sigma_m\right)^{1+\frac{1}{n}}}{K^{\frac{1}{n}}\left(1+\frac{1}{n}\right)} + \frac{\sigma_m^2}{2E} + \frac{\sigma_m^{1+\frac{1}{n}}}{\left(1+\frac{1}{n}\right)K^{\frac{1}{n}}} - \frac{\sigma_{pp}^2}{2E} - \frac{\sigma_{pp}^{1+\frac{1}{n}}}{\left(1+\frac{1}{n}\right)K^{\frac{1}{n}}}. \tag{4.7}$$

After combining and rearranging the terms, the equation is simplified to

$$W_c' = \frac{\left(\sigma_{pp}+\sigma_m\right)^{\frac{1}{n}}\left(\frac{\sigma_{pp}}{n} - \sigma_m\right)}{K^{\frac{1}{n}}} + \frac{\sigma_m^{1+\frac{1}{n}}}{K^{\frac{1}{n}}\left(1+\frac{1}{n}\right)} - \frac{\sigma_{pp}^{1+\frac{1}{n}}}{K^{\frac{1}{n}}\left(1+\frac{1}{n}\right)}. \tag{4.8}$$

As noted in the beginning of this section, the total SEDD in fatigue is equivalent to the monotonic SEDD. This relation can be expressed for non-zero mean stress fatigue cycling as

$$W_f' = NW_c', \tag{4.9}$$

where N is the number of cycles to failure and the prime values indicate the monotonic and cyclic SEDD values after accounting for the mean stress correction. By rearranging the terms in Equation 4.9 and inserting Equation 4.8, the cycles to failure can be predicted by

$$N = W_f'\left(\frac{\left(\sigma_{pp}+\sigma_m\right)^{\frac{1}{n}}\left(\frac{\sigma_{pp}}{n} - \sigma_m\right)}{K^{\frac{1}{n}}} + \frac{\sigma_m^{1+\frac{1}{n}}}{K^{\frac{1}{n}}\left(1+\frac{1}{n}\right)} - \frac{\sigma_{pp}^{1+\frac{1}{n}}}{K^{\frac{1}{n}}\left(1+\frac{1}{n}\right)}\right)^{-1}. \tag{4.10}$$

For most fatigue problems, the applied stress is known. Since the monotonic SEDD can be calculated from known stress-strain curves of the specimen material, the remaining parameters to be solved in Equation 4.10 are the Ramberg-Osgood curve fit parameters n and K. These are termed in this thesis as the fatigue prediction parameters (FPP) and can be calculated from closed-form equations for fully-reversed cycling if the strain range is known. These equations were shown by Shen and Akanda [23]. However, these closed-form equations do not work for cycling with mean stresses. Two open-form methods were

developed to obtain the FPP. These methods are called the strain range method and the life method.

The strain range method finds the FPP parameters by finding the parameters which calculate the closest strain range to the experimental strain range value. The closest strain range is defined as the minimum squared residual when a set of strain range values are calculated. The strain range is calculated using the Ramberg-Osgood expressions for the minimum and maximum strain. As noted earlier, the minimum strain of the extended hysteresis loop (loop which incorporates the mean stress effect) is equivalent to the mean strain. Therefore,

$$\epsilon_{mn} = \frac{\sigma_m}{E} + \left(\frac{\sigma_m}{K}\right)^{\frac{1}{n}}, \tag{4.11}$$

where ϵ_{mn} is the minimum strain and σ_m is the mean stress. The maximum strain is equivalent to the peak-to-peak strain plus the mean strain,

$$\epsilon_{mx} = \epsilon_{mn} + \epsilon_{pp} = \frac{\sigma_m + \sigma_{pp}}{E} + \left(\frac{\sigma_m + \sigma_{pp}}{K}\right)^{\frac{1}{n}}. \tag{4.12}$$

The strain range equation is then expressed as the difference between the maximum and minimum strain,

$$\Delta\epsilon = \frac{\sigma_{pp}}{E} + \left(\frac{\sigma_m + \sigma_{pp}}{K}\right)^{\frac{1}{n}} - \left(\frac{\sigma_m}{K}\right)^{\frac{1}{n}}. \tag{4.13}$$

The FPP are found from Equation 4.13 by minimizing R in the expression,

$$R = \sum_{i=1}^{m} \left(\Delta\epsilon_i - f(\sigma_{pp_i}, \sigma_{m_i}, n, K, E_i)\right)^2, \tag{4.14}$$

where m is the number of strain values used in the minimization function, the measured strain range is $\Delta\epsilon_i$ and $f(\sigma_{pp_i}, \sigma_{m_i}, n, K, E_i)$ is Equation 4.13.

Section 4.4 shows the strain range method is sensitive to variations in the strain measurements and does not always converge to reasonable FPP values. As an alternative method, called the life method, was used to find the FPP. The fatigue life was used in the place of the strain range in the minimization function, by minimizing R in the expression

$$R = \sum_{i=1}^{m} \left(N_i - f(\sigma_{pp_i}, \sigma_{m_i}, n, K, W_f)\right)^2, \tag{4.15}$$

where N_i represents the experimental fatigue life and $f(\sigma_{pp_i}, \sigma_{m_i}, n, K, W_f)$ represents Equation 4.10, the equation which calculates the fatigue life of a specimen with known loading conditions. After the FPP were obtained using either of these two methods, the values were

inserted into Equation 4.10, along with the loading conditions, to obtain predictions of the fatigue life.

4.1.2 Fatigue Prediction for Coated Specimens

For coated specimens, the fatigue life prediction method needs to account for the separate effects of the substrate and coating materials. Although the combined coating-substrate system could be treated as a new material, this method would require new tests to define the material FPP whenever the specimen geometry changes, for example, if the coating thickness increases.

To obtain the effects of the substrate and coating, the force distribution must be known. As well, the FPP are needed for the coating and the substrate material. These values were obtained using the methods described in Section 4.1 and inserted into expressions based on Equation 4.10 for the coating and substrate to generate a fatigue life prediction. The following sections will describe the methods used to obtain the force distribution and residual stresses for the coating and substrate and the modifications to the original prediction methodology to account for the coating.

Calculation of Coating and Substrate Stresses

For these material systems, the material properties for the substrate were well-defined, but the properties for the coating were not, due to lack of literature data for nanocrystalline metals. As well, bulk nanocrystalline metal specimens were not available for testing, making it difficult to obtain a reference material dataset. The coating properties were found by using the known force applied to the specimen, the specimen geometry, the substrate stress-strain curve and the assumption that the substrate and coating strains were equivalent. This last assumption was valid since coating debonding was not observed in the specimens at the crack initiation points.

The first coating property calculated was the elastic modulus. If the specimen was not plastically deformed under load, the forces in the coating and substrate and the elastic modulus for the coating could be estimated based on Hooke's law. First, the stress in the substrate was found,

$$\sigma_{sb} = E_{sb}\epsilon_{sb}, \tag{4.16}$$

where the subscript *sb* is used for the substrate values. The force in the substrate is:

$$F_{sb} = \sigma_{sb}A_{sb}. \tag{4.17}$$

The forces in the coating and substrate sum to the total force, F_t. Thus the force in the coating is:

$$F_{ct} = F_t - F_{sb}. \tag{4.18}$$

The stress in the coating is:

$$\sigma_{ct} = \frac{F_{ct}}{A_{ct}}. \tag{4.19}$$

The subscript ct is used for the coating values. Then, the elastic modulus of the coating is:

$$E_{ct} = \frac{\sigma_{ct}}{\epsilon_{ct}}, \tag{4.20}$$

where ϵ_{ct} is equal to the overall strain measured on the specimen, which is equal to the strain in the substrate.

Since the experiments for this thesis stressed the specimens beyond the elastic limit, another method was needed to calculate the stresses in the coating and substrate. The stress in the substrate was found using the stress-strain curve obtained from the uncoated specimens. These specimens were made in the same manufacturing batch as the coated specimens and had the same specimen geometry. The stress-strain behaviour in the substrate was assumed to be unchanged with the addition of the coating. Therefore, for any given strain, the stress in the substrate could simply be read off the stress-strain curve. Then, since the forces in the substrate and coating must sum to the total force, the stress in the coating is:

$$\sigma_{ct} = \frac{F_t - \sigma_{sb}\left(\epsilon\right) A_{sb}}{A_{ct}}, \tag{4.21}$$

where $\sigma_{sb}\left(\epsilon\right)$ denotes the stress in the substrate at a given measured strain on the substrate stress-strain curve.

To find the stresses when the specimen was unloaded after yielding, a straight line unloading curve was assumed from the maximum load point. Assuming the elastic modulus for the substrate remained constant, the stress in the substrate for a known strain after the specimen is unloaded is:

$$\sigma_{sb} = \sigma_{mx_{sb}} - E\left(\epsilon_{mx} - \epsilon\right), \tag{4.22}$$

where $\sigma_{mx_{sb}}$ and ϵ_{mx} indicate the substrate maximum stress and strain after yield and ϵ indicates the unloading strain. The unloading strain is defined as the measured strain when the specimen is in the unloading phase of a load cycle. This term is associated with the change in strain for a given stress due to metal plasticity. The corresponding stress in the coating at this point was

$$\sigma_{ct} = \frac{F_t - \sigma_{sb} A_{sb}}{A_{ct}}. \tag{4.23}$$

Correction for Residual Stresses

When the stress-strain curves for the coating were initially calculated, non-linearities were observed in the stress-strain curves, which are inconsistent with known material behaviour. An example of these non-linearities is shown inside the circled point in Figure 4.3 for an aluminum (Al) specimen coated with nanocrystalline nickel cobalt (nNiCo). In this example, the stress-strain relations for both the coating and substrate are shown. The aluminum behaviour is well-defined and used as the reference curve. The nNiCo stress-strain curve is calculated using the methods from the previous section. This non-linearity was attributed to residual stresses.

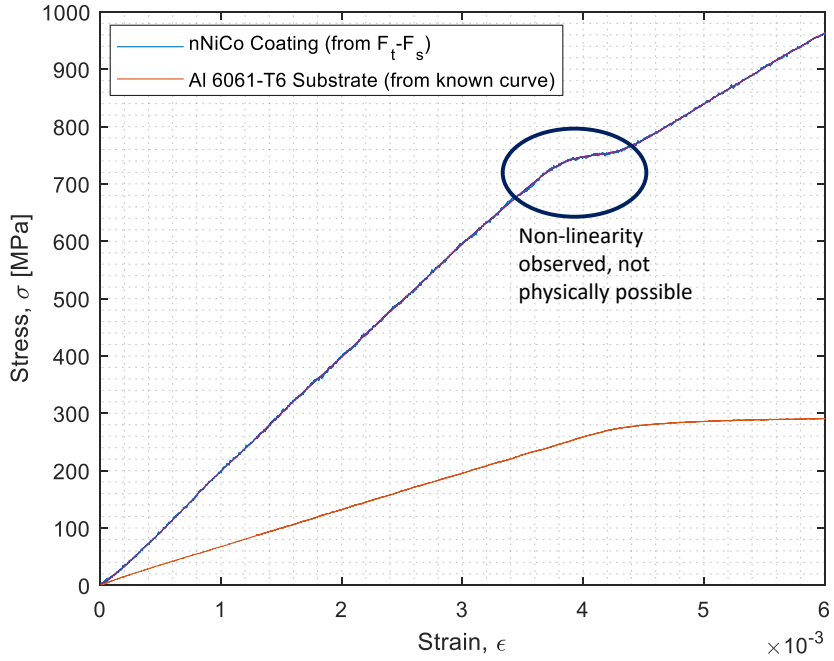

Figure 4.3 Example of the non-linearity occurring in the coating stress-strain curve of nNiCo. This non-linearity is inconsistent with known metal behaviour.

Residual stresses are internal stresses that remain within the coating and substrate after the manufacturing process, in the absence of external forces or thermal gradients [53]. These internal stresses are caused by mismatches in the elongation of two different materials. As stated above, the coating strain is equivalent to the substrate strain. Thus, when mismatches in the elongation occur between two materials, opposing internal stresses must occur to keep the strains equivalent. These mismatches occur due to several reasons, including but not limited to, distortion due to differences in the lattice parameters at the substrate-coating interface, thermal stresses caused by differences in the thermal coefficient of expansion between the substrate and the coating and stresses caused by particular plating conditions or

bath compositions [54].

An iterative method was developed to estimate the residual stress values, which were previously unknown, to obtain accurate stress-strain behaviour. This method uses the plastic deformation behaviour of the substrate to estimate the stress in the coating. The initial method to find the stresses in the substrate and coating assumed residual stresses did not exist in the coated system. As such, both substrate and coating stress-strain curves crossed the strain axes at the origin. However, if there was a residual stress in the specimen, the stress in the substrate at zero strain would become non-zero. The stress in the coating would correspondingly become non-zero to equilibrate the substrate load. Since the actual stress-strain behaviour in the substrate does not change, that is, the modulus, yield and ultimate strength values are the same, this would mean that the strain value of the substrate has shifted. Graphically, this means the stress-strain curve is translated along the strain axis. The residual stresses are assumed to lie between the compressive and tensile yield strengths, thus only elastic effects are considered. The substrate stress-strain curve is shifted until the curvature for the coating stress-strain curve represents expected metal stress-strain behaviour. An example of a tensile substrate residual stress and the consequent effects on the coating stress-strain behaviour is shown in Figure 4.4.

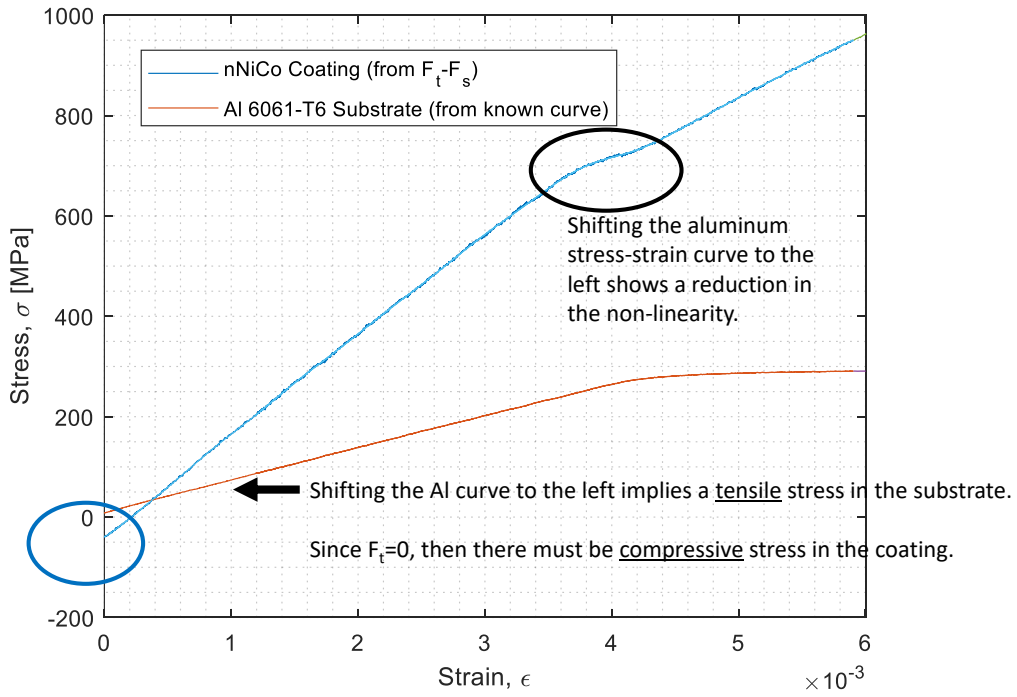

Figure 4.4 Reduction of the non-linearity occurring in the coating stress-strain curve of nNiCo, shown originally in Figure 4.3.

In Figure 4.4, the substrate reference curve is shifted to the left, thus creating a tensile

residual stress at zero overall strain. Overall strain is defined as the measured strain in the specimen. Since shifting the substrate curve causes a corresponding decrease in the non-linearity located at the black circle, this indicates a better estimate of the coating behaviour. This shift of the material curve along the strain axis is how the iterative solver finds the best estimate of the coating stress-strain behaviour. The solver obtains the substrate stress-strain behaviour at a given strain shift, then calculates the corresponding coating stress-strain behaviour using the equations in Section 4.1.2.

An example of the non-linearity removed is shown in Figure 4.5 by the black circle, indicating the best estimate of the coating stress-strain behaviour, compared to the inferred coating behaviour shown in Figures 4.3 and 4.4.

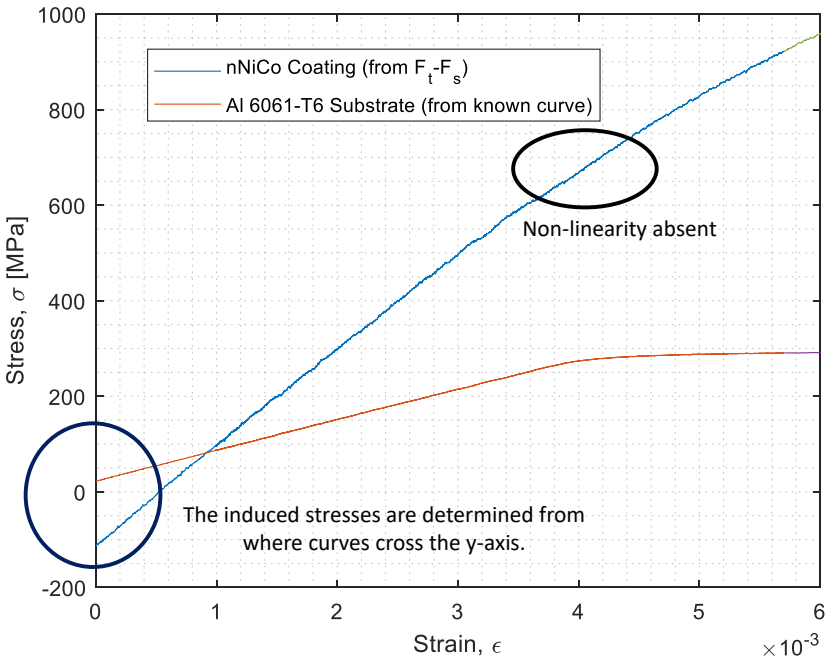

Figure 4.5 Example of the absent non-linearity for the nNiCo coating stress-strain curve.

Figure 4.6 shows the relationship between the curvature of the coating stress-strain curve to the translation of the substrate stress-strain curve. The minimum point of this curve represents the point at which the coating stress-strain behaviour is deemed the most realistic. The abscissa shows the amount of strain by which the substrate curve is shifted, where zero strain represents no shift to the curve. The ordinate is the curvature, defined by the sum of the squared second derivative of the coating stress-strain curve,

$$c = \sum \left(\frac{\partial^2 \sigma_c \epsilon}{\partial^2 \epsilon} \right)^2, \tag{4.24}$$

where c is the summed curvature and $\frac{\partial^2 \sigma_c \epsilon}{\partial^2 \epsilon}$ is the second derivative of the coating stress-strain curve.

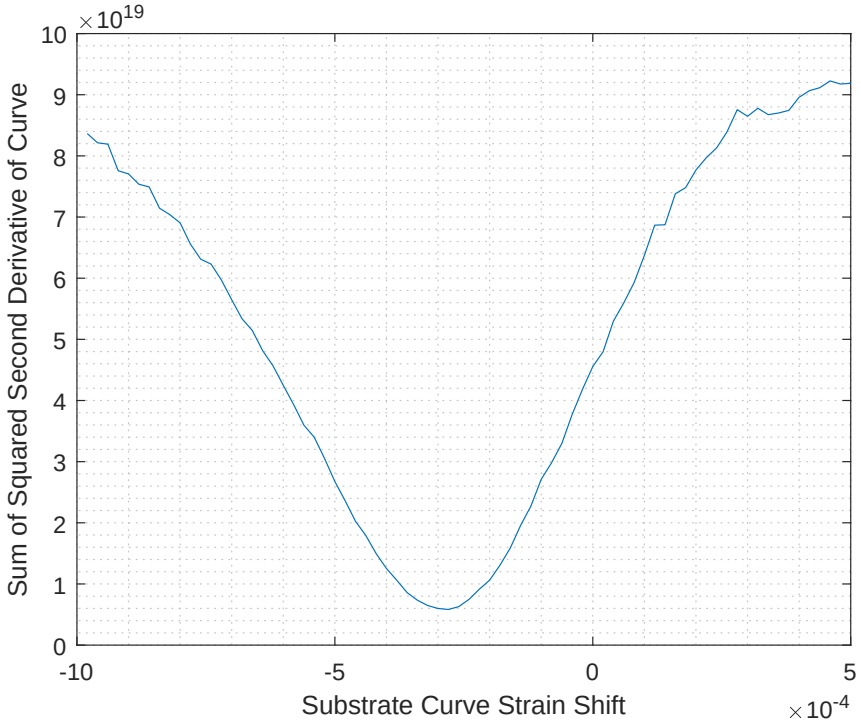

Figure 4.6 The relationship between the nNiCo stress-strain curvature and the amount the substrate stress-strain curve was shifted in the above example.

The residual stresses are determined from the points where the curves cross the vertical stress axis. In this example, a tensile residual stress is inferred for the aluminum and a compressive residual stress is inferred for the nNiCo. Note the magnitude of residual stresses is a function of the coating-substrate area ratio. In this case, the coating area was an order of magnitude smaller than the substrate area, resulting in a significantly higher coating residual stress to equilibrate the substrate residual stress.

Incorporating Coating Effects into the Fatigue Prediction Method

Experimental data and literature indicate that for most cases, either the substrate or the coating will fail first. Once one of the components fails, a rapid stress overload is assumed to act on the other component, which will fail immediately. The substrate and coating fatigue lives are examined separately using Equation 4.10. The fatigue life prediction is taken from the relation which predicts the lower fatigue life. Note that this method requires the parameters entered into the fatigue life prediction to be independent of the observed fatigue life. Therefore, only the strain range method can be used to obtain the FPP. However, the

life method is also used to obtain FPP to determine the accuracy of estimates when the component which fails first is known. This provides insight into whether using this method when the failure mode is known is feasible. As well, using this method provides insight into whether the presumed mode of failure is correct, as the accuracy using the presumed mode of failure should be higher than when incorrectly presuming the mode of failure (that is, if the failure is presumed to occur first in the coating, the prediction accuracy when considering the coating energy should be better than the prediction accuracy when considering the substrate).

4.2 Material Properties

Al 6061-T6 and nNiCo-coated Al 6061-T6 cylindrical and flat specimens were tested. This section presents the material obtained in static testing. These material properties are used in both this chapter and the following chapter.

4.2.1 Al 6061-T6 properties

The properties of Al 6061-T6 were measured via monotonic tensile tests. The elastic modulus was measured from the stress-strain data between 0.15% to 0.25% strain along an unloading curve. The yield strength was obtained via the 0.2% offset method, as described by ASTM E8/E8M [55]. The ultimate tensile strength was also obtained using the methods described by ASTM E8/E8M. The average properties with their corresponding standard deviations are listed in Table 4.1 and are similar to data from literature, with the exception of the elastic modulus of the cylindrical specimen, which is lower than the typical value. This value is listed typically in literature as 68 - 69 GPa [56, 13]. It is unclear why the experimental results showed a lower value. The cylindrical and flat dogbone specimens were obtained from two different suppliers. The cylindrical specimen supplier performed a strain relief procedure on their specimens, which may explain the lower strength values.

Table 4.1 Monotonic Properties for Cylindrical and Flat Al 6061-T6 Specimens

Property Type	**Cylindrical Specimens**	**Flat specimens**
Yield Strength (MPa)	294 ± 5	304 ± 4
Ultimate Tensile Strength (MPa)	318 ± 8	349 ± 2
Elastic Modulus (GPa)	66.5 ± 0.8	71 ± 0.2
Strain Energy Density (MJ/m^3)	319 ± 56	97 ± 18

The calculation for the logarithmic strain (ϵ_t) is

$$\epsilon_t = \ln\left(\epsilon_E + 1\right), \tag{4.25}$$

where ϵ_E is the nominal (engineering) strain value. This value was used up to the necking point.

The "true" stress, σ_t, up to the necking point was calculated as the force divided by the instantaneous area, approximated using conservation of volume theory [57]. This method was used to ensure consistency in measurements between this thesis and the literature this thesis is based upon [58]. To convert to this value from the measured nominal (engineering) stress (σ_E),

$$\sigma_t = \sigma_E\left(\epsilon_E + 1\right). \tag{4.26}$$

The logarithmic strain and "true" stress relation will be referred to as the true stress-strain relationship from this point forward. For the post-necking behavior, a straight line approximation was made between the necking value and the fracture point. A MATLAB script was used to measure the fracture area from images obtained by scanning electron microscopy. The strain and stress at the fracture point were determined based on the specimen area after fracture using,

$$\epsilon_f = \ln\left(\frac{A_0}{A_f}\right), \tag{4.27}$$

$$\sigma_f = \frac{F_f}{A_f}, \tag{4.28}$$

where A_0 is the original measured area, A_f is the fracture area, ϵ_f is the fracture strain and F_f is the force at failure. A comparison between the nominal and true stress-strain curves for a representative round Al 6061-T6 specimen is shown in Figure 4.7.

In the figure, the straight line approximation from the necking point to the final fracture point is shown, where there is a non-tangential transition between this line and the stress-strain relation up to the necking point. The monotonic strain energy is determined from the plot by integrating the true stress-strain curve,

$$W_f = \int_0^{\epsilon_f} \sigma \mathrm{d}\epsilon. \tag{4.29}$$

There is a large difference between the SEDD measured for the cylindrical and flat specimens. The most likely explanation is the difference is caused by specimen geometry. The flat specimen has sharp corners leading to local increases in stress intensity, compared to the lack of these in the cylindrical specimens. As a result, the flat specimen likely experienced

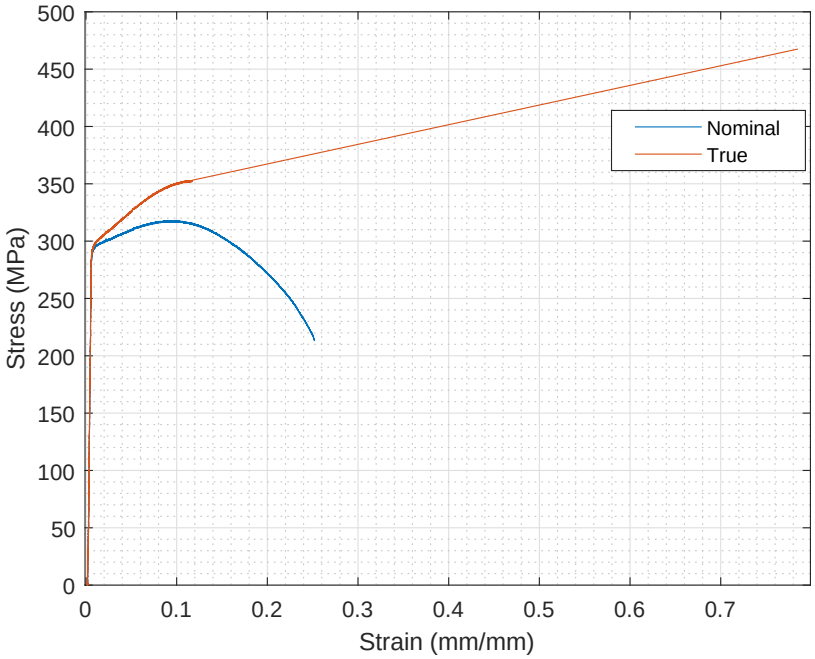

Figure 4.7 Nominal and true stress-strain curve Al 6061-T6. The behaviour in the true stress-strain curve is approximated from the necking point to the fracture point, and may not be tangent to the curve prior to the necking point.

local stress overloads, leading to earlier fracture. The cylindrical SEDD values are similar to those found by Celli [28], who also used cylindrical specimens. However, this reported value varies widely in literature for this material. As an example, Letcher found energy dissipation values which were approximately 30% lower than Celli's [7]. The uncertainty in the measurement is also high. The percentage uncertainty of both specimen types is similar, around 18%. The uncertainty may be due to microstructural differences between specimens, where small flaws in one specimen cause earlier fracture than for another specimen.

4.2.2 nNiCo properties

A nNiCo-coated Al 6061-T6 specimen was also loaded quasi-statically to rupture to obtain the nNiCo material properties. The NiCo properties were interpreted from the coated material using the methods described in Section 4.1.2, as bulk specimens were not available for testing. The Al 6061-T6 properties from Section 4.2.1 are assumed to represent the substrate accurately.

The baseline thickness for the nNiCo coating on the cylindrical specimens was 250 µm to correspond with an intended total specimen diameter of 6.35 mm (0.25 inch). However, the measured coating thicknesses varied significantly from the intended thickness. The mea-

sured thicknesses for the cylindrical specimen are listed in Table 4.2, with a measurement uncertainty of 5 µm.

Table 4.2 Measured coating thickness of nNiCo coatings on cylindrical specimens, where the intended thickness was 250 µm

ID	Coating Thickness (µm)	ID	Coating Thickness (µm)
B1	302	B13	270
B2	307	B15	310
B3	293	B16	313
B6	322	B17	292
B7	280	B18	263
B11	305		

The values of the properties measured are compared with the values provided by the manufacturer in Table 4.3. Figure 4.8 shows the calculated nominal and true stress-strain curves of both the nNiCo and Al 6061-T6 during a monotonic test for the coated specimen. The curves include the effects of residual stress, which was -31 MPa for the substrate and 268 MPa for the coating. Due to resource constraints, only one specimen was statically tested. Uncertainty values are not provided for the ultimate tensile strength and the SEDD. As well, note the end behaviour of the true nNiCo stress-strain curve. The force at fracture was assumed to be the remainder of the force in the specimen after accounting for the force in the substrate. The aluminum stress at fracture was assumed to be equivalent to 362 MPa leaving a remaining force in the coating equivalent to 114 MPa. This nNiCo stress value is significantly less than the stress at where the specimen is assumed to "neck" and contradicts known metal behaviour, where the true stress at fracture should exceed that at the necking point. This deviation from the known behaviour is shown by the dashed line. It is unclear what the cause of this reduced "fracture stress" is and further investigation is required to clarify whether this is an effect of the coated specimen or if it represents the actual nNiCo behaviour. As a more representative estimate of the nNiCo behaviour, a straight line estimate parallel to the tangent at the necking point was taken up to the point of the fracture strain and is assumed to represent the actual behaviour. This estimate is shown by the solid line in the figure. The value used to obtain nNiCo montonic SEDD is the area below this stress-strain curve.

Table 4.3 Tensile Properties for nNiCo

Property Type	**Measured Values**	**Manufacturer Values**
Yield Strength (MPa)	1304	900 - 1200
Ultimate Tensile Strength (MPa)	2061	1400 - 1700
Elastic Modulus (GPa)	186.7 ± 3.4	135 - 165
Strain Energy Density Range (MJ/m^3)	201	N/A

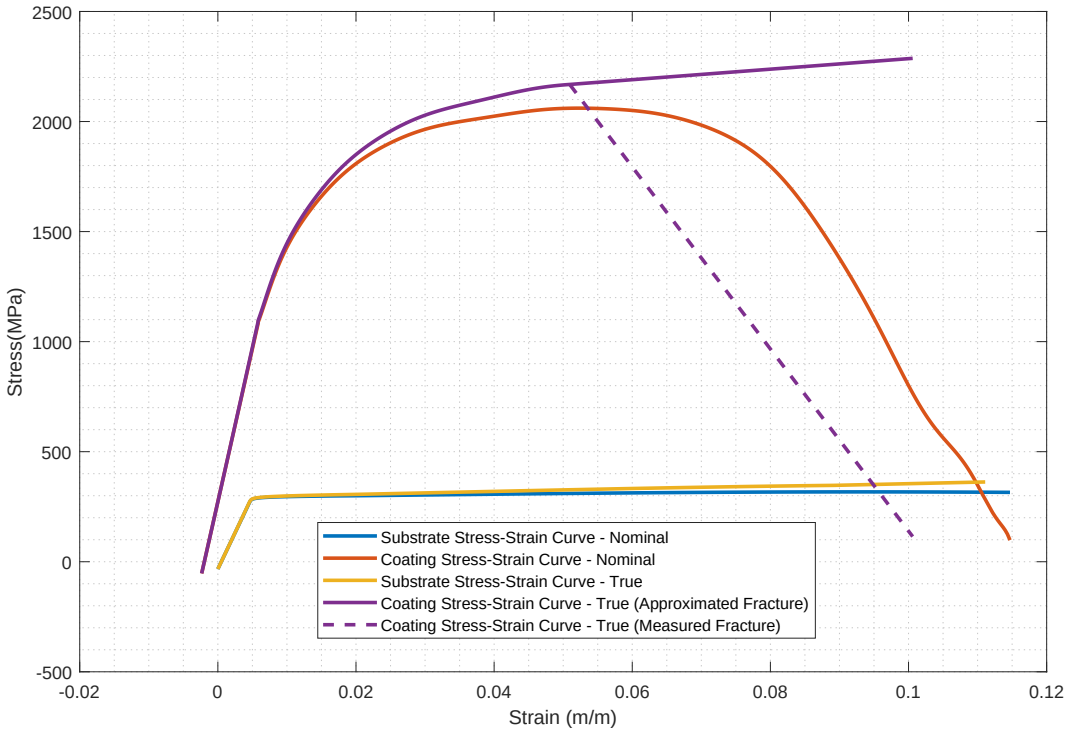

Figure 4.8 Nominal and true stress-strain curve for the nNiCo and Al 6061-T6 in a nNiCo coated specimen. Note the two lines in the nNiCo true stress-strain curve. The dashed line represents the straight line approximation from the necking stress to a stress calculated by dividing the calculated force in the nNiCo at fracture by the fracture area measured using SEM. This does not accurately represent any known metal behaviour. The solid line represents the approximated behaviour of nNiCo, following typical metal stress-strain behaviour. This curve was used to calculate the nNiCo monotonic SEDD. The origins of the different material curves are different due to the residual stresses, where the strain axis is the measured specimen strain.

The measured strength and modulus values for the nNiCo were higher than the values provided by the supplier. This difference may be due to variations in the measurement method, where the supplier values are likely measured using a bulk specimen rather than interpreting measurements from a coated specimen. Since strain energy density values for nNiCo are not present in literature, it is difficult to evaluate whether the obtained value is reasonable.

Only the properties for the cylindrical nNiCo-coated specimen were obtained. The flat specimen was not considered for material properties and fatigue testing due to uncertainties in the geometry. The coating thickness could not be reliably ascertained for the purposes of calculating residual stresses and therefore would not have provided reliable results. With the exception of one section in Chapter 5, the discussion regarding the coated specimens will refer to the cylindrical specimens.

4.3 Fatigue Results

The fatigue test results for the uncoated and nNiCo-coated Al 6061-T6 specimens are described in this section. For the aluminum specimens, the results are compared against data reported in the literature to assess the validity of the results.

4.3.1 Fatigue Life of Uncoated Al 6061-T6 Specimens

The uncoated Al 6061-T6 specimens were tested at several stress ratios. The maximum stress values, stress ratios (R-values) and the corresponding number of cycles to failure are described in Table 4.4. The results are plotted on an S-N curve in Figure 4.9. These results are superimposed on Al 6061-T6 literature data in the same figure to determine the similarity of the measurements to data found in the literature.

Table 4.4 Fatigue properties of the uncoated specimen set. The specimen ID and the corresponding maximum stress and stress ratio applied are listed, along with the recorded fatigue life of the specimen.

Specimen ID	Maximum stress (MPa)	Stress Ratio (R)	Fatigue Life (Cycles)
T11	291	-0.07	38683
T14	291	-0.07	69054
T19	275	0.01	81974
T12	291	0.01	56864
T16	291	0.01	41710
T17	291	0.01	60040
T3	295	0.01	65144
T5	310	0.01	15062
T9	310	0.05	20114
T18	286	0.10	151091
T20	291	0.10	101303
T4	303	0.10	41017

Resource constraints limited the number of tests that were completed, therefore fatigue tests at lower stresses, implying longer lives, were not performed. The data for $R = 0.01$ and

$R = 0.1$ were fit to a power-law relationship. The fit for $R = 0.1$ has a coefficient of variation (R-squared) value of 1, indicating a perfect curve fit, while the fit for $R = 0.1$ has an R-squared value of 0.766, indicating there was considerable scatter in the data. For fatigue, scatter is expected, even in laboratory conditions, due to the variability of the microstructure between specimens.

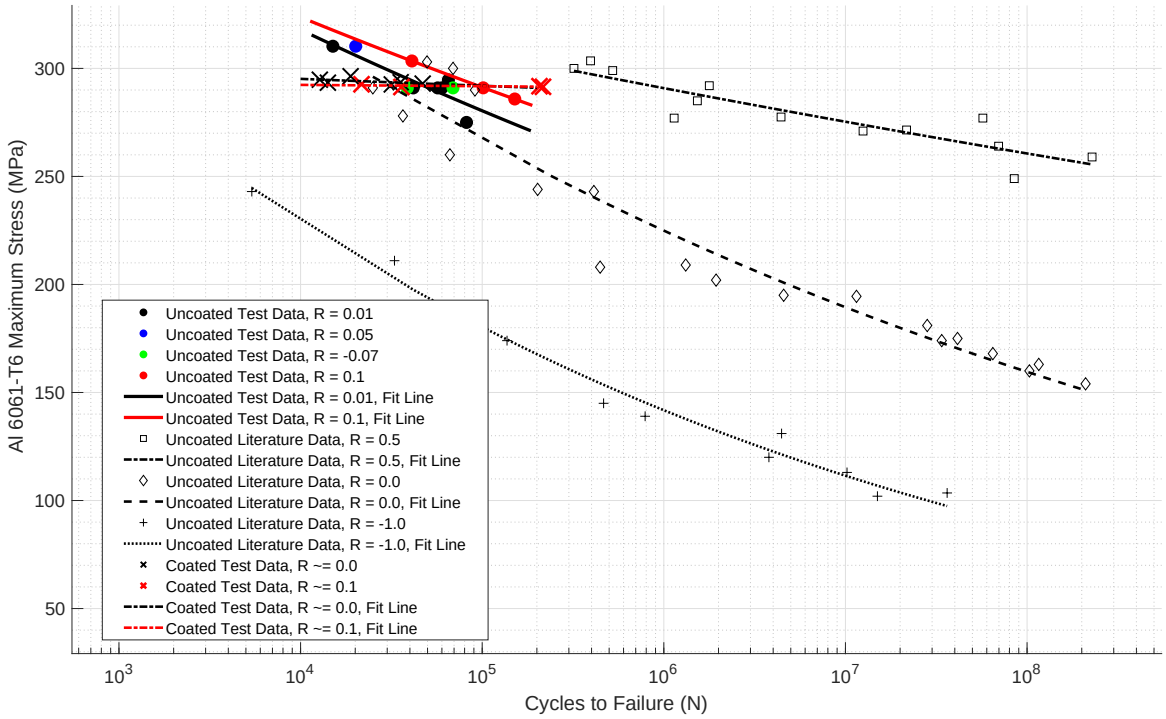

Figure 4.9 S-N curve for the uncoated and nNiCo-coated Al 6061-T6 specimens, where the stress axis is the maximum stress in Al 6061-T6. The uncoated fatigue life results are shown by the circles and the coated fatigue life results are shown by the crosses. The data is overlaid onto the literature data, indicated by the other shapes. This graph shows an increase in the fatigue life is strongly correlated with a decrease in stress applied for the uncoated specimens but an increase in the fatigue life does not result in a significant decrease in the stress level for the nanocoated specimens.

Exact comparisons to data found in the literature were not available since tests were not conducted at the same stress ratios. As discussed in Chapter 3, the nature of the grips did not allow for negative stress ratios, due to the backlash that would occur when the stress changes from tension to compression. The smallest stress ratio was $R = 0.01$ rather than R = 0.0 due to the possibility of negative loads (and therefore backlash) incurred on the specimen caused by machine variability during fatigue. Tests at $R = 0.5$ could be conducted, however these tests would require long tests times due to the high lifecycles at high stress ratios. Since the test facility could not be left unmonitored during these tests, testing at this stress ratio would take multiple days for the given test frequency.

An approximate comparison can still be made between the experimental dataset and the dataset from literature. Figure 4.9 shows an increase in stress ratio causes an increase in the number of cycles to failure at a given stress level and a decrease in the reduction of stress as fatigue life increases. This pattern fits with the experimental data. Based on these observations, the test data is consistent with the data in the literature. One observation to note from the literature data is the inherent scatter caused by small differences in specimen microstructure and surface finish, among other factors.

4.3.2 Fatigue Life of nNiCo-coated Al 6061-T6 Specimens

A set of Al 6061-T6 specimens coated with nNiCo, where the nominal thickness was 250 µm, were also cyclically loaded until fatigue failure. A summary of the results is shown in Table 4.5, where the load conditions and corresponding life of each tested specimen are listed.

Table 4.5 Fatigue properties of Al 6061-T6 specimens coated with 250-µm nNiCo. The maximum stress and stress ratios applied to the substrate and coating are listed with the corresponding specimen ID and fatigue life.

ID	Substrate Maximum Stress (MPa)	Coating Maximum Stress (MPa)	Substrate Stress Ratio	Coating Stress Ratio	Substrate Residual Stress (MPa)	Coating Residual Stress (MPa)	Fatigue Life (Cycles)
B1	293	901	0.02	0.31	24	-111	31779
B2	294	1064	0.02	0.35	33	-148	35565
B3	292	816	0.11	0.22	32	-145	206776
B7	295	1023	0.01	0.32	30	-147	12763
B11	296	1115	0.01	0.40	28	-130	18859
B13	291	959	0.07	0.23	22	-116	35907
B15	291	849	0.08	0.25	19	-85	216095
B16	293	875	0.03	0.33	31	-136	47016
B17	293	1009	0.10	0.33	23	-108	21650
B18	293	1353	0.02	0.43	-45	237	14140

The two objectives of the tests on coated specimens were to compare the performance of the coated specimens against the uncoated specimens and assess the validity of the life prediction framework for coated specimens. To compare the performance of the coated specimens against the uncoated specimens, the stress levels were selected so the aluminum substrate underwent similar conditions as the uncoated aluminum. Since the loads were

set based on the desired maximum stress and stress ratio in the aluminum, this meant the stress in the coating was dependent upon pre-existing fabrication conditions that could not be controlled. Residual stresses, which originated during the manufacturing process, were observed in the specimens. The tabulated stresses are modified to account for these residual stresses, according to the procedure described in Section 4.1.2. Since the residual stresses were not consistent across specimens, the maximum stress and the stress ratio applied to the coating varied between tests despite a consistent load in the substrate.

In Figure 4.9, the S-N plot for the coated Al 6061-T6 is also shown, where the stress axis shows the stress in the aluminum substrate. The data for coated specimens shows that there is a much larger variation in the number of cycles to failure for the coated specimens compared to the uncoated specimens for the same stress level. This large variation differs from expected metal behaviour, where there is a clear decrease in stress as the fatigue life increases. This variation indicates specimen fracture is likely driven by failure in the nNiCo coating layer rather than in the aluminum substrate. Since the nNiCo coating carries over 25% of the load, once the nNiCo fails, the aluminum is rapidly overloaded and fails as well. This phenomenon was confirmed by scanning electron microscope imaging of the fractured specimens, where crack initiation was seen in the nNiCo coating rather than the aluminum substrate, and the behaviour of the S-N curve when plotted for the coating. The S-N curve based on the nNiCo coating stresses is shown in Figure 4.10, where the stress axis represents the coating stresses. The relationship in this figure now resembles expected S-N behaviour in metals, where there is a much stronger inverse relationship between the stress level and the fatigue life. Since the stress ratios were not exactly the same between tests, the ratios are rounded to the nearest tenth for comparison of the data.

The collected nNiCo-coated aluminum data represents one of the first times in literature that the fatigue behaviour for an electrodeposited nanocrystalline metal coating has been quantified. As well, the presented data represents the first known instance where the coating and substrate behaviour of nanocrystalline coated specimens under fatigue are separately quantified. These contributions to literature should enhance the understanding of nanocrystalline coatings under fatigue loading.

4.4 Comparison of Fatigue Life Predictions Against Test Data

The fatigue test results were compared to the predictions obtained using the energy-based fatigue life prediction framework. This was done to evaluate the fatigue prediction accuracy.

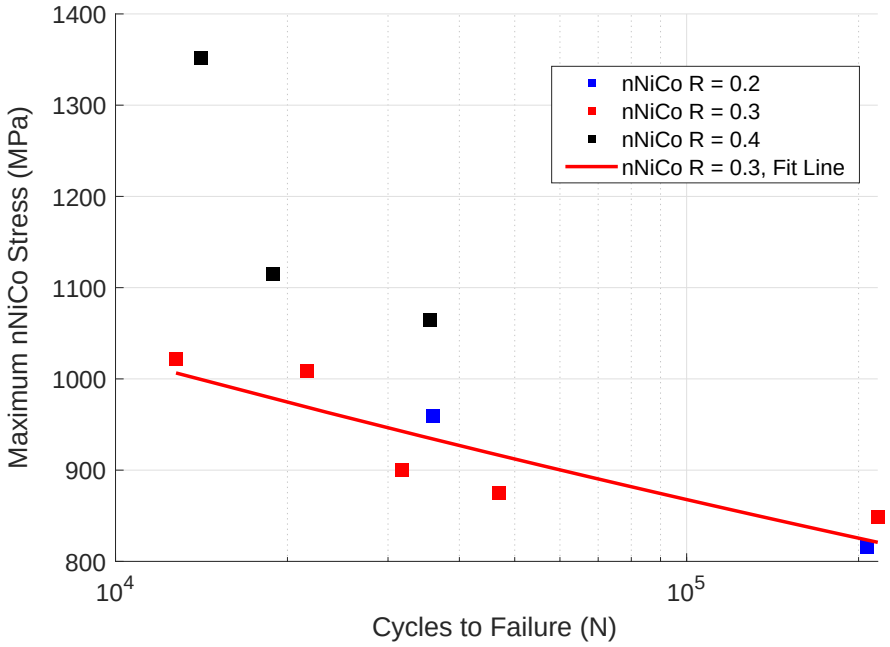

Figure 4.10 S-N curve for the nanocoated specimens, where the vertical axis is the maximum stress applied to the nNiCo coating. The approximate stress ratios at each point are indicated by the different colors.

The framework uses a set of curve fit parameters, known as FPP to predict the fatigue life of a specimen under known loading conditions. Two methods were used to obtain these FPP - the strain range method and the life method.

The comparison was performed for both the uncoated Al 6061-T6 specimens and the nNiCo coated Al 6061-T6 specimens, shown in Sections 4.4.1 and 4.4.2, respectively. For both sections, the life method and strain range method are used to obtain the FPP needed to be inserted into the energy framework. Section 4.4.3 analyses the effectiveness of the methods in obtaining FPP values for accurate predictions.

4.4.1 Fatigue Life Predictions for Al 6061-T6

This subsection compares the fatigue life predictions against the Al 6061-T6 fatigue results. The first part of this subsection compares the fatigue life predictions at the tested stress levels against the test results, as well as those from literature, where the predictions used FPP values obtained from the strain range method. These predictions did not match well against the collected data. The second part of this subsection compares the fatigue life predictions at the tested stress levels against the test results, where the predictions used FPP values obtained from the life method. The predictions from the second part matched

the test results better than those from the first part. The third part of this subsection compares data from literature against predictions made with the energy framework using FPP values obtained from the life method. The predictions were also shown to match the literature well.

Predictions using the strain range method

The strain range method obtains the FPP by minimizing the difference between the measured strain range and the corresponding calculated strain range. The strain range is calculated by inserting the FPP into the Ramberg-Osgood equation, as described in Equation 4.13. At each prediction point, the strain range values were the average strain range recorded recorded during the steady-state energy dissipation region. Using the average most accurately represented the strain range in fatigue. Strain range values from six different fatigue tests were used. The stress ratio for most of these tests was $R = 0.01$. For the other tests, the strain range could not be obtained because the strain gauges did not adhere to the specimen throughout the test. The FPP values obtained using the strain range method were $n = 0.846$ and $K = 2212$ GPa. Using these values, the average difference between the calculated and measured strains was 2.7%. The fatigue life prediction was calculated by inserting these FPP into Equation 4.10. The S-N curves showing the predictions at different stress levels and ratios are shown in Figure 4.11. The predicted S-N curves are overlaid against the experimental data.

The same FPP were used to predict the fatigue life at the stress levels from literature. A comparison between the predicted S-N curves and values from literature is shown in Figure 4.12. Note the fatigue life predictions at $R = 0.5$ using these values were all negative, since Equation 4.10 produces negative values when the mean stress is significantly greater than the stress amplitude and the parameter n is large. Therefore, the predictions at this stress ratio are not shown.

In general, the predicted S-N curves did not agree well with the data in all these cases. The differences between the predicted and calculated values are quantified in Table 4.6 at the end of this subsection, using the Armstrong symmetric mean absolute percentage error (SMAPE) and the Tofallis method [59]. Both of these methods are based on relative measures, thus avoiding bias towards selecting a prediction scheme which under-predicts the fatigue data. SMAPE is calculated by

$$SMAPE = \frac{1}{n} \sum_{i=1}^{N} \left[\frac{|g_i - f_i|}{(g_i + f_i)/2} \right], \tag{4.30}$$

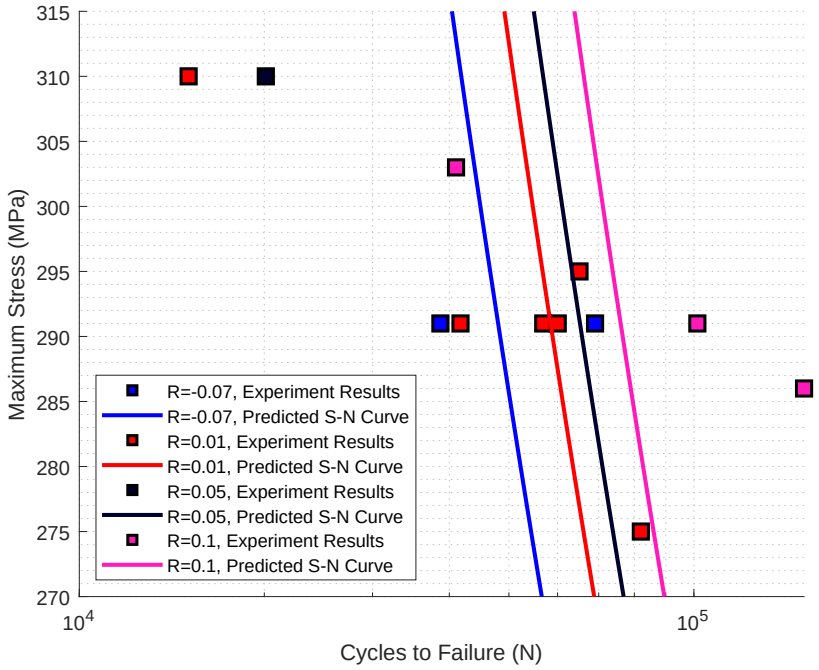

Figure 4.11 Predictions made using Equation 4.10 from the energy framework, using FPP values obtained from the strain range method, compared against the Al 6061-T6 test dataset.

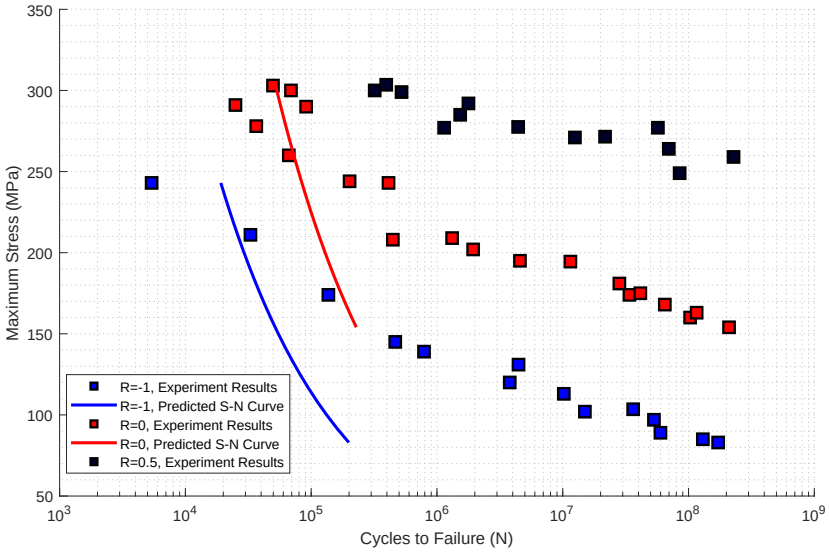

Figure 4.12 Predictions made using Equation 4.10 from the energy framework, using FPP values obtained from the strain range method, compared with the Al 6061-T6 dataset from literature. The predictions made for R = 0.5 were all negative and are not displayed.

where g_i is the predicted fatigue life and f_i is the observed fatigue life. The Tofallis function is calculated by

$$T = \sum_{i=1}^{N} \left(\ln \frac{g_i}{f_i} \right)^2, \tag{4.31}$$

where T is the value of the metric, g_i is the predicted fatigue life and f_i is the observed fatigue life. SMAPE provides information on the percentage difference between the observed and predicted fatigue life, whereas the Tofallis function provides information about the residual. For both functions, the desired value is zero, indicating perfect prediction to the observed values. However, due to the variability in fatigue scatter caused by conditions such as material microstructure, specimen surface quality and the laboratory environment, it is expected that scatter from the predicted value will occur. Note that the Tofallis function is a total relative residual value, which means that it cannot be used to compare prediction sets with a different number of observation points. The error values are shown for both the overall dataset and for the data at the considered stress ratio (used only for the life method).

Predictions using the life method

The life method was also used to obtain FPP for use in the prediction framework. This method uses Equation 4.10 to find the FPP which are able to calculate the closest predictions to the observed fatigue lifecycles. Figure 4.13 shows the predicted S-N curves against the test data. The predictions were expected to match the data closely because the life method uses the experimental data as an input. However, this was not the case. It was theorized that rather than using a set of FPP to predict the fatigue life for all stress ratios, there may be a unique set of FPP for each stress ratio. To examine whether unique FPP exist for each stress ratio, the life method was rerun considering only the data at a single stress ratio. Figures 4.14 and 4.15 show the predicted S-N curves against the experimental results, when the life method is run using only the data at stress ratios $R = 0.01$ and $R = 0.1$, respectively.

Although only the data at one stress ratio is used to calculate the FPP, the predicted S-N curves for the other stress ratios are shown in order to show the effect on other S-N curves when optimizing the prediction for one stress ratio. The figures show that better predictions are available when using the FPP at a single stress ratio to predict the fatigue life at that stress ratio, but the prediction accuracy at other stress ratios decreases. The FPP values that were used to calculate the predictions for each figure are listed in Table 4.6 at the end of this subsection. Since this thesis is based on using the strain range and loading conditions to obtain the energy dissipation and subsequent fatigue life of a specimen, the FPP values are re-inserted into the original strain range equation, Equation 4.13, and compared with

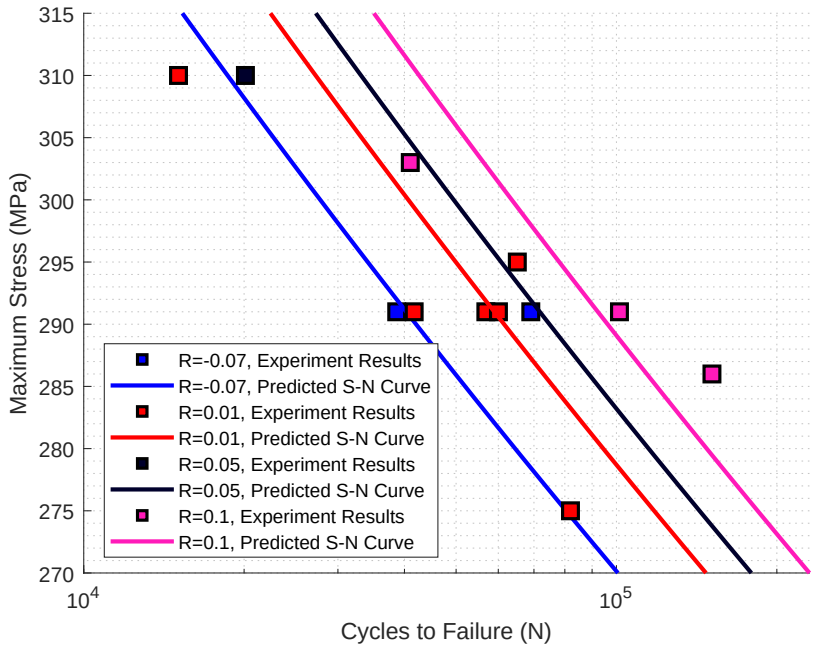

Figure 4.13 Fatigue life predictions compared to the Al 6061-T6 test dataset. The FPP values were obtained from the life method.

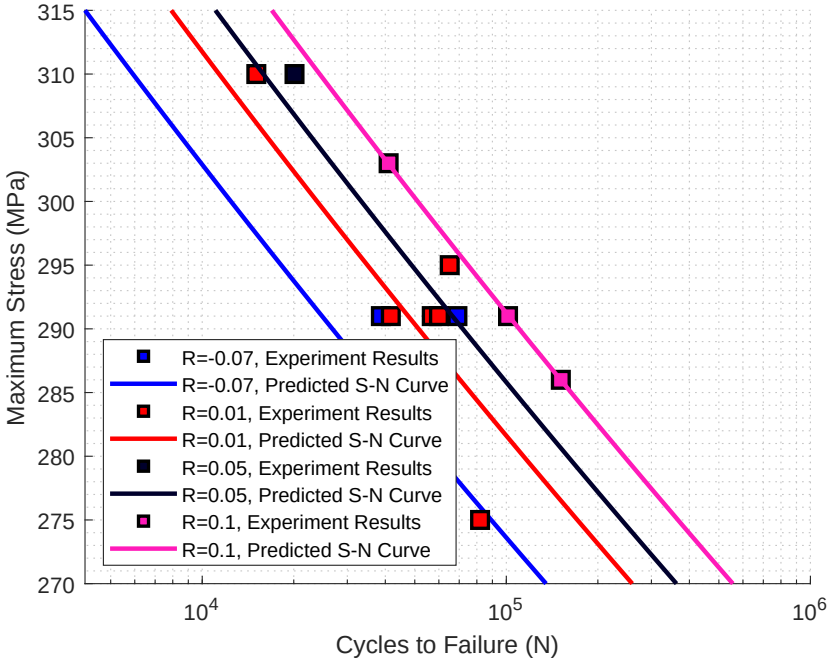

Figure 4.14 Fatigue life predictions compared to the Al 6061-T6 test dataset. The FPP values were obtained from the life method, by only considering the test data at $R = 0.01$.

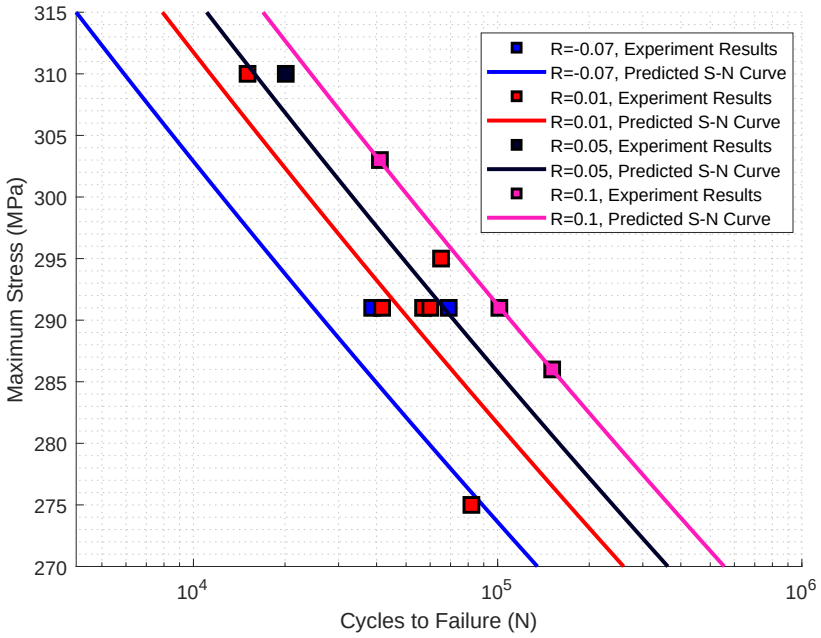

Figure 4.15 Fatigue life predictions compared to the Al 6061-T6 test dataset. The FPP values were obtained from the life method, by only considering the test data at $R = 0.1$.

the measured strain range. The differences are tabulated in Table 4.7 at the end of this subsection to determine whether using the strain range to calculate energy dissipation for predicting fatigue was a valid method.

Predictions using the life method for data from literature

Figure 4.16 shows the fatigue life predictions at the load levels from literature compared to the lifecycles listed in literature.

These predictions were made with FPP obtained using the life method, since the strain range for the results from literature was unknown. As with the test dataset, the predictions appear to be a compromise between several different tests. This was be due to different behaviour between the tests at stress ratios $R = -1.0$ and $R = 0.0$, versus the tests at $R = 0.5$. The S-N curves from literature show that for a given decrease in stress, fatigue life increases at a higher rate for the tests at $R = 0.5$ compared to the other tests. It is unclear why this occurs. The comparison between the data from literature and fatigue life predictions using FPP found when considering the data from only one stress ratio at a time are shown in Figures 4.17 to 4.19, for stress ratios $R = -1.0$, $R = 0.0$ and $R = 0.5$, respectively. As with the test dataset, the figures show that better predictions are available when using the FPP at a single stress ratio to predict the fatigue life at that stress ratio.

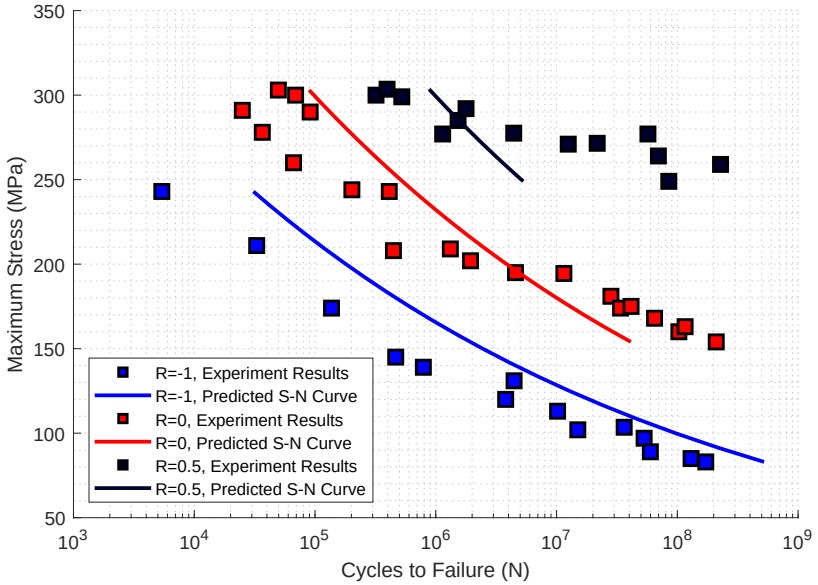

Figure 4.16 Predictions made using Equation 4.10 from the energy framework, using FPP values obtained from the life method, compared with the Al 6061-T6 dataset from literature.

The FPP values used in the fatigue framework to generate the predicted S-N curves in each figure are shown in Table 4.6.

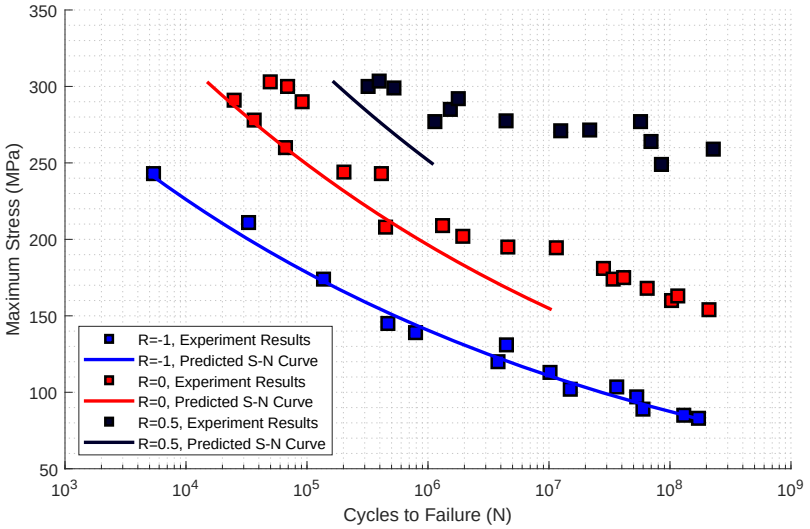

Figure 4.17 Predictions made using Equation 4.10 from the energy framework, using FPP values obtained from the life method, compared with the Al 6061-T6 dataset from literature. The FPP for this set of predictions was obtained by only considering the test data at $R = -1.0$.

As with the test dataset, strain range values were calculated using the FPP obtained from the life method for the data in literature. These are compared with the measured values in

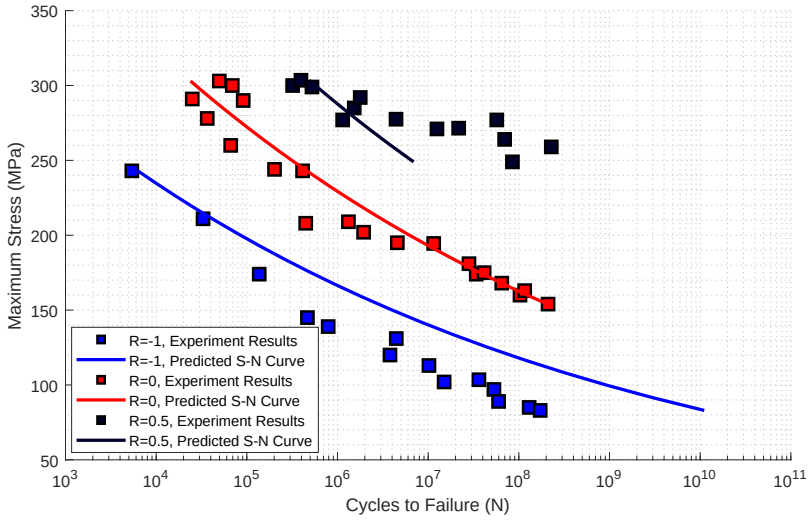

Figure 4.18 Predictions made using Equation 4.10 from the energy framework, using FPP values obtained from the life method, compared with the Al 6061-T6 dataset from literature. The FPP for this set of predictions was obtained by only considering the test data at $R = 0.0$.

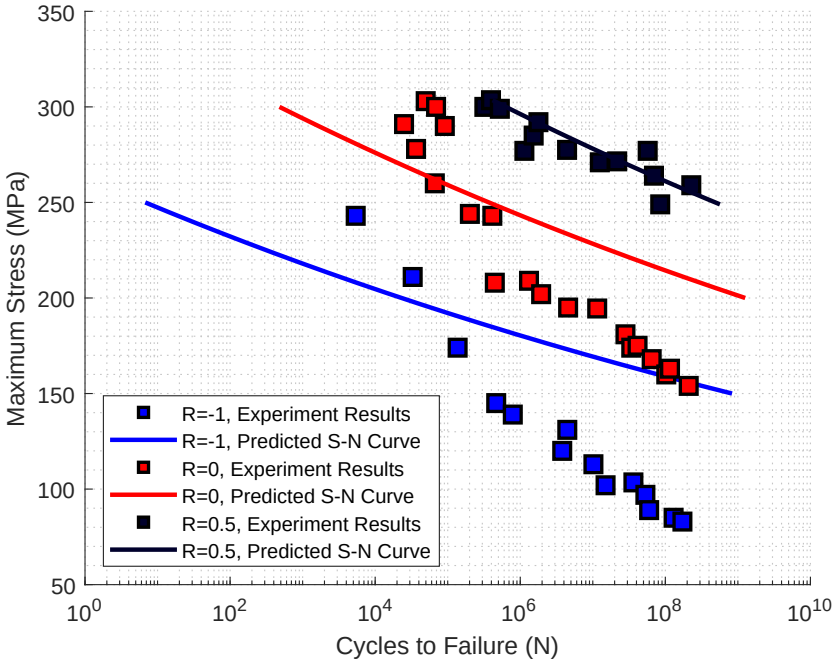

Figure 4.19 Predictions made using Equation 4.10 from the energy framework, using FPP values obtained from the life method, compared with the Al 6061-T6 dataset from literature. The FPP for this set of predictions was obtained by only considering the test data at $R = 0.5$.

Table 4.7. Only test specimens which had usable strain data are shown in the table. Since the different calculated strain values varied less than 1%, for simplicity only the average of the calculated strain values at different FPP for each load level are shown, along with the corresponding standard deviation for the different calculated strain values at a given test point.

Table 4.6 Al 6061-T6 FPP values obtained using the strain range method and the life method, calculated based on either the test data or data from literature. For each set of source data, the life method was obtained by considering the entire source dataset, and the source dataset at a single stress ratio. The SMAPE and Tofallis (ln(Q)) criteria are shown for the overall dataset and at the given stress ratio considered. Note that the ln(Q) criterion should only be compared between the same source datasets.

Source Data	FPP Method	Stress Ratio Considered	n	K (MPa)	SMAPE (%) Overall	SMAPE (%) Given Ratio	ln(Q) Overall	ln(Q) Given Ratio
Test	Strain	All	0.846	2212245	39.9	N/A	3.7	N/A
Test	Life	All	0.0892	1419	27.8	N/A	1.4	N/A
Test	Life	R = -0.07	0.0947	1557	39.4	28.8	2.9	0.2
Test	Life	R = 0.01	0.1325	2349	31.0	24.8	1.8	0.7
Test	Life	R = 0.1	0.0462	820	31.3	0.4	2.4	0.0
Lit	Life	All	0.1240	2386	103.1	N/A	110.4	N/A
Lit	Life	R = -1.0	0.1151	1740	98.2	31.4	208.4	2.17
Lit	Life	R = 0.0	0.0807	1247	96.5	51.8	188.5	11.5
Lit	Life	R = 0.5	0.0282	591	151.9	66.3	4090.6	14.7

Table 4.7 Calculated strain values using the FPP obtained from the life method, for the Al 6061-T6 specimens

Specimen ID	Maximum Stress	Stress Ratio	Measured Strain	Calculated Strain (Average)	Calculated Strain (Standard Deviation)	Difference (%)
T11	291	-0.07	3.92e-3	4.69e-3	1.7e-5	17.8
T19	275	0.01	4.12e-3	4.10e-3	1.2e-5	0.7
T12	291	0.01	4.63e-3	4.34e-3	6.5e-5	6.6
T16	291	0.01	4.27e-3	4.34e-3	6.5e-5	1.6
T17	291	0.01	4.04e-3	4.34e-3	6.5e-5	7.1
T18	286	0.1	3.92e-3	3.87e-3	1.4e-5	1.2
T20	291	0.1	3.98e-3	3.94e-3	9.3e-5	1.1

4.4.2 Fatigue Life Predictions for nNiCo-coated Al 6061-T6

This subsection shows a comparison between measured nNiCo-coated Al 6061-T6 fatigue life and the predicted fatigue life, calculated using Equation 4.10. The FPP are obtained

using the strain range and life methods, when considering only energy dissipation in the substrate and only energy dissipation in the coating. The monotonic SEDD value used for nNiCo in these calculations was 201 $\mathrm{MJ\,m^{-3}}$, which is an approximated value. The method of approximating this value is described in Section 4.2.

The results in this subsection are presented relating the cycles to failure to the coating stress, since fatigue life is believed to dependent on fracture in the coating. Presenting the results in this manner will allow for consistent comparison between specimens. However, the substrate still has some influence on the fatigue life. Therefore, rather than presenting the fatigue life predictions as an S-N curve as was done in Section 4.4.1, the fatigue life predictions in this subsection are presented at each test point to account for the effect of the substrate on the fatigue life.

The first part in this subsection shows a comparison between the test results and the fatigue life predictions calculated using FPP values obtained from the strain range method. As with the uncoated specimen results, using the FPP obtained using the strain method in the energy framework did not provide accurate predictions. The second part in this subsection shows a comparison between the test results and the fatigue life predictions calculated using FPP obtained from the life method. These results show a more accurate prediction compared to those calculated using the strain range FPP.

Predictions using the strain range method

Using the strain range method, the FPP were obtained for both the coating and the substrate. As with the uncoated aluminum specimens, not every test had a set of strain range values that were usable. For the coated specimens, only seven tests provided usable strain range values. The obtained FPP were inserted into Equation 4.10 to obtain fatigue life predictions. The test data are compared to the fatigue life predictions considering only substrate energy dissipation in Figure 4.20 and the fatigue life predictions when considering only coating energy dissipation in Figure 4.21. Both figures show that the fatigue life predictions do not match well against the test data.

The FPP values for the coating and substrate, along with the corresponding SMAPE and ln(Q) accuracy criterion, are listed in Table 4.8 at the end of this subsection. Note the large difference in K between the coating and the substrate. Given the FPP values found for the Al 6061-T6 case, the coating FPP is higher than expected. This may be caused by the sensitivity of the fitting equation, where small changes in strain cause large changes in the coating K value.

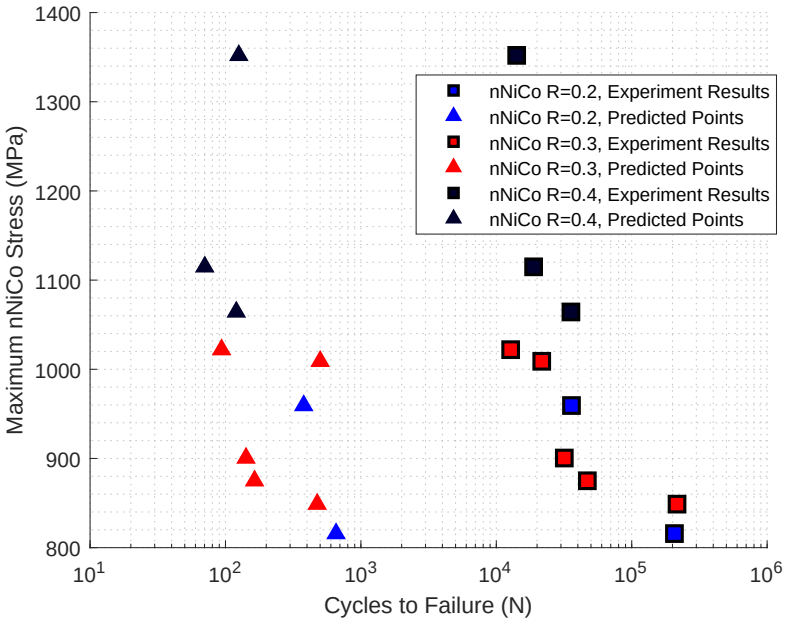

Figure 4.20 Predictions made using Equation 4.10 from the energy framework, using FPP values obtained from the strain range method, compared with the coated specimen dataset. The values used in Equation 4.10 refer to the substrate and not the coating. The stress axis indicates the maximum stress in the coating.

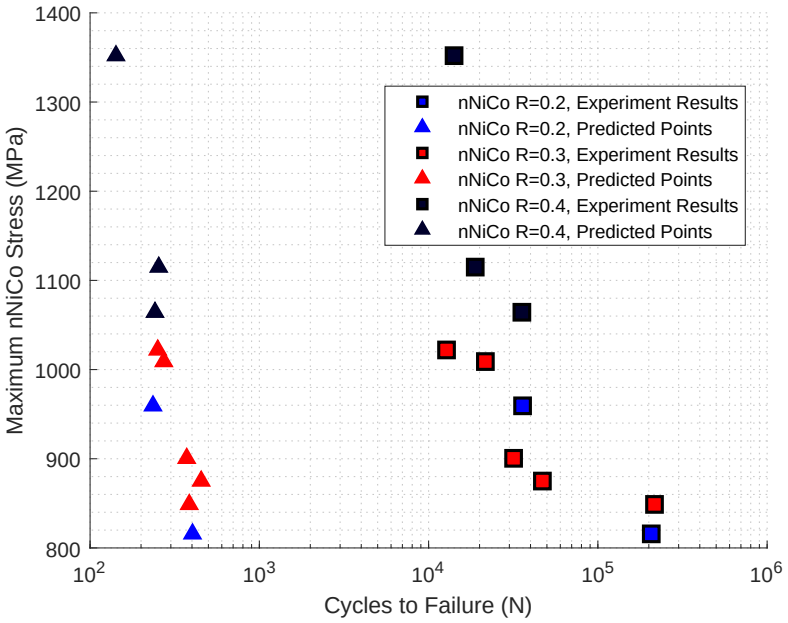

Figure 4.21 Predictions made using Equation 4.10 from the energy framework, using FPP values obtained from the strain range method, compared with the coated specimen dataset. The values used in Equation 4.10 refer to the coating and not the substrate. The stress axis indicates the maximum stress in the coating.

Predictions using the life method

The fatigue life was also predicted using FPP parameters obtained from the life method. The parameters were obtained by considering the energy dissipation from only the substrate or only the coating. Equation 4.10 is used to calculate the fatigue life predictions. The test data are compared against the predictions obtained using the life method FPP which considered only the substrate energy dissipation in Figure 4.22. The test data comparison against predictions, found using the FPP which considered only the coating energy dissipation, is shown in Figure 4.23. The corresponding FPP are listed in Table 4.8.

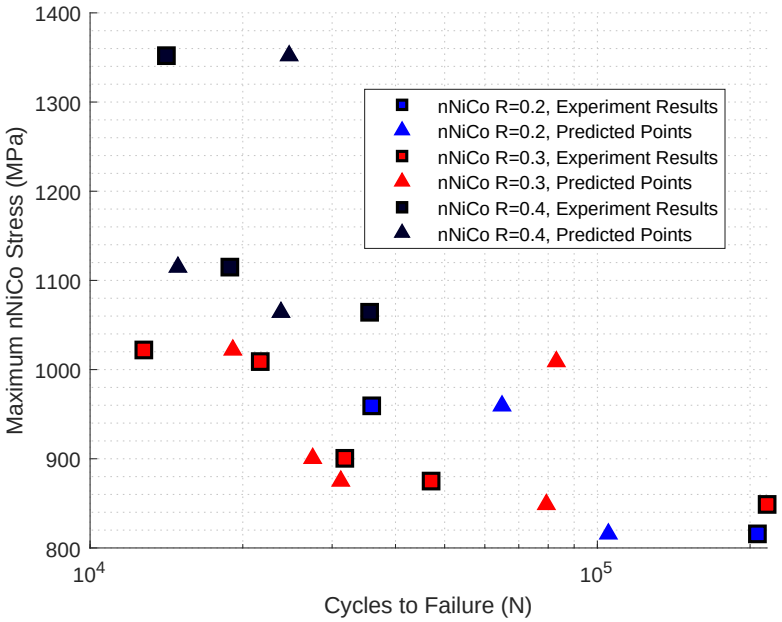

Figure 4.22 Fatigue test data compared to predictions. The FPP values used in the prediction were obtained from the life method when considering energy dissipation by only the substrate. The values used in Equation 4.10 refer to the substrate and not the coating. The stress axis indicates the maximum stress in the coating.

Table 4.8 also shows the prediction accuracy. The table shows the accuracy when considering the energy dissipation in only the coating is worse than those for the substrate energy dissipation, which implies that the substrate is the cause of failure. However, this increase in the substrate prediction accuracy is only seen when including all specimens. For the test point at 1350 MPa, a compressive residual stress in the substrate is observed, versus the other tests which had a tensile residual stress in the substrate. This likely affects the fatigue life, thus making this test point difficult to compare. If this point is ignored, the fatigue predictions in the coating have a SMAPE of 52.4% and the substrate SMAPE is 54.5%, making both predictions on a similar order of accuracy. This may indicate the coating causes the

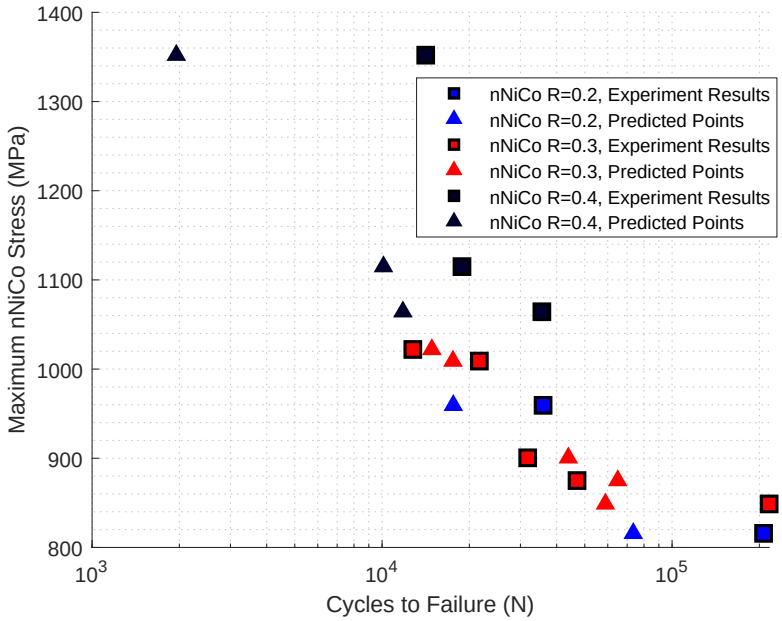

Figure 4.23 Fatigue test data compared to predictions. The FPP values used in the prediction were obtained from the life method when considering energy dissipation by only the substrate. The values used in Equation 4.10 refer to the substrate and not the coating. The stress axis indicates the maximum stress in the coating.

failure, but is not conclusive.

Table 4.8 Coated specimen FPP values obtained using the strain range method and the life method. The values are calculated by considering energy dissipation from only the Al substrate or nNiCo coating. The SMAPE and ln(Q) criteria are shown for the overall dataset.

Energy Source Considered	FPP Method	Al n	Al K (MPa)	nNiCo n	nNiCo K (MPa)	SMAPE (%)	ln(Q)
Al	Strain	0.023	532	N/A	N/A	196.6	283.1
nNiCo	Strain	N/A	N/A	0.392	23230	196.3	244.8
Al	Life	0.0265	628	N/A	N/A	54.5	4.5
nNiCo	Life	N/A	N/A	0.1225	6970	60.0	5.5

The FPP values were inserted into Equation 4.13 to determine whether the strain range values calculated were the same as the measured strain. The percentage difference between the measured strain and the calculated strain, using FPP values from Table 4.8, is shown in Table 4.9. This table lists the differences when the strain range is calculated using the FPP found by using the energy accounting for the Al substrate and nNiCo coating separately. As with before, only comparisons where valid strain range values were recorded during the stabilized fatigue region are shown.

Table 4.9 Calculated nNiCo-coated Al specimen strain values using the FPP obtained from the life method, considering only energy dissipated from the Al substrate and only energy dissipated from the nNiCo coating.

ID	Al σ_{mx} (MPa)	Al Stress Ratio	nNiCo σ_{mx} (MPa)	nNiCo Stress Ratio	Difference (%) (Al Energy Only)	Difference (%) (nNiCo Energy Only)
B1	293	0.02	901	0.31	3.3	16.9
B2	294	0.02	1064	0.35	1.6	9.3
B7	295	0.01	1023	0.32	20.7	30.2
B11	296	0.01	1115	0.40	1.0	12.6
B13	291	0.07	959	0.23	4.2	10.6
B15	291	0.08	849	0.25	0.2	4.8
B17	293	0.10	1009	0.33	0.2	8.5

4.4.3 Analysis of Energy-Based Fatigue Life Prediction Framework

The fatigue life had a SMAPE of up to 30% when the parameters obtained by the life method are used. Although this value may appear high, it does not take into account the scatter that occurs in fatigue data. Section 4.3 showed an R-squared correlation value of 0.7 between the data and a best fit line, indicating the data did not fit a best fit line well. Based on this scatter in the data, the SMAPE value appears to be reasonable. The predictions for the data from literature and the coating data were worse than those of the uncoated aluminum dataset. Both of these datasets demonstrate larger scatter than the aluminum dataset and this may contribute to the decrease in accuracy, as the accuracy measure assumes that the scatter is not present in the dataset.

Based on the aluminum results, it appears there is a unique set of FPP for each stress ratio, as opposed to a uniform set of FPP for a given material. The error in the prediction for the fatigue life of aluminum, at the best stress ratio results, was less than 1%. This high accuracy is attributed partially to minimal scatter in the fatigue data at this stress ratio. For all cases, the predictions improved when considering parameters for only one stress ratio. This phenomena exists for both the experimental data and the data from literature. Literature does not provide any conclusive guidance as to the validity of this conclusion. It is also notable that when predicting for different stress ratios using a given set of FPP, a similar increase in fatigue life when stress decreases is observed. This indicates that there is an underlying assumption in the method that a change in the stress ratio does not significantly affect the rate of increase in life when stress decreases.

Since the life method is based on calculating the energy dissipation from the strain

range, the obtained FPP were re-inserted into Equation 4.13, the strain range equation, and compared with the measured strains. The average difference between the calculated and measured strains was 5%. This value indicates that the original theory of using the strain range to predict the fatigue life by applying energy-based equations was valid but the FPP are highly sensitive to small changes in the strain range.

For the nNiCo-coated Al 6061-T6 specimens, the fatigue life predictions calculated using FPP from the life method matched well to the test data. Due to the limited data available, only an overall FPP value was found rather than finding it at each stress ratio. This has the effect of sacrificing some accuracy as the aluminum results noted there appears to be a different optimal FPP at each stress ratio. The fatigue predictions made using the FPP which considered only the coating had slightly higher accuracy, if only specimens with substrate tensile stresses were considered, indicating the earlier theory that coating drives the failure may be correct. However, the accuracy is not significantly more than the substrate to conclusive make this statement. The obtained FPP were inserted into Equation 4.13 and compared with the measured strains. The average difference between the calculated and measured strains was 4.4% when calculating via the substrate parameters and 13.3% when calculating from the coating parameters. This suggests that extending the method to include coated specimens is valid.

For both the uncoated aluminum and the nNiCo coated aluminum data sets, the strain range method produced FPP which did not predict the fatigue life well. This was likely due to the high sensitivity of the FPP to the measured strain range, where small changes in strain produced FPP which predicted vastly different fatigue life values. Evidence of this can be seen in Table 4.7, where the calculated strain using the FPP for predictions that matched well with the experimental results was very similar to strain range values calculated using the FPP found by the strain range method.

An assumption was made that the hysteresis loop is well-represented by the Ramberg-Osgood power-law relation. This assumption was confirmed in literature, but other relations representing the hysteresis loop should be considered. As well, the measured strain values could be obtained at a higher precision by better adhesion of the strain gauges. This would also reduce scatter in the experimental dataset. Typically strain gauges are attached to specimens by sanding part of the specimen surface to increase the surface roughness for adhesion, then attaching the specimen with an adhesive. Since sanding a specimen used for fatigue would generate early fatigue damage, the strain gauges were adhered directly onto the smooth aluminum surface without sanding. As a result, some of the strain gauges did not adhere well and provided inaccurate results. Given that this issue was prevalent for both datasets, the current experimental setup was not suitable for using the strain range

method as a candidate for predicting fatigue life. One future method to evaluate whether the method is usable would be to complete a large number of tests at just two different stress levels, which would likely produce a more representative value of the strain range during fatigue. As well, measuring the strain using contact extensometers rather than strain gauges would likely provide higher precision and more consistent strain measurements.

Within this chapter, the Shen-Akanda energy-based prediction framework using the strain range to measure the energy dissipation has been expanded to predict the fatigue life of specimens cyclically loaded at varying stress ratios and specimens which have a nanocrystalline coating applied. The predictions were compared with experimental test data. The predictions matched well with the experimental data when the FPP were found using the life method, and did not match well when using FPP found by the strain range method. Ideally, the strain range method should be used as the method is based on the strain range, but further improvements are needed to the strain range measurements prior to having this method be feasible.

The life and strain range methods are two new approaches to solving for the FPP when closed-form approaches are not available. These methods provide advantages over the Scott-Emuakpor method of obtaining the parameters by curve-fitting the hysteresis loops, since they are not reliant on the test frequency. In addition, the above presents one of the first times that nNiCo-coated Al 6061-T6 fatigue behaviour has been documented and increases the understanding of nanocrystalline coated fatigue. In addition, it was shown that for these specimens, the coating stress level may be the primary driver of failure rather than the substrate stress level as previously thought. Future work could expand on this thesis by performing tests beyond the current test range, into very high cycle failures and a larger variety of stress ratios. As well, work should be done to examine whether the assumption of Ramberg-Osgood hysteresis behaviour holds true for coated specimens. This is particularly important for the coated specimens to validate the understanding of fatigue of nanocrystalline coated specimens developed in this thesis.

Chapter 5

Evaluating Energy Dissipation Via Digital Image Correlation

Digital image correlation (DIC) is an alternative method to measure the strain fields needed to evaluate the strain energy density dissipation (SEDD). DIC offers similar measurement capabilities as strain gauges, but with several distinct advantages. In particular, the ability to measure full-field strains at high resolutions allows for comprehensive analysis of the SEDD during fatigue.

Both uncoated aluminum (Al) 6061-T6 and nanocrystalline nickel cobalt (nNiCo)-coated Al 6061-T6 flat dogbone specimens were used to compare the ability of DIC to measure parameters relevant to fatigue. However, only the Al 6061-T6 specimens were used for calculating the energy dissipation in Section 5.2, since the stresses for the nNiCo-coated Al 6061-T6 specimens were difficult to estimate. This difficulty was caused by large accumulations of the nNiCo at the edges during the electrodeposition process, making reliable estimation of the residual stresses difficult. Without the initial residual stress, the calculation of the actual stresses in the specimen was difficult and was not done.

5.1 Comparison Between Strain Gauge and DIC Strain Measurements

Strain measurements made using the strain gauges were compared to DIC to evaluate the feasibility of DIC as an alternative strain measurement system. Since the DIC images were obtained using a different system than the strain gauge system, the load was held at various points while pictures were taken to enable easy matching of the load information to the image data. An example of the time-stress relationship is shown in Figure 5.1, which demonstrates

the images being obtained when the load is temporarily held at pre-defined levels. These pre-defined levels were arbitrary and intended to obtain a sufficient number of DIC images for further analysis.

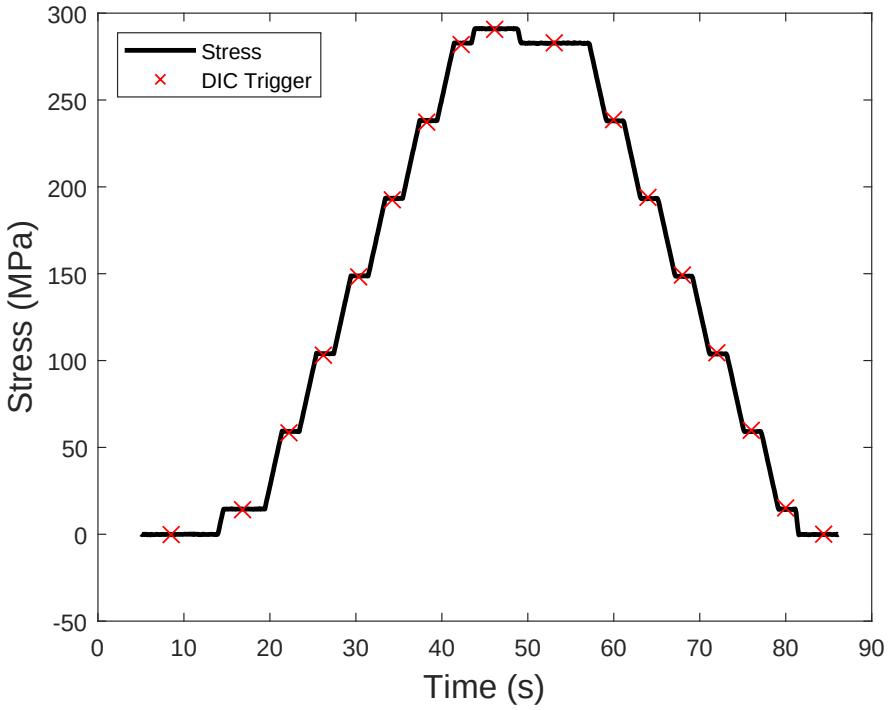

Figure 5.1 The time-stress relationship, where the x marks when DIC images were captured, while the black line marks the stress levels during the fatigue cycle.

To measure the strain for the DIC images, a virtual extensometer from Vic-2D was used. An example of the extensometer point selection is shown in Figure 5.2. In the figure, the two red dots indicate the extent of the extensometer, with the ϵ_{yy} strain field overlaid on top of the specimen. For the Al 6061-T6 specimens, four extensometer measurements at slightly offset positions were obtained and averaged to compare the performance of the strain gauge and DIC for measuring strain. Three extensometer measurements were used for the nNiCo-coated Al 6061-T6 specimens. Since the selection of the exact extensometer location is operator dependent, the different extensometer locations allow for quantification of the random error associated with different operator selections.

The Al 6061-T6 measurements were obtained from 44 different cycles throughout the fatigue life in the stabilized energy phase for a specimen tested with a maximum stress of 291 MPa and a stress ratio of 0.05. The stabilized energy region was referenced in Chapter 2 and is the fatigue phase where SEDD per cycle remains constant between cycles. The other Al 6061-T6 specimens tested did not have accurate strain gauge measurements due to poor

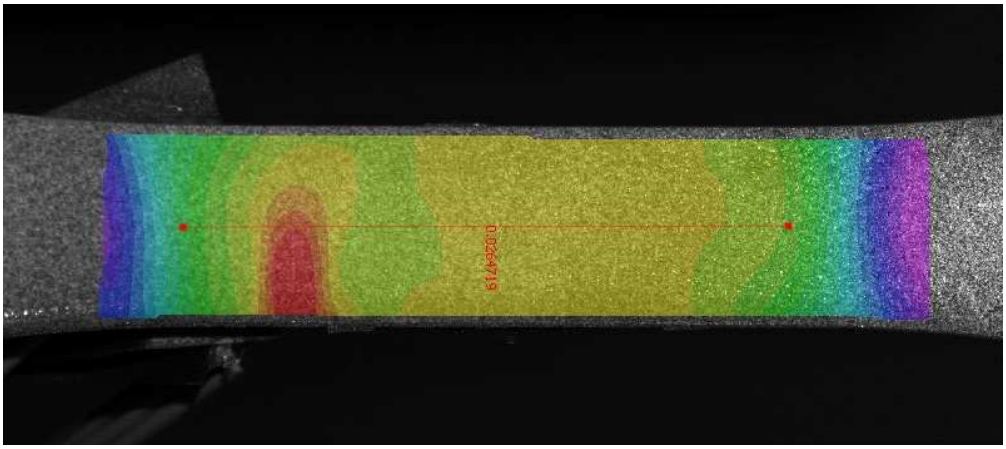

Figure 5.2 Example of a DIC extensometer, where the extensometer is indicated by a horizontal red line.

strain gauge adhesion and are not included in the comparison. The first nNiCo-coated Al 6061-T6 specimen comparison was obtained from five different cycles during fatigue and the second specimen used four different cycles. The low number of cycles recorded was due to the specimens fracturing earlier than expected during testing. The results are shown in Table 5.1. This table contains the average strain range values obtained for the two strain measurement types, along with the standard deviation and percent difference of these measurements. In addition, the pooled standard deviation value for the DIC measurements indicates the square root of the sum of variances of each cycle, such that

$$SD_p = \sqrt{\sum \sigma_i^2}, \tag{5.1}$$

where σ_i is the standard deviation of the different extensometer measurements for each cycle. This value is used to quantify the random operator selection variance mentioned above.

Table 5.1 Comparison of the strain range measurements made by the strain gauge and DIC for Al 6061-T6 and nNiCo-coated Al 6061-T6 specimens

Specimen Type	Al 6061-T6	nNiCo-coated Al 6061-T6 (Specimen 1)	nNiCo-coated Al 6061-T6 (Specimen 2)
Average - Strain Gauge	4.413e-3	4.933e-3	5.009e-3
Standard Deviation - Strain Gauge	3.356e-5	2.319e-5	1.814e-5
Average - DIC	4.879e-3	4.879e-3	4.998e-3
Standard Deviation - DIC	3.686e-5	1.751e-5	4.985e-5
Pooled Standard Deviation - DIC	2.851e-4	1.371e-4	5.954e-5
Average Percent Difference (%)	0.33	1.10	0.22

Table 5.1 shows that the difference between the two strain measurement methods is minimal, with at most a 1% difference between the two measurements. In addition, it indicates the average strain does not change significantly between cycles in the stabilized energy fatigue region, in line with literature. Finally, the low pooled standard deviation value indicates the different extensometers measured the strains similarly and special considerations for the extensometer locations are not required. These observations show DIC provides sufficiently accurate and consistent results for use as an alternative strain measurement system.

In addition to the strain measurements, the SEDD values were measured from the hysteresis loops by both methods and compared. Figure 5.3 shows a typical hysteresis loop for the Al 6061-T6 specimen, measured at 60% of the specimen fatigue life. Figure 5.4 shows a typical hysteresis loop for the nNiCo-coated Al 6061-T6 specimen, measured at 50% of the specimen fatigue life. Since comparison of the two strain measurement methods is the primary objective, the stress in this figure is simply obtained as the total force divided by total area of the specimen. Table 5.2 shows the average SEDD per cycle and provides statistical comparisons between the strain gauge and DIC measurements similar to what was done for Table 5.1.

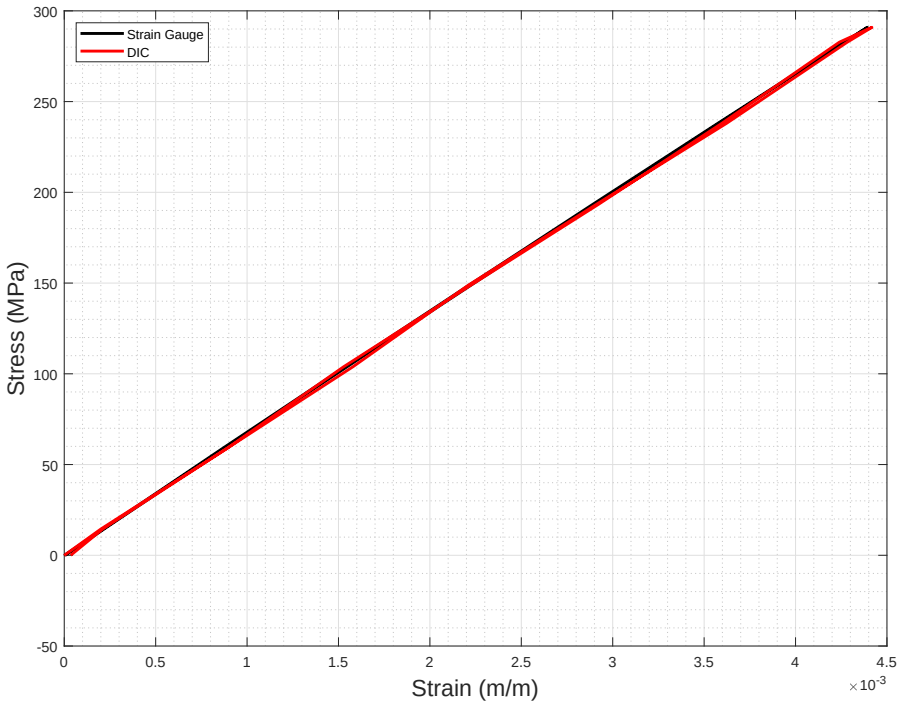

Figure 5.3 Hysteresis loop for an Al 6061-T6 specimen measured at 60% of the specimen fatigue life.

Figure 5.4 shows a larger SEDD for the nNiCo-coated Al 6061-T6 specimen compared

to the Al 6061-T6 specimen. The cyclic SEDD during fatigue for the Al 6061-T6 cylindrical specimens from Chapter 4 was not easily measured using the strain gauge due to the narrowness of the hysteresis loop used to measure SEDD. For the dogbone specimens, this pattern continued, as evidenced by the large standard deviation in Table 5.2 for the strain gauge. The DIC measurements for the Al 6061-T6 specimens showed slightly lower standard deviation indicating a more consistent measurement throughout fatigue, however the large pooled standard deviation value indicates there was a large variation between the virtual extensometer measurements. For the nNiCo-coated Al 6061-T6 specimens, the standard deviation of the measurements relative to the mean was much lower, indicating more consistent measurements for both the strain gauge and DIC. The large deviation found for specimen 2 is likely caused by a virtual extensometer which overlapped a strain concentration. The average percent difference in measuring the SEDD is approximately 15% for both the Al 6061-T6 and nNiCo-coated Al 6061-T6 specimens. Based on the variations in the measurements, the SEDD is unlikely to be accurately obtained for Al 6061-T6 specimens, while promising results are shown for obtaining SEDD for nNiCo-coated Al 6061-T6 specimens. However, the percentage difference between the measurement results indicate DIC may not provide adequate accuracy to replace strain gauge measurements. This difference is likely caused by noise in the measurements, which affects the SEDD measurements significantly more than the strain measurements due to the precision required in these measurements.

Table 5.2 Average SEDD measured by the strain gauge and DIC methods

Specimen Type	Al 6061-T6	nNiCo-coated Al 6061-T6 (Specimen 1)	nNiCo-coated Al 6061-T6 (Specimen 2)
Average - Strain Gauge ($\mathrm{J\,m^{-3}}$)	3288	26923	37214
Standard Deviation - Strain Gauge ($\mathrm{J\,m^{-3}}$)	2832	6907	8280
Average - DIC ($\mathrm{J\,m^{-3}}$)	3795	23019	55746
Standard Deviation - DIC ($\mathrm{J\,m^{-3}}$)	2402	7664	35317
Pooled Standard Deviation - DIC ($\mathrm{J\,m^{-3}}$)	15703	7027	57462
Average Percent Difference (%)	14.33	15.63	39.87

5.2 Measuring Strain Energy Density Dissipation Via DIC

Scott-Emuakpor et al. [20] note the SEDD per cycle remains constant throughout the majority of a specimen lifetime. Impending fracture is indicated by a significant rise in

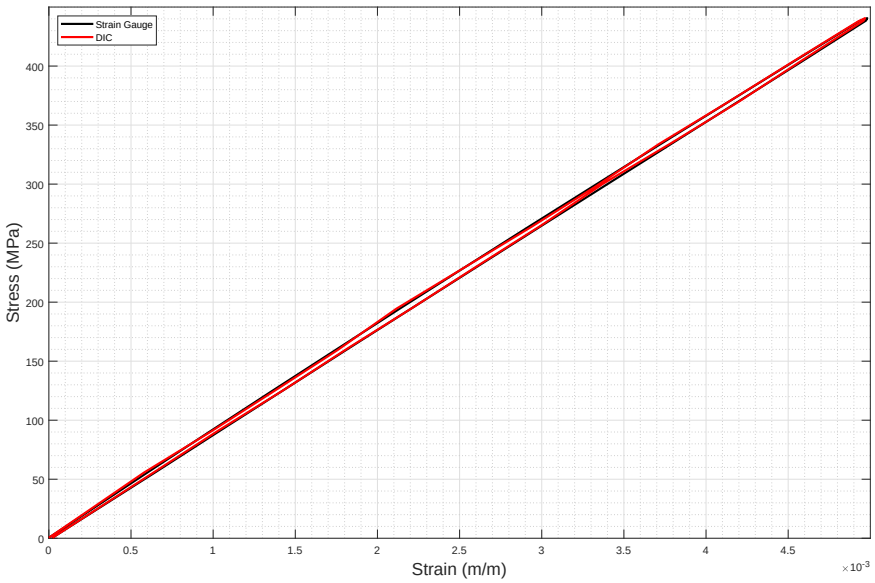

Figure 5.4 Hysteresis loop for a nNiCo-coated Al 6061-T6 specimen (specimen 2 in Table 5.2) measured at 50% of the specimen fatigue life. The vertical axis combines the stresses for the coating and substrate into a total stress value, calculated by the total force divided by total cross-sectional area.

the SEDD. An example of this rise in SEDD was shown earlier in Figure 2.3, where the strain energy dissipation rises at around 90% of the specimen lifetime. Chapter 2 noted that Letcher [7] defined a critical life value based on this observed deviation of the steady-state SEDD value. In this section, a method to obtain the critical life value based on the SEDD calculated from DIC is shown, along with the corresponding results of this method.

5.2.1 Methodology

The DIC images were obtained using the procedures described in Section 3.2. Section 5.1 noted that strain gauge measurements were not obtained for each specimen. Since the strain gauge measurements were affirmed to be similar, using only the DIC measurements is sufficient. As well, only the Al 6061-T6 specimens are analyzed due to difficulties in accurately determining the stresses in the nNiCo-coated Al 6061-T6 specimens, as described in Section 5.1.

Obtaining the SEDD requires both stress and strain measurements. DIC allows for full-field strain measurements to be easily obtained based on correlating the deformed grayscale pattern to the original grayscale pattern on the specimen, but full-field stress measurements are difficult to obtain. To obtain precise full-field stress estimates, several proposals have

been put forward for combining finite element formulations with DIC techniques. Réthoré et al. [60] show that these properties can be easily obtained when the specimen is under linear elastic isotropic conditions, but these methods pose difficulties when plasticity is introduced, as explicit constitutive relations for the material are not easily obtained in these cases. Additionally, stresses during fatigue are particularly difficult to determine due to the complexities of stress near the crack tip when a crack forms, requiring comprehensive knowledge of the loading history. Although Chapter 2 describes methods to quantify the crack stress fields using the J-integral, a comprehensive methodology to convert the measured strains obtained from DIC into accurate stresses is currently unavailable in literature.

Rather than attempting to quantify the full-field stresses to obtain the SEDD, an approximate estimate of the SEDD during fatigue cycling was obtained by,

$$SEDD = \sigma_y \epsilon_r, \tag{5.2}$$

where σ_y is the nominal maximum stress applied and ϵ_r is the full-field residual strain field in the load axis obtained at the end of the cycle (stress equal to zero). This assumes that the large majority of the inelastic strain occurs when the stress is at or near the maximum, the applied full-field load is only in the load axis and the minimum load is negligible. Using this equation produces an approximate full-field SEDD measurement at various points throughout fatigue cycling.

5.2.2 Results

Six fatigue tests on flat dogbone Al 6061-T6 specimens were completed. The applied load on five of these tests was 310 MPa with a stress ratio of 0.05. The remaining test was completed at the same stress ratio, but with a maximum load of 291 MPa to assess the effects when the maximum load changes. Table 5.3 shows the fatigue life of each specimen. For the tests at 310 MPa, the average fatigue life was 24032 cycles, with a standard deviation of 3377 cycles.

Table 5.3 Fatigue Life of Dogbone Specimens

ID	Maximum stress (MPa)	Stress Ratio (R)	Fatigue Life
P18	291	0.05	68800
P3	310	0.05	21934
P4	310	0.05	27020
P6	310	0.05	25878
P13	310	0.05	19120
P17	310	0.05	26210

The DIC images were obtained at varying points during the specimen lifetime, in an attempt to get the optimal balance between test efficiency and obtaining an adequate amount of images for analysis. As a result, some fatigue tests had residual strains imaged in the cycle immediately prior to failure and some tests did not have residual strains imaged within 500 cycles to failure. However, at a minimum, images were obtained during the initial cycles and within 1000 cycles prior to failure. For all the specimens except for P13, the full gauge section area, 557 mm^2, was imaged. For P13, a magnified gauge section was imaged in an attempt to obtain higher resolution strain data near the crack tip. However, the results did not significantly increase the resolution of the data.

An example of the evolution of the SEDD during fatigue is shown in Figure 5.5 for specimen P13. In this image, the total SEDD values are shown when the stress is at zero MPa after the first cycle, cycles 14612, 17616 and 18618, and the cycle right before specimen fracture. The specimen fractured at 19120 cycles. It was observed that there was a region where the SEDD increased prior to fracture.

To quantify the results, the median SEDD value of the gauge section was computed, then compared to the maximum full-field SEDD value in the gauge section. Figure 5.6 shows the plots of the median and maximum SEDD values versus the percentage of cycles to failure for all the tests conducted. Figure 5.7 shows the same plot for the test at 291 MPa and the averaged values from Figure 5.6 for the tests at 310 MPa. Table 5.4 shows the average median value throughout the fatigue life and the average maximum value between 20-70% of the fatigue life.

Table 5.4 Median and Maximum SEDD Values

ID	Average Median SEDD ($MJ\,m^{-3}$)	Average Maximum SEDD (20-70% Life) ($MJ\,m^{-3}$)
P18	0.65	0.81
P3	2.84	3.24
P4	4.39	4.79
P6	3.52	3.92
P13	6.41	6.71
P17	6.77	7.03

Figures 5.6 and 5.7 show the difference between the maximum and median values is less than 0.5 $MJ\,m^{-3}$ until the specimen approaches the fracture cycle. The critical fatigue point is when the maximum exceeds the average median by 0.5 $MJ\,m^{-3}$ and is marked on Figure 5.6 by filled circles. On average, this point occurs at 91.7% of the fatigue life cycle, with a standard deviation of 7.5%. The point at which this occurs for each specimen is detailed in Table 5.5.

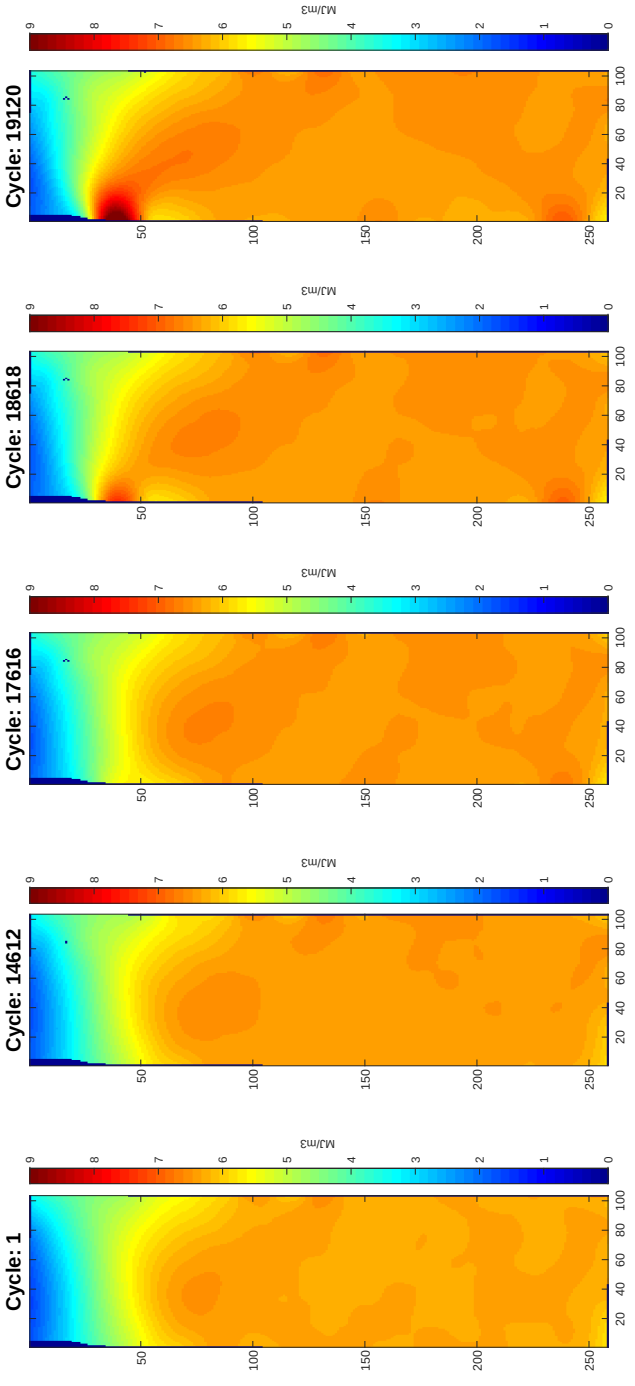

Figure 5.5 SEDD fields at various points during fatigue cycling, showing the evolution of the SEDD field.

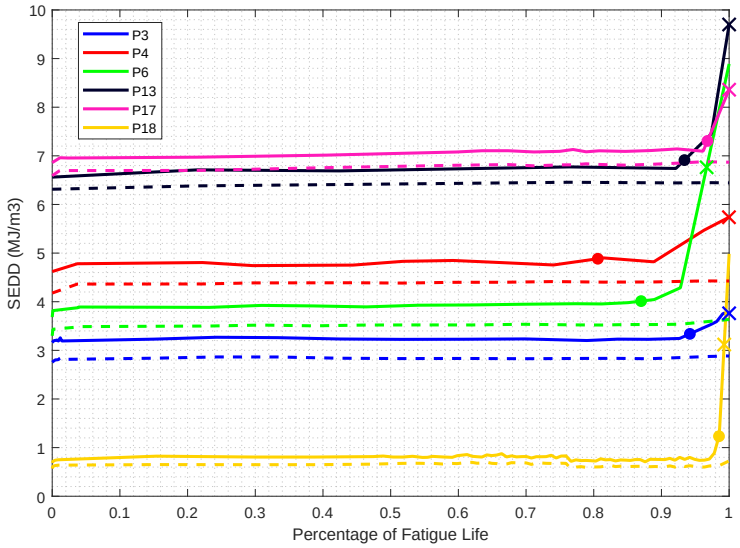

Figure 5.6 Median and maximum SEDD values obtained at various points throughout the fatigue cycles for the tests. The dashed lines represent the median values during fatigue and the solid lines represent the maximum values. The x marks indicate the last point measured by DIC for each specimen, where the remainder of the points are linearly extrapolated. The filled circles indicate the point where the specimen exceeds the critical fatigue criteria. All tests were conducted at a maximum stress of 310 MPa and a stress ratio of 0.05, with the exception of P18 which was conducted at 291 MPa.

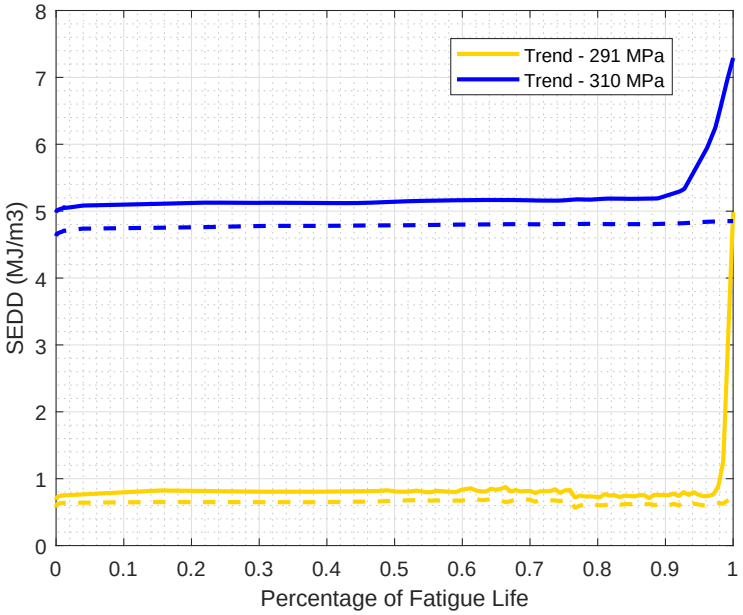

Figure 5.7 Median and maximum SEDD values obtained at various points throughout the fatigue cycles for the test at 291 MPa versus the average values for the tests at 310 MPa.

The region where the specimen fracture occurs is in the same position as where the full-field SEDD values are observed to exceed the critical fatigue criteria. Although resolution is insufficient to visualize the crack formation, it can be reasonably assumed from literature that the critical SEDD region is centered on the crack origin. Figures 5.8 and 5.9 show two examples of the fractured specimens on the left and the vertical strain map captured in the cycles immediately prior to fracture on the right. The region where the strain increase occurs approximately matches the location of the fracture for the top half of the specimen. It does not match the bottom half because the bottom grip drops when the specimen fractures. All specimens demonstrated this phenomena of the fracture location approximating the location of strain concentration. Since the SEDD values are a factor of the strain values, the strain map is sufficient to demonstrate this phenomena. This phenomena matches the theoretical energy dissipation caused by the large increase in plasticity and crack formation at the fracture location.

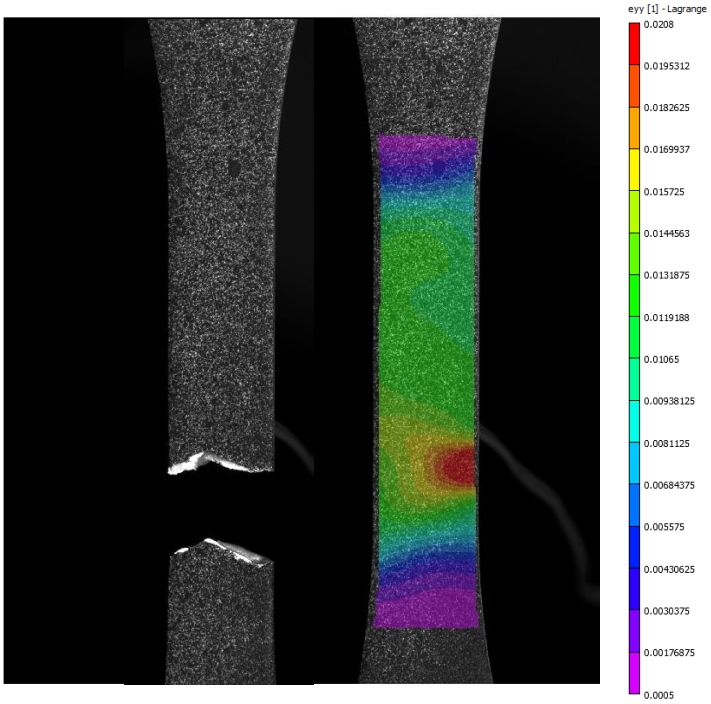

Figure 5.8 The fractured specimen P6 and the corresponding strain map immediately prior to fracture.

Analysis was performed to determine whether there was a critical size of the zone where the SEDD exceeds the criteria. For consistency, the region was taken when the fatigue life was approximately 98%. Since the images were not taken at exactly the same percentage of fatigue life, it is difficult to compare the size of this critical zone precisely. It was not practical to obtain the DIC images to calculate SEDD after each cycle, but future tests should examine

what the optimal measurement frequency is. Based on the preliminary results in Table 5.5, the zone size does not appear to be consistent, with drastically varying sizes from 1 to 140 mm^2. Note that Table 5.5 does not list the size for specimen P17. For this specimen, the only DIC images obtained with a critical zone present were taken right before fracture, which make it inconsistent with the zone size measurements taken for the other specimens at 98% of the fatigue life.

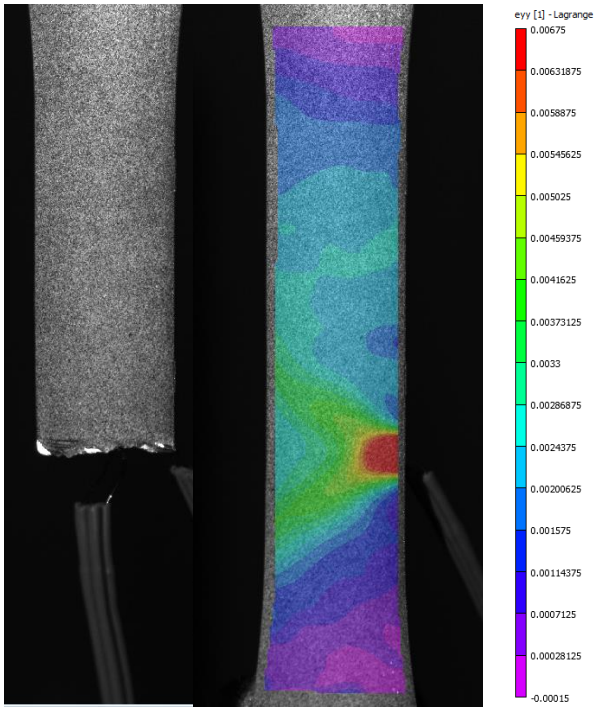

Figure 5.9 The fractured specimen P18 and the corresponding strain map immediately prior to fracture.

Based on the results described above, comparisons to existing literature can be made. The pattern of full-field SEDD generally follows the trend observed in literature. Quantification of a critical point prior to fatigue fracture is consistent with Letcher's theory of a critical point prior to fatigue fracture [7]. By using the full-field SEDD results, the large increase in SEDD shortly before fatigue fracture can be attributed mainly to a small highly strained region rather than an overall increase in SEDD throughout the specimen. Although the size of the region varies significantly, the region is shown to be at least 1 mm^2 large, making it detectable at the macroscopic level.

The demonstration of a critical point allows for the development of new fatigue detection methodologies. Rather than searching for cracks within a specimen, a speckle pattern can be painted on a specimen that has a known maximum stress level. Then, the residual strains can be monitored during fatigue and the part taken out of service when a 1 mm^2 region is

Table 5.5 Critical Point and Critical Region Measurements

ID	Critical Point (% Life)	Critical SEDD Region Size When Fatigue Life = 98% (mm^2)	Actual Life When Region is Measured (%)
P18	98.4	1.76	98.5
P3	94.2	11.02	98.2
P4	80.5	21.24	96.2
P6	87.0	141.75	96.7
P13	93.4	1.253	97.3
P17	96.7	N/A	N/A

detected which has SEDD values that are 0.5 $MJ\,m^{-3}$ greater than the median SEDD value.

Chapter 6

Conclusions

The existing energy-based fatigue prediction method was expanded to include predictions for nanocrystalline-coated specimens loaded at varying stress ratios. This work also represented one of the first times in literature that the fatigue properties of these specimens has been characterized. In addition, digital image correlation (DIC) data was used to demonstrate there is a region where the strain energy density deviates by a critical value immediately prior to fatigue fracture.

6.1 Extension of the Energy-Based Fatigue Prediction Method

The existing strain range method described by Shen and Akanda [23] was shown to reduce the dependence of the strain energy density prediction on the fatigue frequency. This method was expanded in this thesis to incorporate fatigue cycling with non-zero mean stresses. This was validated by comparing the test data for cylindrical Al 6061-T6 specimens against the predictions calculated using the framework. Two fatigue prediction parameters (FPP) were used in this calculation and were based on the strain range measured during fatigue, but could also be obtained by curve-fitting the experimental S-N dataset. The strain range method and the life method were the two methods used to obtain these parameters. Using the FPP obtained from the life method to predict the fatigue life provided predictions that matched well to the test data. However, the predictions did not match well when using the FPP obtained from the strain range method to calculate the fatigue life. This poor prediction was likely due to the sensitivity of the FPP to small variations in the strain. When the FPP obtained using the life method were inserted into the original strain range equation, the values were mostly within 10% of the measured strain. The calculated fatigue

predictions were also compared to data from literature. It was shown that the predictions improve when a unique set of FPP are used for each stress ratio, contrary to the original hypothesis of a single set of FPP that are insensitive to stress ratio variations.

The model was then expanded to incorporate fatigue life predictions for coated specimens. For this study, nanocrystalline nickel cobalt (nNiCo) was used as the coating and Al 6061-T6 was used as the substrate. Methods were developed to estimate the nNiCo properties from the overall coated specimen, by assuming the underlying aluminum substrate behaviour was known. In addition, a novel technique was developed to estimate the specimen residual stresses by shifting the known aluminum stress-strain curve along the strain axis until the curvature was minimized for the nNiCo stress-strain curve. As with the aluminum dataset, the FPP were obtained using the strain range and life methods. Again, the parameters calculated by the life method produced predictions that matched well with the test data and the parameters calculated by the strain range method did not produce predictions that matched well. In addition, it was observed that the predictions were best when only analysing the energy dissipated by the coating, rather than analysing the energy dissipated by both the coating and substrate.

Based on the comparison between the fatigue life predictions and actual fatigue test data, the expanded fatigue prediction framework provides a basis for predicting cycles to failure if the FPP are accurately estimated. This method can be applied to both coated and uncoated specimens.

6.2 Strain Energy Dissipation Via Digital Image Correlation

DIC images were captured to evaluate the cumulative full-field strain energy density dissipation behaviour during fatigue. Observations showed that a large amount of energy was dissipated at the beginning of fatigue cycling, but very little dissipation occurred afterwards. The changes in both the median and maximum values of the full-field strain energy density dissipation during fatigue were recorded. It was observed that these values significantly deviated when the number of cycles to fracture was approached. The region where this deviation occurred had a consistent minimum size. This led to the creation of a new fatigue criterion, which states that at 98% of the cycles to failure, there will be a critical region of at least 1 mm^2, where the cumulative strain energy density dissipation in that region will deviate from the median cumulative strain energy density dissipation of the specimen by 0.5 $MJ\,m^{-3}$. This fatigue criterion creates a way forward for the development of a non-destructive inspec-

tion method for impending fatigue fracture, where if the applied load is known and constant, the elapsed number of cycles are known and DIC images at zero load are obtained, then a determination can be made for whether the part should still be in service based on the existence and size of a region where the strain energy density exceeds the median value.

In addition to the fatigue criteria above, observations were also made to compare the strain measurements obtained by DIC against strain gauge measurements. The results showed DIC provided equally consistent and accurate results when measuring strain for obtaining the strain range, but the measurements were not sufficiently accurate to use for calculating the hysteresis loop to obtain strain energy density dissipation (SEDD).

6.3 Future Work

There are a number of further investigations that could be undertaken to improve on the thesis conclusions. For the expansion of the energy-based fatigue prediction framework, improvements to the strain range method are required, as the predictions showed only good matches with the data when using the parameters obtained from the life method. Using an alternate measurement system such as an extensometer may provide the matches needed. In addition, the range of tests was limited in scope, making comparison to data from literature necessary. Additional tests at negative stress ratios, as well as tests at lower maximum stresses, are necessary to fully validate the framework. These tests could be performed for both the coated and uncoated specimens.

The coated prediction equations could also be improved. Due to the poor predictions made when using the strain range FPP, it was not possible to obtain good estimates of the separated energy dissipation and find an accurate determination of whether the coating or substrate energy should be considered. Future work should obtain more accurate strain range data to verify this work. As well, the coated specimen behaviour is assumed to be driven by fatigue in the nNiCo coating. Additional coated specimen tests would provide further verification for this test. As well, a bulk nNiCo static test would allow for precise quantification of the static strain energy density dissipation, since the fracture behaviour of nNiCo is unclear. Furthermore, analysis should be performed to examine whether the Ramberg-Osgood model is an adequate representation of the hysteresis loop.

The new fatigue indicator using DIC could be improved by a better stress estimate. Currently, the full-field stresses are assumed to be the same throughout the specimen. However, there is variation in the stress field, especially around the crack tip due to crack tip plasticity, which would affect the strain energy density dissipation value. Literature indicates potential stress calculation methods such as using a domain J-integral, but methods do not currently

exist for calculating the stress during fatigue using DIC. As well, since there is not a consensus on the speckle size and subset size and radius for DIC, values were selected based on literature. Work could be performed to establish the digital image parameters selected were appropriate.

Several advances in fatigue life prediction using a strain energy-based method were accomplished. These included expanding the strain range approach to predict the fatigue life of coated nanocrystalline specimens loaded at varying stress ratios, as well as using DIC to predict impending failure based on the strain energy levels. The advances made in this thesis provide a better understanding of energy dissipation in fatigue and the subsequent applications for using energy dissipation to predict the fatigue life of coated specimens.

References

[1] S. Suresh, *Fatigue of Materials*. Cambridge University Press, 1998.

[2] National Transportation Safety Board, "DCA18MA142 SWA1380 Investigative Update," tech. rep., Philadelphia, 2018.

[3] M. A. Meyers, A. Mishra, and D. J. Benson, "Mechanical properties of nanocrystalline materials," *Progress in Materials Science*, vol. 51, no. 4, pp. 427–556, 2006.

[4] N. Enomoto, "On Fatigue Tests Under Progressive Stress," *American Society for Testing Materials*, vol. 55, pp. 903–917, 1955.

[5] F. Ellyin, *Fatigue Damage, Crack Growth and Life Prediction*. London: Chapman & Hall, 1st ed., 1996.

[6] E. Z. Stowell, "A study of the energy criterion for fatigue," *Nuclear Engineering and Design*, vol. 3, pp. 32–40, 1966.

[7] T. Letcher, M. H. Shen, O. Scott-Emuakpor, T. George, and C. Cross, "An energy-based critical fatigue life prediction method for AL6061-T6," *Fatigue and Fracture of Engineering Materials and Structures*, vol. 35, no. 9, pp. 861–870, 2012.

[8] O. Scott-Emuakpor, M.-H. H. Shen, T. George, C. J. Cross, and J. Calcaterra, "Development of an Improved High Cycle Fatigue Criterion," *Journal of Engineering for Gas Turbines and Power*, vol. 129, no. 1, p. 162, 2007.

[9] M. Shen and S. Akanda, "A Modified Closed Form Energy Based Framework for Fatigue Life Assessment for Aluminum 6061-T6 — Damaging Energy Approach," *J. Eng. Mater. Technol.*, vol. 137 (2), pp. 1–7, 2015.

[10] B. Pan, K. Qian, H. Xie, and A. Asundi, "Two-dimensional digital image correlation for in-plane displacement and strain measurement: A review," *Measurement Science and Technology*, vol. 20, no. 6, 2009.

[11] J. Rupil, S. Roux, F. Hild, and L. Vincent, "Fatigue microcrack detection with digital image correlation," *The Journal of Strain Analysis for Engineering Design*, vol. 46, no. 6, pp. 492–509, 2011.

[12] F. Mathieu, F. Hild, and S. Roux, "Fatigue crack propagation law measured from integrated digital image correlation: The example of Ti35 thin sheets," *Procedia Engineering*, vol. 10, pp. 1091–1096, 2011.

[13] C. M. Holycross, *A multiscale analysis and extension of an energy based fatigue life prediction method for high, low, and combined cycle fatigue.* PhD thesis, Ohio State University, 2016.

[14] J. D. Carroll, W. Abuzaid, J. Lambros, and H. Sehitoglu, "High resolution digital image correlation measurements of strain accumulation in fatigue crack growth," *International Journal of Fatigue*, vol. 57, pp. 140–150, 2013.

[15] R. K. Holman and P. K. Liaw, "Methodologies for predicting fatigue life," *JOM*, vol. 49, no. 7, pp. 46–52, 1997.

[16] A. Pineau, D. L. McDowell, E. P. Busso, and S. D. Antolovich, "Failure of metals II: Fatigue," *Acta Materialia*, vol. 107, pp. 484–507, 2016.

[17] E. Santecchia, A. M. Hamouda, F. Musharavati, E. Zalnezhad, M. Cabibbo, M. El Mehtedi, and S. Spigarelli, "A Review on Fatigue Life Prediction Methods for Metals," *Advances in Materials Science and Engineering*, vol. 2016, 2016.

[18] D. H. Kohn, P. Ducheyne, and J. Awerbuch, "Acoustic emission during fatigue of Ti-6Al-4V: Incipient fatigue crack detection limits and generalized data analysis methodology," *Journal of Materials Science*, vol. 27, no. 12, pp. 3133–3142, 1992.

[19] P. Paris and F. Erdogan, "A Critical Analysis of Crack Propagation Laws," *Journal of Basic Engineering*, vol. 85, no. 4, pp. 528–533, 1963.

[20] O. Scott-Emuakpor, T. George, C. Cross, and M. H. Shen, "Hysteresis-loop representation for strain energy calculation and fatigue assessment," *Journal of Strain Analysis for Engineering Design*, vol. 45, no. 4, pp. 275–282, 2010.

[21] V. Ontiveros, *Strain Energy Density and Thermodynamic Entropy as Prognostic Measures of Crack Initiation in Aluminum.* PhD thesis, University of Maryland, 2013.

[22] O. Scott-Emuakpor, M.-H. H. Shen, T. George, C. Cross, and J. Calcaterra, "A new energy-based uniaxial fatigue life prediction method for a gas turbine engine material," in *Proceedings of the ASME Turbo Expo*, vol. 5, pp. 393–405, 2007.

[23] M. H. Shen and S. R. Akanda, "A modified closed form energy-based framework for fatigue life assessment for aluminum 6061-T6: Strain range approach," *International Journal of Damage Mechanics*, vol. 25, no. 5, pp. 661–671, 2016.

[24] H. Ozaltun, M. H. Shen, T. George, and C. Cross, "An Energy Based Fatigue Life Prediction Framework for In-Service Structural Components," *Experimental Mechanics*, vol. 51, no. 5, pp. 707–718, 2011.

[25] H. Ozaltun, J. Seidt, M.-H. Shen, T. George, and C. Cross, "An energy-based method for uni-axial fatigue life calculation," in *Proceedings of the ASME Turbo Expo 2009: Power for Land, Sea, and Air.*, vol. 6, pp. 195–202, 2009.

[26] O. E. Scott-Emuakpor, H. Shen, T. George, and C. Cross, "An Energy-Based Uniaxial Fatigue Life Prediction Method for Commonly Used Gas Turbine Engine Materials," *Journal of Engineering for Gas Turbines and Power*, vol. 130, no. 6, pp. 062504–1, 2008.

[27] O. E. Scott-Emuakpor, B. T. Langley, C. M. Holycross, T. George, and B. D. Runyon, "Strain Sensor Comparison for Improving Experimental Measurement of Hysteresis Energy," *56th AIAA/ASCE/AHS/ASC Structures, Structural Dynamics, and Materials Conference*, no. January, pp. 1–9, 2015.

[28] D. Celli, *Measurement of Hysteresis Energy Using Digital Image Correlation with Application to Energy Based Fatigue Life Prediction and Assessment.* PhD thesis, Ohio State University, 2017.

[29] H. A. Padilla and B. L. Boyce, "A Review of fatigue behavior in nanocrystalline metals," *Experimental Mechanics*, vol. 50, no. 1, pp. 5–23, 2010.

[30] H. Gleiter, "Nanocrystalline materials," *Progress in Materials Science*, vol. 33, no. 4, pp. 223–315, 1989.

[31] T. Hanlon, E. D. Tabachnikova, and S. Suresh, "Fatigue behavior of nanocrystalline metals and alloys," *International Journal of Fatigue*, vol. 27, no. 10-12, pp. 1147–1158, 2005.

[32] P. Cavaliere, "Fatigue properties and crack behavior of ultra-fine and nanocrystalline pure metals," *International Journal of Fatigue*, vol. 31, no. 10, pp. 1476–1489, 2009.

[33] A. Singh, L. Tang, M. Dao, L. Lu, and S. Suresh, "Fracture toughness and fatigue crack growth characteristics of nanotwinned copper," *Acta Materialia*, vol. 59, no. 6, pp. 2437–2446, 2011.

[34] T. Hanlon, *Grain size effects on the fatigue response of nanocrystalline metals.* PhD thesis, Massachusetts Institute of Technology, 2004.

[35] K. R. Sriraman, S. Ganesh Sundara Raman, and S. K. Seshadri, "Influence of crystallite size on the hardness and fatigue life of steel samples coated with electrodeposited nanocrystalline Ni-W alloys," *Materials Letters*, vol. 61, no. 3, pp. 715–718, 2007.

[36] D. Burot, J. Harris, M. Sakovsky, and C. Steeves, "Fatigue Performance of Nanocrystalline Ni- or CoP-Coated Al 7255," tech. rep., University of Toronto Institute of Aerospace Studies, Toronto, 2012.

[37] C. Sachs, H. Fabritius, and D. Raabe, "Experimental investigation of the elastic-plastic deformation of mineralized lobster cuticle by digital image correlation," *Journal of Structural Biology*, vol. 155, no. 3, pp. 409–425, 2006.

[38] B. Pan, A. Asundi, H. Xie, and J. Gao, "Digital image correlation using iterative least squares and pointwise least squares for displacement field and strain field measurements," *Optics and Lasers in Engineering*, vol. 47, no. 7-8, pp. 865–874, 2009.

[39] N. McCormick and J. Lord, "Digital Image Correlation," *Materials Today*, vol. 13, pp. 52–54, dec 2010.

[40] F. Hild and S. Roux, "Digital image correlation: From displacement measurement to identification of elastic properties - A review," *Strain*, vol. 42, no. 2, pp. 69–80, 2006.

[41] J. Tong, "Full-field characterisation of crack tip deformation and fatigue crack growth using digital image correlation—a review," *Fatigue and Fracture of Engineering Materials and Structures*, vol. 41, no. 9, pp. 1855–1869, 2018.

[42] W. Zhang and Y. Liu, "Plastic zone size estimation under cyclic loadings using in situ optical microscopy fatigue testing," *Fatigue and Fracture of Engineering Materials and Structures*, vol. 34, no. 9, pp. 717–727, 2011.

[43] J. D. Carroll, W. Z. Abuzaid, J. Lambros, and H. Sehitoglu, "On the interactions between strain accumulation, microstructure, and fatigue crack behavior," *International Journal of Fracture*, vol. 180, no. 2, pp. 223–241, 2013.

[44] S. Roux, J. Réthoré, and F. Hild, "Digital image correlation and fracture: An advanced technique for estimating stress intensity factors of 2D and 3D cracks," *Journal of Physics D: Applied Physics*, vol. 42, no. 21, 2009.

[45] J. Rice, "A Path Independent Integral and the Approximate Analysis of Strain Concentration by Notches and Cracks," *Journal of Applied Mechanics*, vol. 35, no. 2, pp. 379–386, 1968.

[46] S. Yoneyama, S. Arikawa, S. Kusayanagi, and K. Hazumi, "Evaluating J-integral from displacement fields measured by digital image correlation," *Strain*, vol. 50, no. 2, pp. 147–160, 2014.

[47] T. H. Becker, M. Mostafavi, R. B. Tait, and T. J. Marrow, "An approach to calculate the J-integral by digital image correlation displacement field measurement," *Fatigue and Fracture of Engineering Materials and Structures*, vol. 35, no. 10, pp. 971–984, 2012.

[48] G. L. Gonzáles, J. A. González, J. T. Castro, and J. L. Freire, "A J-integral approach using digital image correlation for evaluating stress intensity factors in fatigue cracks with closure effects," *Theoretical and Applied Fracture Mechanics*, vol. 90, pp. 14–21, 2017.

[49] E. Malitckii, H. Remes, P. Lehto, Y. Yagodzinskyy, S. Bossuyt, and H. Hänninen, "Strain accumulation during microstructurally small fatigue crack propagation in bcc Fe-Cr ferritic stainless steel," *Acta Materialia*, vol. 144, pp. 51–59, 2018.

[50] P. Peralta, S. H. Choi, and J. Gee, "Experimental quantification of the plastic blunting process for stage II fatigue crack growth in one-phase metallic materials," *International Journal of Plasticity*, vol. 23, no. 10-11, pp. 1763–1795, 2007.

[51] C. Holycross, M.-H. H. Shen, O. E. Scott-Emuakpor, and T. George, "In Situ Study of Strain Energy Density at Notch Roots Using Digital Image Correlation," *56th AIAA/ASCE/AHS/ASC Structures, Structural Dynamics, and Materials Conference*, no. January, 2015.

[52] ASTM International, "ASTM E111-17 Standard Test Method for Young's Modulus, Tangent Modulus, and Chord Modulus," 2017.

[53] N. S. Rossini, M. Dassisti, K. Y. Benyounis, and A. G. Olabi, "Methods of measuring residual stresses in components," *Materials and Design*, vol. 35, pp. 572–588, 2012.

[54] A. M. El-Sherik, J. Shirokoff, and U. Erb, "Stress measurements in nanocrystalline Ni electrodeposits," *Journal of Alloys and Compounds*, vol. 389, no. 1-2, pp. 140–143, 2005.

[55] ASTM International, "ASTM E8/E8M-16a Standard Test Methods for Tension Testing of Metallic Materials," 2016.

[56] Department of Defense, *Handbook Metallic Materials and Elements for Aerospace Vehicles Structures*. 2003.

[57] S. Kalpakjian, "Tension," in *Manufacturing Engineering and Technology*, pp. 62–74, 1992.

[58] O. Scott-Emuakpor, "Development of a novel energy-based method for multi-axial fatigue strength assessment," vol. Ph.D., p. 181, 2007.

[59] C. Tofallis, "A better measure of relative prediction accuracy for model selection and model estimation," *Journal of the Operational Research Society*, vol. 66, no. 8, pp. 1352–1362, 2015.

[60] J. Réthoré, A. Leygue, M. Coret, L. Stainier, and E. Verron, "Computational measurements of stress fields from digital images," *International Journal for Numerical Methods in Engineering*, vol. 113, no. 12, pp. 1810–1826, 2018.